

REPORT DOCUMENTATION PAGE

Form Approved
OMB No. 0120-0188

Public reporting burden for this collection of information is estimated to average 1 hour per response, including the time for reviewing instructions, searching existing data sources, gathering and maintaining the data needed, and completing and reviewing the collection of information. Send comments regarding this burden estimate or any other aspect of this collection of information, including suggestions for reducing this burden, to Washington Headquarters Services, Directorate for Information Operations and Reports, 1215 Jefferson Davis Highway, Suite 1204, Arlington, VA 22202-4302, and to the Office of Management and Budget, Paperwork Reduction Project, OMB 0120-0188, Washington, DC 20503.

1. AGENCY USE ONLY (Leave blank)	2. REPORT DATE	3. REPORT TYPE AND DATES COVERED
	May 28, 1996	Final(7/15/92-2/29/96)
4. TITLE AND SUBTITLE		5. FUNDING NUMBERS
High Temperature Behavior of Metal Matrix Composites		AFOSR F49620-93-1-0087
6. AUTHOR(S)		
M. Taya, J.K. Lee, M.L. Dunn, G. Walker and T. Mori		
7. PERFORMING ORGANIZATION NAME(S) AND ADDRESS(ES)		AFOSR-TR-96 0388
Department of Mechanical Engineering University of Washington Box 352600 Seattle, WA 98195		
9. SPONSORING MONITORING AGENCY NAME(S) AND ADDRESS(ES)		10. SPONSORING MONITORING AGENCY REPORT NUMBER
Dr. Walter F. Jones Aerospace Science US Air Force of Scientific Office Bolling Air Force Base, DC 20332-6448		NA 93-1-0087
11. SUPPLEMENTARY NOTES		
12a. DISTRIBUTION AVAILABILITY STATEMENT		
unlimited 19960726 044		
13. ABSTRACT (Maximum 200 words)		
<p>When a metal matrix composite(MMC) is subjected to combined creep and thermal cycling loading, dimensional change is known to occur. This project is aimed at elucidating the mechanisms of a MMC subjected to creep/thermal cycling both experimentally and theoretically. The target MMCs is SiC particulate/Al matrix composite. The experimental results of dimensional change of SiCp/Al composite indicates that larger the maximum temperature(T_{max}), and larger creep applied stress, the larger dimensional change is observed. The analytical model based on dislocation punching can explain the experimental results well. Thermal cycling of SCS6 fiber/Ti-alloy matrix composite was also conducted and the mechanical properties of as-cycled composite were assessed. The minor degradation of the as-cycled composite was observed only under the condition that T_{max} is equal to or higher than 600C. Analytical modeling of relaxation of CTE mismatch strain that exists at the metal-ceramic interface was also developed by using variational principle and Eshelby's method. Complete relaxation can be found by minimizing the total potential energy. As a example, a complete relaxation of a creeping MMC is that the Von-Mises stress in the metal matrix becomes zero, i.e., hydrostatic state of stress.</p>		
14. SUBJECT TERMS		15. NUMBER OF PAGES
metal matrix composites, high temperature behavior, thermal cycling, creep, dislocation punching, CTE mismatch strain		126
		16. PRICE CODE
17. SECURITY CLASSIFICATION OF REPORT	18. SECURITY CLASSIFICATION OF THIS PAGE	19. SECURITY CLASSIFICATION OF ABSTRACT
unclassified	unclassified	unclassified
20. LIMITATION OF ABSTRACT		

High Temperature Behavior of Metal Matrix Composites



M. Taya, Professor
J. K. Lee, Graduate Student
Department of Mechanical Engineering
University of Washington
Seattle, WA 98195
Dr. Martin Dunn, University of Colorado
Mr. Gregory Walker, Boeing Company
and T. Mori, Tokyo Institute of Technology

AFOSR Final Technical Report (F49620-93-1-0087) covering July 15, 1994 through Feb. 29, 1996

May. 28, 1996

GENERAL INSTRUCTIONS FOR COMPLETING SF 298

The Report Documentation Page (RDP) is used in announcing and cataloging reports. It is important that this information be consistent with the rest of the report, particularly the cover and title page. Instructions for filling in each block of the form follow. It is important to *stay within the lines* to meet optical scanning requirements.

Block 1. Agency Use Only (Leave blank).

Block 2. Report Date. Full publication date including day, month, and year, if available (e.g. 1 Jan 88). Must cite at least the year.

Block 3. Type of Report and Dates Covered.

State whether report is interim, final, etc. If applicable, enter inclusive report dates (e.g. 10 Jun 87 - 30 Jun 88).

Block 4. Title and Subtitle. A title is taken from the part of the report that provides the most meaningful and complete information. When a report is prepared in more than one volume, repeat the primary title, add volume number, and include subtitle for the specific volume. On classified documents enter the title classification in parentheses.

Block 5. Funding Numbers. To include contract and grant numbers; may include program element number(s), project number(s), task number(s), and work unit number(s). Use the following labels:

C - Contract	PR - Project
G - Grant	TA - Task
PE - Program	WU - Work Unit
Element	Accession No.

Block 6. Author(s). Name(s) of person(s) responsible for writing the report, performing the research, or credited with the content of the report. If editor or compiler, this should follow the name(s).

Block 7. Performing Organization Name(s) and Address(es). Self-explanatory.

Block 8. Performing Organization Report Number. Enter the unique alphanumeric report number(s) assigned by the organization performing the report.

Block 9. Sponsoring/Monitoring Agency Name(s) and Address(es). Self-explanatory.

Block 10. Sponsoring/Monitoring Agency Report Number (If known)

Block 11. Supplementary Notes. Enter information not included elsewhere such as: Prepared in cooperation with...; Trans. of...; To be published in.... When a report is revised, include a statement whether the new report supersedes or supplements the older report.

Block 12a. Distribution/Availability Statement.

Denotes public availability or limitations. Cite any availability to the public. Enter additional limitations or special markings in all capitals (e.g. NOFORN, REL, ITAR).

DOD - See DoDD 5230.24, "Distribution Statements on Technical Documents."

DOE - See authorities.

NASA - See Handbook NHB 2200.2.

NTIS - Leave blank.

Block 12b. Distribution Code.

DOD - Leave blank.

DOE - Enter DOE distribution categories from the Standard Distribution for Unclassified Scientific and Technical Reports.

NASA - Leave blank.

NTIS - Leave blank.

Block 13. Abstract. Include a brief (Maximum 200 words) factual summary of the most significant information contained in the report.

Block 14. Subject Terms. Keywords or phrases identifying major subjects in the report.

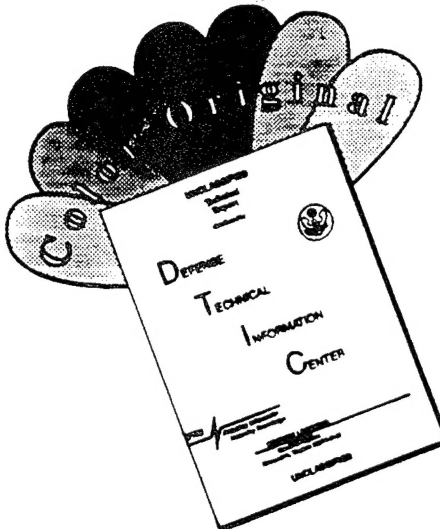
Block 15. Number of Pages. Enter the total number of pages.

Block 16. Price Code. Enter appropriate price code (NTIS only).

Blocks 17. - 19. Security Classifications. Self-explanatory. Enter U.S. Security Classification in accordance with U.S. Security Regulations (i.e., UNCLASSIFIED). If form contains classified information, stamp classification on the top and bottom of the page.

Block 20. Limitation of Abstract. This block must be completed to assign a limitation to the abstract. Enter either UL (unlimited) or SAR (same as report). An entry in this block is necessary if the abstract is to be limited. If blank, the abstract is assumed to be unlimited.

DISCLAIMER NOTICE



THIS DOCUMENT IS BEST
QUALITY AVAILABLE. THE COPY
FURNISHED TO DTIC CONTAINED
A SIGNIFICANT NUMBER OF
COLOR PAGES WHICH DO NOT
REPRODUCE LEGIBLY ON BLACK
AND WHITE MICROFICHE.

Table of Contents

1. Introduction	1
2. Experimental Study	2
2.1. Design of Creep/Thermal Cycler	2
2.2. Thermal Cycling Resistance of SCS-6/Ti-15-3 Metal Matrix Composite.....	6
2.3. Dimensional Change of SiC _p /Al Composite	16
2.4. Fracture Toughness of PSZ-SS/PSZ Composite-PSZ Laminate.....	21
3. Analytical Study I: Dislocation Punching from Ceramic/Metal Interfaces	32
3.1. Introduction	32
3.2. Dislocation Punching From a Short Fiber.....	33
3.3. Dislocation Punching From a Spherical Particle.....	37
3.4. Dislocation Punching From a Continuous Fiber.....	40
3.5. Dislocation Punching From a Planar Interface.....	42
3.6. References.....	45
4. Analytical Study II: Dimensional Change of MMCs	47
4.1. Analytical Model for Short Fiber Composites	47
4.2. Analytical Model for a Particulate Composite.....	64
5. Analytical Study III: Stress Relaxation by Plastic Flow, Interfacial Sliding and Diffusion in an Inclusion Bearing Material	84
5.1. Introduction	84
5.2. Elastic State After Complete Relaxation	84
5.3. Discussion.....	99
5.4. Summary.....	103
5.5. References.....	103
6. Analytical Study IV: Dislocation Punching in Functionally-Graded Materials.....	107
6.1. Introduction	107
6.2. Model and Analysis.....	108
6.3. Discussion.....	115
6.4. Summary.....	120

6.5. References.....	120
7. Conclusion	123
8. List of Publications.....	124

1. Introduction

High temperature behavior of metal matrix composites (MMCs) has been reviewed recently by Taya and his co-workers [1-3], where creep behavior and thermal cycling resistance of MMCs are discussed. Creep resistance of a MMC is superior to that of the unreinforced metal, while thermal cycling resistance of a MMC is normally degraded more than that of the unreinforced metal. High temperature behavior of a MMC includes that of the MMC at room temperature which underwent a high temperature exposure. The key mechanism of a MMC that is subjected to excursion to and from high temperature environment is the relaxation of the otherwise high stresses induced by the difference in the coefficient of thermal expansion (CTE) between the metal matrix and ceramic or refractory filler.

This final report will discuss a number of subjects related to high temperature behavior of MMCs. The experimental work includes design of creep/thermal cycler, thermal cycling resistance of SCS-6/Ti-15-3 matrix composite, dimensional change of SiCp/Al composite, all of which are discussed in chapter 2. The analytical study consists of four subjects: dislocation punching from ceramic/metal interfaces, chapter 3, dimensional change of MMCs, chapter 4, stress relaxation by plastic flow, interfacial sliding and diffusion in an inclusion bearing material, chapter 5, and dislocation punching in functionally graded materials, chapter 6. Finally conclusion is given in chapter 7, followed by list of publications in chapter 8.

References

1. M. Taya, 1991, "Creep Behavior of Metal Matrix Composites," in Metal Matrix Composites: Mechanisms and Properties, eds by R. K. Everett and R. J. Arsenault, Academic Press, pp. 189-215.
2. M. Taya, 1993, "Mechanical Behavior of Metal Matrix Composites at High Temperatures," in Mechanical Properties of Metallic Composites, ed. S. Ochiai, Marcel Dekker Inc., 1993, pp. 553-611.
3. R. J. Arsenault, S. G. Fishman and M. Taya, 1994, "Deformation and Fracture Behavior of Metal-Ceramic Matrix Composites," in Progress of Mater. Sci., Vol. 38, eds J. W. Christian and T. B. Massalski, pp. 1-157.

2. Experimental Study

We have performed several experimental works, (1) design of a creep/thermal cycler, (2) thermal cycling resistance of SCS-6 fiber/Ti-15-3 matrix composite, (3) measurement of dimensional change of SiCp/Al composite subjected to combined creep/thermal cycling using the equipment designed in (1), and (4) fracture toughness of PSZ-SS/PSZ composite-PSZ laminate. The analytical model are also developed to explain the experimental results of (2)~(4), some of which are detailed in chapters 3 and 4.

2.1 Design of a Creep/Thermal Cycler for High Temperature Capability*

We reported in the first year annual report a summary of designing a creep/thermal cycler with low to intermediate temperature capability (T_{max} up to 400°C) where a capability of a constant stress loading was emphasized. For the second year, an emphasis is placed upon designing a new creep/thermal cycler with high temperature capability (T_{max} up to 1100°C) where a constant load is used. This is because for high temperature MMCs, dimensional change (or accumulated strain) is expected to be small (less than a few percent), thus justifying use of constant load device which is much easier to construct.

This creep/thermal cycler is designed to apply temperature fluctuations up to 1100°C under a dead load. A constant temperature furnace travels up and down while the specimen is subjected to a tensile load. The furnace is shuttled from one station to the other with wire cables driven by a 1/4-horsepower 12-V AC electric motor. The station hold time can be set independently in 2-minute increments up to a maximum of 32 minutes. the construction of the creep/thermal cycler is half done and will be finished in a few months.

Test Stand

The test stand is necessary for applying a load to a test specimen for an extended period of time under thermal cycling. This structure can be divided into two main sets; load train and load frame which consists of the front and rear frame. The front frame is 102 mm high by 52 mm wide by 6.35 mm wall thickness A500 grade steel rectangular tube, while the rear frame is L50.8mm x 50.8mm x 6.35mm steel angles. Fig. 2.1 shows the creep-thermal cycling system schematically.

*The results of this work were published in J. Experimental Mechanics, Vol. 35, 1995, pp. 66-70, "Creep and Thermal Cycling Fixture Design for Metal Matrix Composites," by Taya, M., Lee, J. K., Lui, M., and Armstrong, W. D..

Furnace

The machine is equipped with one 300 mm high by 450 mm diameter resistance element furnace as shown in Fig. 2.2. The furnace is mounted on a moving frame which slides on guides attached to the front frame. The furnace is powered by eight 356 mm long by 25.4 mm diameter silicon carbide heating elements. Each heating element has a 102 mm hot section. The maximum steady operating temperature of the furnace can go up to 1100°C. The resistivity of silicon carbide is so low that a transformer is required in most cases. Here two sets of transformers are used in parallel. As it is heated, the resistivity of silicon carbide decreases first(negative temperature coefficient of resistance) and then increases (positive temperature coefficient of resistance). The maximum recommended operating temperature of the heating elements is 1400°C. To prevent the heat convection and radiation from the top and bottom sides of the furnace, two hole caps are installed.

The temperature of furnace is controlled by a Barber Coleman 560 controller and a phase SCR(Silicon Controlled Rectifier) power switch. The SCR modulates small increments of power to the load, unlike conventional mechanical control, and eliminates the overshoot and undershoot associated with contactor control. In this design, the type R thermocouple is used to monitor and control the temperature of the furnace. Ordinarily the controllers are powered by the same current as the furnace.

The external jacket of the furnace is made of stainless steel. Inside the jacket the furnace is insulated with 450 mm diameter disks of high temperature Cerachem insulating blanket and Fiberfrax insulating GH board which can stand vibration, mechanical stresses and strong erosive forces. The maximum temperature at which the insulating blanket can be used is 1400°C.

Furnace Transport System

An arrangement of the furnace transport system is also shown in Fig. 2.1. The furnace moves vertically to place its hot section over a specimen while the specimen is kept stationary. The furnace hold time at each section can be set independently by a hold time setter. This results in thermal cycling of a specimen. The furnace is installed on a moving frame which slides on steel rods attached to the front frame. The moving frame is driven by a 1/4 horsepower AC electric motor with two take-up reels. The take-up reels wind 3.2 mm diameter swaged steel cables which are routed through pulleys attached to the top of the front frame. Ten seconds are required to move a furnace from the hold station to the specimen station.

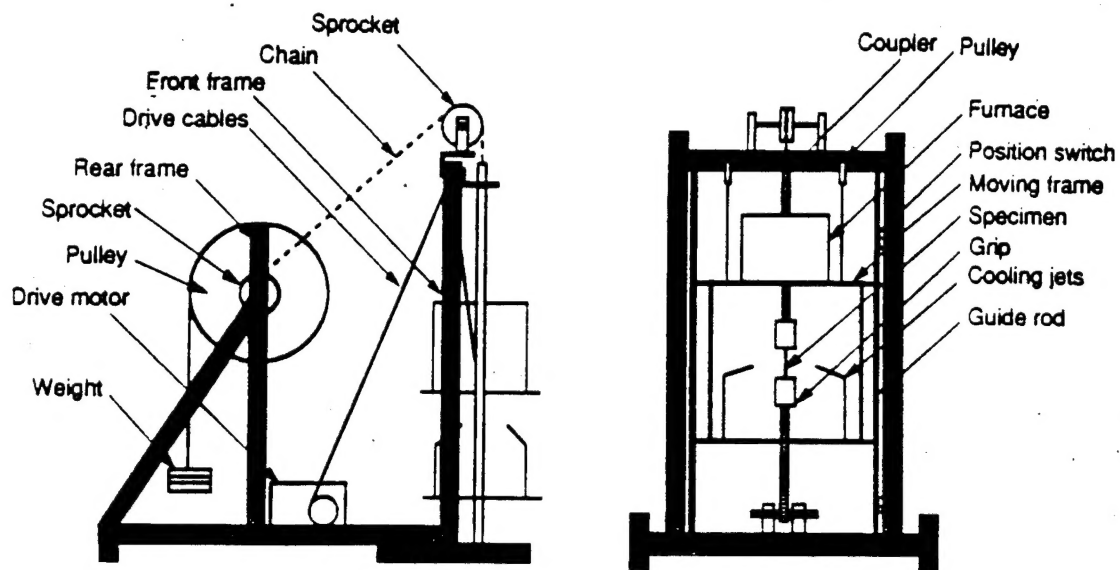


Fig. 2.1 Creep/thermal cycler with higher temperature capability

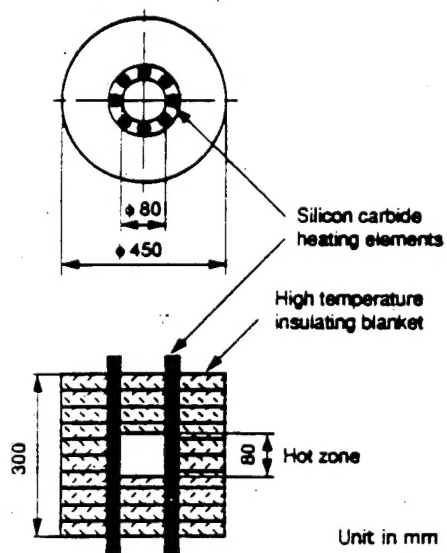


Fig. 2.2 Furnace

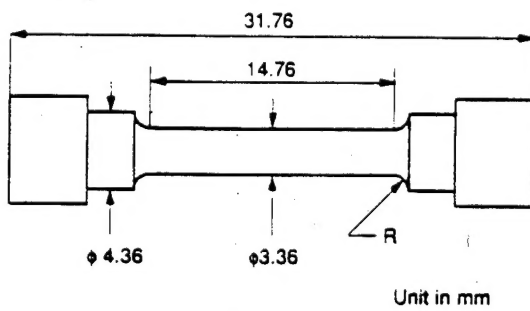


Fig. 2.3 Geometry of high temperature MMC specimen

Load Train

The load train is a set of parts connecting the dead weight with the specimen. The load train must sustain a large tensile load while being subjected to the time-temperature conditions imposed by the moving furnace. The load train is composed of weight pan, pulley, chain, two sprockets, one coupler, two long bars, two inconel grips, and a test specimen. The chain is made of stainless steel which can sustain 200 °C temperature. The chain connects one side of tensile bar with the sprocket attached to the pulley to transmit the load from the rear to the front frames. The load is applied to the specimen through a pulley (radius r_1), a sprocket (radius r_2), a chain, and a rod. The load magnification factor due to the cam and sprocket is r_1 / r_2 . In this design, the radius of the pulley is 5 times larger than that of the sprocket. The coupler is made of mild steel and has a one inch horizontal hole through which a hardened steel pin runs. The steel rods are connected with high temperature inconel grips which are tapped and attached to the specimen holder.

Specimen

Target metal matrix composite that will be tested by the new creep/thermal cycler is W-ThO₂ fiber/FeCrAlY matrix composite, which is durable up to 1100°C. The above MMC specimens have been processed through powder metallurgical processing route. Due to the limited amount of specimens, the specimen geometry of Fig. 2.3 will be used.

2.2. Thermal Cycling Resistance of SCS-6/Ti-15-3 Metal Matrix Composite

2.2.1 Introduction

In order to achieve high performance aerospace structures, materials possessing high strengths with low densities (high specific strengths), combined with high temperature resistance, are required. This is one reason for the relatively recent development of metal matrix composites (MMC) systems. Ceramic fibers in typical MMC's possess a coefficient of thermal expansion (CTE) much lower than the metal matrix. This mismatch of CTE's has the potential to cause cracking whenever this material is thermally cycled due to the strain on the fiber-matrix interface. This has been observed in various studies which have shown that accumulated damage can occur due to thermal cycling and, in certain cases, have resulted in the reduction of their mechanical properties [1-6]. In these particular studies, the MMC's were thermally cycled at elevated temperatures without external loading which caused a measurable elongation in the longitudinal fiber direction creating porosity and cracking at the fiber-matrix reaction zone. Both of these damage types were determined to be the direct result of CTE mismatch between the fiber and the matrix.

In most thermal cycling studies the specimens were exposed to the maximum temperatures for short time periods by using either "sine wave" or "saw tooth" temperature profiles. But in actual applications, these materials would likely be subjected to a thermal profile resembling a "square wave" with a dwell time at the maximum cycling temperature. This would then subject the specimens to a combination of sustained high temperature effects and thermal cycling and presumably give rise to severer damage.

2.2.2 Experimental procedure

The SCS-6 fiber/Ti-15-3-3-3 (Ti-15-3) MMC system was used for this study. This alloy is generally limited to applications below 550°C - 600°C because of alloy embrittlement due to oxygen diffusion through the surface [7]. The SCS-6 fibers were manufactured at Textron using a chemical vapor deposition (CVD) process starting with a 33 μm diameter carbon filament, upon which SiC was deposited. After the SiC was deposited, a complex outer coating of SiC and Carbon giving the fiber and overall diameter of 145 μm [8]. This outer coating is applied to reduce the surface flaws, allow for easier handling, and to limit the reaction zone between the fibers and the titanium matrix.

The reaction zone appears in almost all SiC/Ti MMC's as an interface which initially occurs as a result of processing or consolidation of the metal and fibers into MMC's. The metal matrix

consolidation is usually done at high temperatures (1100°C) where the outer coating of the fibers reacts with the titanium in the matrix creating a zone which can start as low as 727°C. This reaction zone is composed of small particulates which consist of TiC adjacent to the fiber and Ti_5Si_3 next to the matrix. In addition, some small "islands" of reaction products usually exist within the matrix adjacent to the fibers. This reaction zone is the fiber-matrix interface that transfers the loads from the matrix into the fibers and can greatly influence the mechanical behavior of the MMC [8].

The tensile specimens were fabricated from panels manufactured by Textron and donated by Boeing for this study. The panels consisted of eight alternating foils of Ti-15-3 with SCS-6 fibers in unidirectional orientation. The panels were determined to have a fiber volume fraction of approximately 36% -40% based on previous analysis by Boeing. No heat treatment was given to the panels prior to fabrication or testing of the specimens. Specimens were cut from the panels using electrical discharge machining (EDM) because usual machining processes could cause excessive fiber pullout in the curvatures of the specimen shape. No attempt was made to grind off any heat affected zone that may have developed during the EDM process. The tensile specimens were in a flatbar type configuration with the fiber oriented in the longitudinal direction. They were 76.2 mm long by 12.7 mm wide with a gage region 5 mm wide by 12.7 mm long.

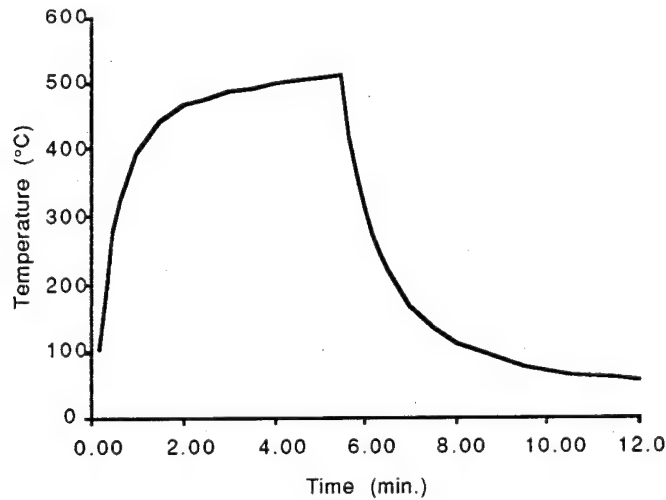


Figure 2.4 Typical thermal cycling temperature profile

The specimens were thermally cycled, unloaded, into and out of a 100 mm diameter vertical furnace tube heated using four SiC heating rods. Two thermocouples were used for temperature control; one was placed adjacent to the furnace wall for power supply control, and the other attached to the cycling specimens to determine the appropriate settings for the furnace power

supply. The specimens were attached to a rod that was moved into and out of the furnace by means of a motor/pulley system using a mechanical timer.

Each thermal cycle combined a heat cycle, approximately 5 minutes, with a 7 minute non-forced air cooling cycle. The overall thermal cycle temperature profile resembled a "square wave" having an approximately 3 minute dwell at the maximum thermal cycle temperature (T_{max}), Fig. 2.4. The specimens were exposed to T_{max} for 25, 50 and 75 hours for; 500, 1000, and 1500 cycles, respectively.

Four maximum elevated cycling temperatures were used; 500°C, 600°C, 650°C, and 700°C. Three specimens were cycled at each maximum cycling temperature with the removal of one specimen after every 500 cycles. In addition, dimensions of the specimens were determined periodically during the thermal cycling testing.

2.2.3 Results

The results of the tensile testing are shown in Fig. 2.5 with each point representing the results of one tensile specimen test. The failure stresses appear to decreased consistently with increasing maximum cycling temperatures by about 250 MPa for each different setting of T_{max} . Samples of specimens were examined metallographically revealing a greater change in the matrix microstructures with increasing maximum cycling temperatures when compared with the uncycled specimens. The uncycled specimen exhibited a typical as-received Ti-15-3 microstructure (Fig. 2.6a) which contained a few dark blotchy regions distributed throughout the matrix. These regions were probably the solute lean, coherent β' phase [9].

Starting with the 500°C specimens, the α phase began to precipitate in a very fine needle form from the β' phase. (Fig. 2.6b). These precipitates gradually increased in dimensions as seen in the 600°C/1500 cycle microstructure then became extremely coarse as the maximum cycling and temperatures were increased to 700°C/1500 cycles. The largest α phase precipitates were located adjacent to the grain boundaries and the fibers. However, no cracks or other damage was observed in the matrix of any of the specimens.

In addition, an oxide layer covering the specimens was observed which increased in thickness with higher maximum cycling temperatures and cycles. But even at the most extreme case, 700°C at 1500 cycles, the oxidation did not penetrate beyond the first fiber layer.

The fiber-matrix reaction zones do not appear to change with either increasing cycles or maximum temperatures. In addition, no debonding or damage was observed at the reaction zone. The fibers were neither affected by the thermal cycling, other than cracks observed in a few fibers which corresponded directly to the mechanical test machine grip impressions made on the surface of the specimens.

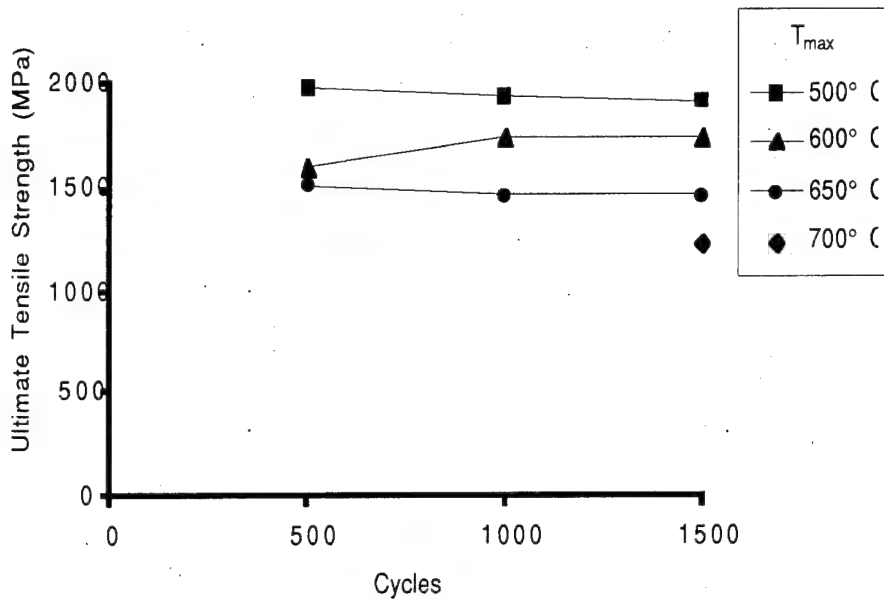


Figure 2.5 Residual tensile strength of thermal cycled specimens

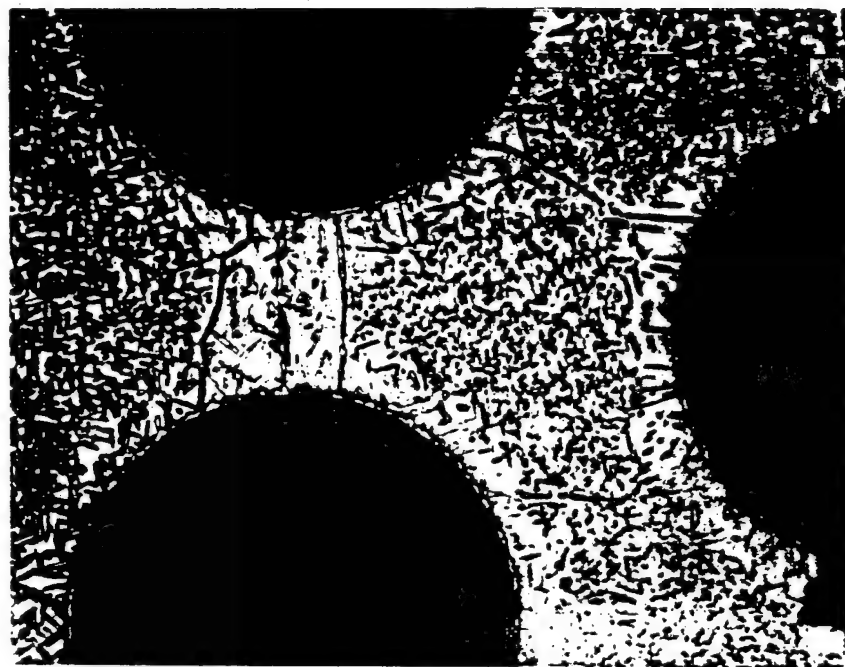
Evaluation of the fracture surface morphology of the tensile specimens revealed no significant differences regardless of the cycling conditions. The matrix adjacent to the fibers formed sharp ridges consistent with plastic flow. Dimpling, also indicative of plastic overload, was present on all of the matrix surfaces whether it was on the ridges adjacent to the fibers or between the fibers. The reaction zones on the other hand, appeared to have fractured in a brittle mode. These materials did not adhere consistently to either the outer coatings, on the fibers, or the matrix. Furthermore, a fracture region between the carbon fiber core and the SiC region was clearly observed. This interface was not easily characterized in the metallographic examination. It appears to be similar to the fiber-matrix reaction zone in that it adhered to both fracture surfaces inconsistently.

The metallographic mounts of the uncycled and the 700°C/1500 cycled specimen were placed in a scanning electron microscope for further evaluation of the reaction zone. Like the optical examination, no significant microstructural changes could be detected at a 7500X magnification. The only notable change was the configuration of the outer layer of the fiber. The uncycled coating on the fiber appeared to be in three layers probably composed of equal compositions based on the signal strength detected by the SEM which corresponding to their atomic numbers. The 700°C/1500 specimen reaction zone appeared to have only two such layers but it had the same total thickness (approximately 4.5 μm) as the un-cycled reaction zone. The reaction zones also appeared to have same average thickness and possessing similar jagged appearance.

Most of the specimens developed overall dimensional changes during the cycling. All of the recorded specimen dimensions generally increased with increasing maximum cycling temperatures



(a)



(b)

Figure 2.6 a) Microstructure of the uncycled specimen and b) microstructure of the 700° C/1500 cycled specimen

and cycles. The maximum dimensional change was 0.215 inch on the 700°C/1500 specimen at the gage thickness. However, the length or longitudinal direction measurements did not increase consistently with the other measurements. A comparison of the micrometer measurements with the oxide measurements from the micrographs, indicated that the specimen growth was due to the oxidation products.

2.2.4 Discussion

Since no general damage or porosity was observed, this would suggest that a microstructural or chemical change occurred within the composite material which would cause a reduction in the tensile properties. There are three primary material components within the MMC; the fibers, reaction zone, and the Ti-15-3 matrix, which can affect the properties of the composite system.

From observations, the fibers did not appear to have been affected either by the increase in the number of cycles or the maximum cycling temperature. No cracks or microstructural changes were observed in the cross sections, either in the core or the bulk of the fibers, which would suggest that the thermal cycling did not effect the fiber material to any noticeable degree. This is consistent with other studies that have shown that these fiber types by themselves exhibited little change in their mechanical properties up to approximately 1100°C [10]. Since these specimens were cycled at considerably lower temperatures it would appear that the fibers themselves were not affected.

The fibers' strength within the matrix can be greatly affected by the properties of the fiber-matrix reaction zone. Yet observations of the reaction zones did not reveal any microstructural changes and these regions were probably not effected by the thermal cycling. In other work, [11] it was reported that the reaction zone of the SCS-6/Ti-15-3 system can actually increase in strength under specific thermal aging conditions. In a SCS-6/Ti-15-3 composite system the interfacial shear strength increased from approximately 118 MPa to 131 MPa, at 800°C from 12 hours to 50 hours. This would increase the overall strength of the fibers and therefore the composite as it would allow for better transfer of the loads to the fibers. But since the composite material in this study exhibited a decrease in strength, any possible changes to the interfacial shear strength of the reaction zone did not seem to have any affect.

Since the fibers and the reaction zone did not appear to change the mechanical properties of the MMC, the only component of the composite that most likely contributed to the reduced strength in the composite was the matrix. Heat treatment studies of SCS-6/Ti-15-3 have shown that the matrix will decrease in strength over time due to phase changes [9]. The study compared unreinforced Ti-15-3 alloy properties to SCS-6/Ti-15-3 composite properties by aging the materials at temperatures ranging from 300°C to 700°C for 24 hours. It revealed that, based on hardness

measurements, the strength of the MMC would increase to a plateau between 400°C and 500°C and then decrease with increasing aging temperatures. In a related study [12], this MMC was aged for the times and temperatures shown in Table 2.1 with the resulting ultimate tensile strengths:

Table 2.1

Temperature/Time	UTS (MPa)
As Fabricated	1572 \pm 125
500°C/50 hr	1728 \pm 130
500°C/100 hr	1607 \pm 104
800°C/12 hr	1331 \pm 41
800°C/50 hr	1269 \pm 212

The thermal treatments shown above most likely causes the solute rich alloy to separate into solute-rich β and α solute-lean β' phases prior to the precipitation of the α phase from the β' crystals. The α phase provides strengthening to the alloy but requires long aging time due to the slow formation kinetics. Ti-15-3 is also susceptible to grain boundary formation of the α phase. This is due to the nucleation kinetics of the α in the grain boundaries which is not as sensitive to β stabilizers as the kinetics for the formation of intergranular α [13]. Additional aging coarsens the α phase which in turn reduces its strain to failure and eventually reducing the overall strength of the alloy.

Since the residual strengths of the specimens doesn't change appreciably for a given maximum thermal cycling temperature level after the first 500 cycles, it appears that the reduction in strength of this MMC occurred during the first 500 cycles.

In comparison to a similar thermal cycling study [14], the tensile specimens exhibited no appreciable change in the residual strength even after undergoing more cycles than specimens had undergone for this paper. In that study, two sets of tensile specimens were cycled from 149°C to 427°C and from 149°C to 649°C, for up to 16,750 cycles yet the tensile strengths varied between 1750 MPa and 1900 MPa with no correlation to the number of cycles or the maximum cycling temperature level. The composite lay-up of eight plies was similar to the one used for this study however their tensile specimens were rectangle in shape, 12.7 mm by 177 mm, with no specific gage length or necked region. In addition, these specimens started cycling in the "as-received" condition and in an unloaded condition. However, the specimens were cycled using a 48 second cycle "saw tooth" temperature profile with no dwell time at either the high or low temperatures. It appears that their specimens were probably not overaged due to the limited time at the elevated temperature and therefore did not suffer a reduction in tensile strength. The different cycling

thermal profiles used in these studies may be responsible for the discrepancy of the results.

In another study [15] using a similar thermal cycling temperature profile, 33.3 hours at T_{\max} , the reduction in the residual strength of the specimens (SCS-6/Ti-6Al-4V) was attributed to changes of the matrix, primarily oxygen embrittlement, which subsequently caused a degradation of the fibers.

A calculation was performed on the tensile data using the rule of mixtures, Eq. (2.1), to determine whether the reduction in the matrix strength could be directly correlated to the overall composite strength:

$$\sigma_c = V_f \sigma_f + (1 - V_f) \sigma_m \quad (2.1)$$

The matrix and fiber strength values used for the calculations were obtained from previous studies [9,16]. As seen in Fig. 2.7, the results do not correspond generally for the data beyond the 600°C strength levels. There are two possible reasons for this discrepancy. One is that the rule of mixtures is a simple model that may not take into account the interactions of other variables that could affect this specific composite, such as the interfacial shear strength. Another reason would most likely be the nonuniform matrix changes such as those observed in Fig. 2.6b. The precipitate lean region surrounding the fibers would exhibit a lower mechanical strength due to fewer precipitates which would reduce the overall matrix strength. The effective matrix flow stress that is influential in governing the fracture of a MMC is that of the matrix adjacent to the fiber. Thus if σ_m in equation (1) is replaced by the matrix flow stress of the soft region surrounding the fiber, then the rule of mixtures suggests that the strength of the composite is reduced due to the existence of the soft region.

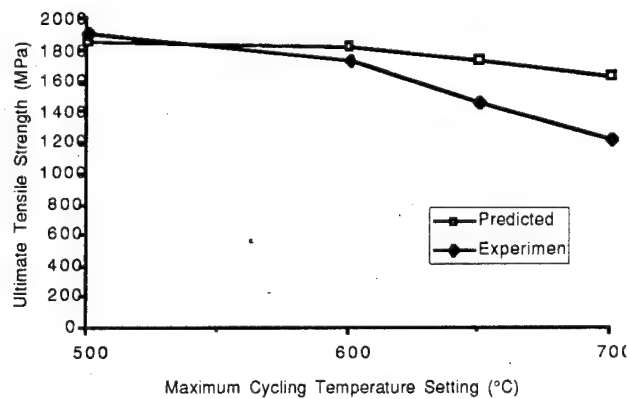


Figure 2.7 Plot of the rule of mixtures predictions compared to the experimental data

2.2.5 Conclusions

1. In regards to the fibers, matrix and the reaction zone, only the microstructure of the Ti-15-3 matrix exhibited a change which can be related primarily to the exposure of the specimen to a duration of accumulated thermal cycles at the maximum cycling temperature.
2. The microstructural changes of the Ti-15-3 matrix is the most likely explanation for the reduction in residual strength of the specimens and due to prolonged exposure to the higher temperatures used in this study.

2.2.6 References

1. W. G. Patterson and M. Taya, , "Thermal Cycling Damage of SiC Whisker/2124 Aluminum," *Proc. ICCM-5, AIME, 1985, pp. 53-66*
2. S. Yoda et al, "Thermal Cycling-Induced Deformation of Fibrous Composites with Particular Reference to the Tungsten-Copper System," *Metallurgical Transaction A, 1978, Vol. 9A, pp. 1229-1236*
3. Wolff et al, "Thermal Cycling of a Unidirectional Graphite-Magnesium Composite," *Journal of Material Science, 1985, Vol. 20. pp. 1141-1149*
4. T. Kyono, E. Kuroda, A. Kitamura, T. Mori, and M. Taya, "Effects of Thermal Cycling on Properties of Carbon Fiber / Aluminum Composites," *Transactions of the ASME, Journal of Engineering Materials and Technology, 1988, Vol. 110. pp. 89-95*
5. M. Taya and R. J. Arsenault, Metal Matrix Composites, Thermomechanical Behavior, (Permagon Press) 1989
6. R. C. Wetherhold and L. J. Westfall, "Thermal Cycling of Tungsten-Fibre-Reinforced Superalloy Composite," *Journal of Material Science, 1988, Vol. 23 pp. 713-717*
7. R. W. Schutz, "Environmental Behavior of Beta Titanium Alloys," *Journal of Metals, July 1994, pp 24-29*
8. B. A. Lerch and D. R. Hull, "As-Received Microstructure of a SiC/Ti-15-3 Composite," *NASA Technical Memorandum 100938, Aug. 1988*
9. B. A. Lerch, T. P. Gabb, and R. A. McKay, "Heat Treatment Study of the SiC/Ti-15-3 Composite System," *NASA TP 2970, Jan, 1990*
10. R. T. Bhatt and M. D. Kraitchman, "Environmental Effects on Tensile Strength of Chemically Vapor Deposited Silicon Carbide Fibers," *NASA TM-86981, April 1985, pp. 13-16*
11. S. M. Jeng, J. M. Yang, and C. J. Yang, "Fracture Mechanics of Fiber-Reinforced Titanium Alloy Matrix Composites, Part I: Interfacial Behavior," *Material Science and Engineering A138 (1991), pp 155-167*

12. S. M. Jeng, J. M. Yang, and C. J. Yang, "Fracture Mechanics of Fiber-Reinforced Titanium Alloy Matrix Composites, Part II: Tensile Behavior," *Material Science and Engineering A138* (1991), pp 169-180
13. R. Boyer, G. Welsch, and E. W. Collings, "Materials Properties Handbook: Titanium Alloys," *ASM*, pp 899-919
14. S. Mall and P. G. Ermer, "Thermal Fatigue Behavior of a Unidirectional SCS-6/Ti-15-3 Metal Matrix Composite," *Journal of Composite Materials Vol. 25 1991*, pp 1668-1686
15. S. H. Thomin, P. A. Noel, and D. C. Dunand, "Cracking Mechanisms in Thermally Cycled Ti-6Al-4V Reinforced with SiC Fibers," *Metallurgical Transaction A, 1995, Vol. 26A*, pp. 883-895
16. W. D. Pollock and W. S. Johnson, "Characterization of Unnotched SCS-6/Ti-15-3 Metal Matrix Composites at 650°C," *NASA Technical Memorandum 102699, Sept 1990*

2.3 Dimensional Change of SiC_p/Al Composite

The present MMC specimens made of SiC particulate/aluminum (A359) composite were processed by using the DURALCAN molten metal mixing technology by Alcan International Ltd., followed by extrusion with the ratio of 9:1. The volume fraction of the particulates (f) is 0.2. The range of the longer diameter of angular shaped SiC particulates is from $10 \mu\text{m}$ to $15 \mu\text{m}$. As-extruded SiC particulate/Al (SiC_p/Al) composite were subsequently all solution-treated at temperature 530°C . The same processing route was also used to fabricate control unreinforced matrix material[1]. As-extruded bar was further machined to a buttonhead specimen with shouldered ends whose loading axis is parallel to the extrusion direction. The dimensions of the gage section of a cylindrically shaped test specimen are 26.99 mm in length and 3.81 mm in diameter.

Thermal cycling creep tests were performed on SiC_p/Al composite specimens for two temperature profiles of $T_{\max}=300^\circ\text{C}$ and 350°C by using a thermal cycler with constant stress capability, consisting of a movable furnace of a constant temperature, temperature controller, load train and a cooling system[2]. Since the creep thermal cycling tests of MMCs are expected to result in a large deformation, a constant stress cam was employed to compensates the instantaneous change of the cross-sectional area of specimen so that the specimen can be loaded always under a constant stress condition during tests. A specimen is thermally cycled by the moving furnace and the forced cooling system where the heating and cooling durations are kept as 6.3 and 3.2 min., respectively. A typical temperature profile was measured by the K-type thermocouple embedded in the specimen, shown in Fig. 2.8 where (a) and (b) denote the cases of $T_{\max}=350^\circ\text{C}$ and $T_{\min}=115^\circ\text{C}$, and $T_{\max}=300^\circ\text{C}$ and $T_{\min}=100^\circ\text{C}$, respectively. The detail explanation of the creep thermal cycler is given elsewhere[2].

The dimensional change of SiC_p/Al composite has been known to be proportional to the number of thermal cycle (N) for a constant applied stress up to several hundred percent extension without any fracture and necking so that tests were performed up to the strain of about 0.5[3,4]. The dimensional change of a specimen was obtained by measuring the gauge length change after cycles with a digital vernier caliper of resolution $10 \mu\text{m}$ and experimental results are shown in Fig. 2.9. With the initial specimen gauge length of 26.99 mm the smallest resolvable strain is approximately 4×10^{-4} . Although the strain measurement is intermittent and its resolution is not so high, this strain measurement system is considered to be adequate because the purpose is to measure the dimensional change at different thermal cycles (N), for example, $N = 100, 500, 1000$.

The microstructural studies were also conducted using scanning electron microscope (JEOL-T330A) to compare the microstructural change in terms of particulate aspect ratio and particulate orientation before and after tests. The typical micrographs are shown in Fig. 2.10, where (a), (b)

and (c) denote as-received state, as-tested states under the applied stress of $\sigma^0=24$ MPa and $T_{\max}=300$ °C and $T_{\max}=350$ °C, respectively. The two tested specimens of Figs. 2.10 (b) and (c) were deformed to the elongations of 56% and 77 % without fracture, respectively. Based on micrographs having the total number of 604 particulates, a two-dimensional analysis was performed to determine the average aspect ratio and orientation of particulates. The distributions of particulate aspect ratio are shown in Fig. 2.11, where average aspect ratios are 2.15, 2.28 and 2.34 for Figs 2.10 (a), (b) and (c), respectively. The results of the microstructural study are used as input data for the analytical study.

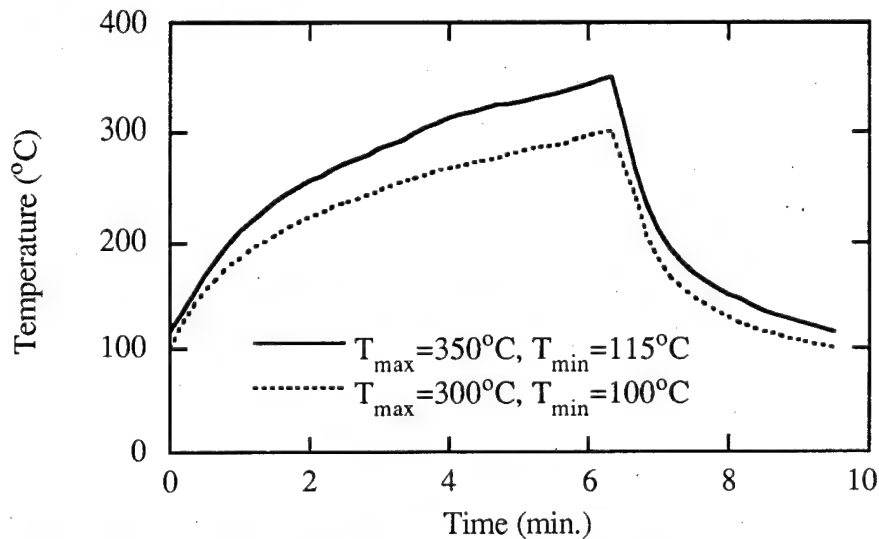


Figure 2.8 Typical temperature profiles used throughout experiment.

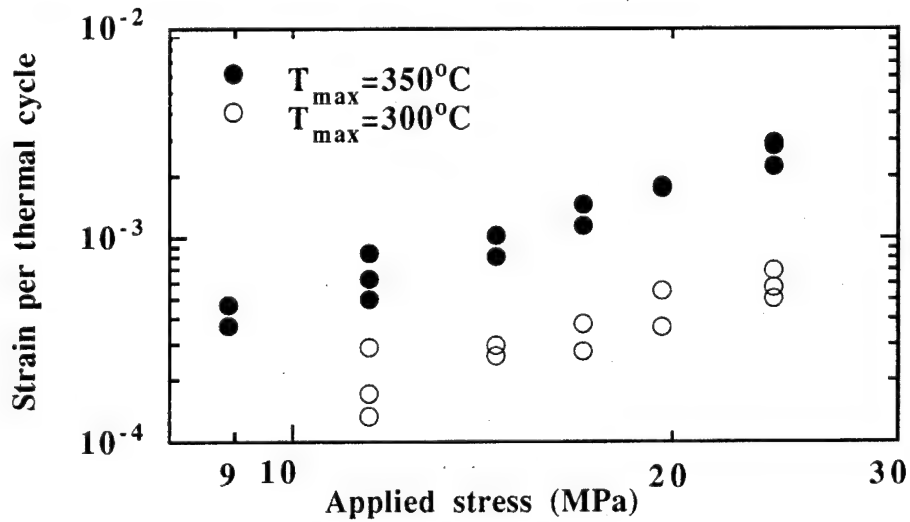
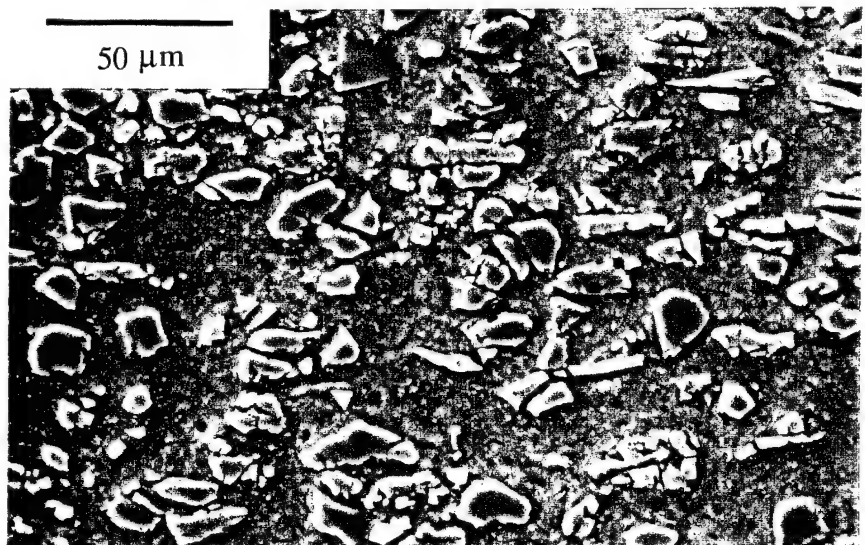
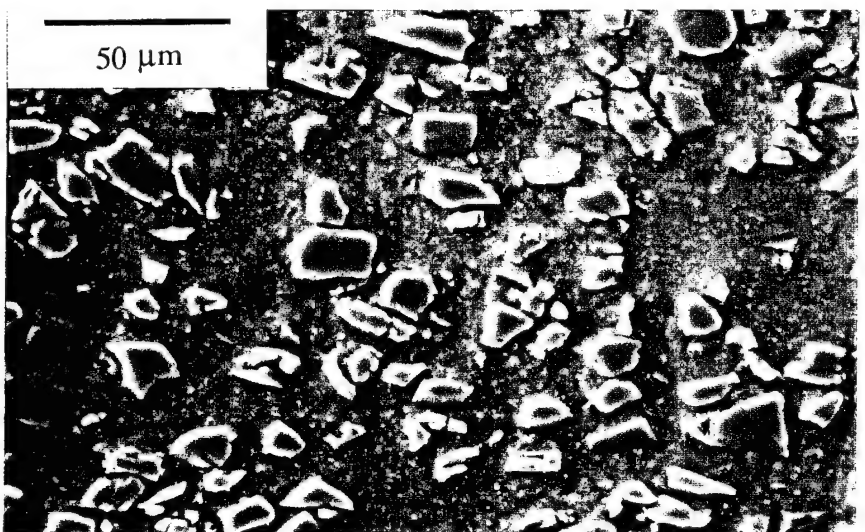


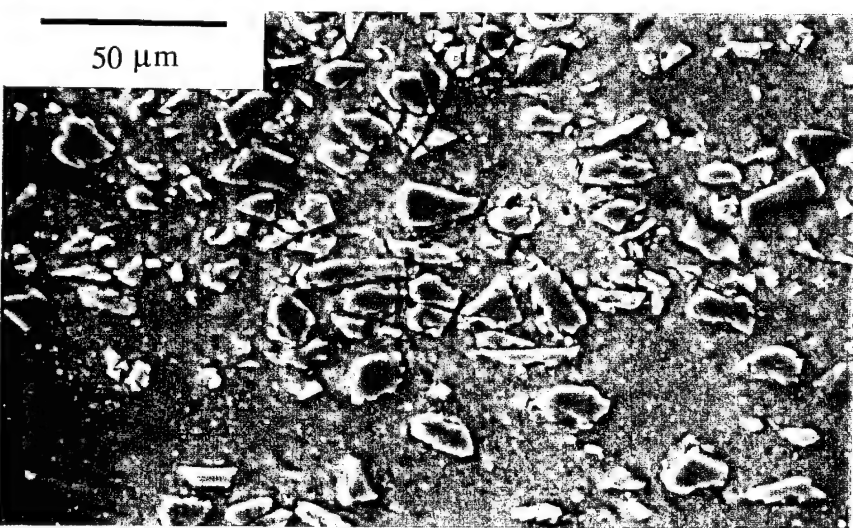
Figure 2.9 The experimental results of SiC_p/Al composite subjected to creep/thermal cycle loading: strain per thermal cycle vs. applied stress



(a)

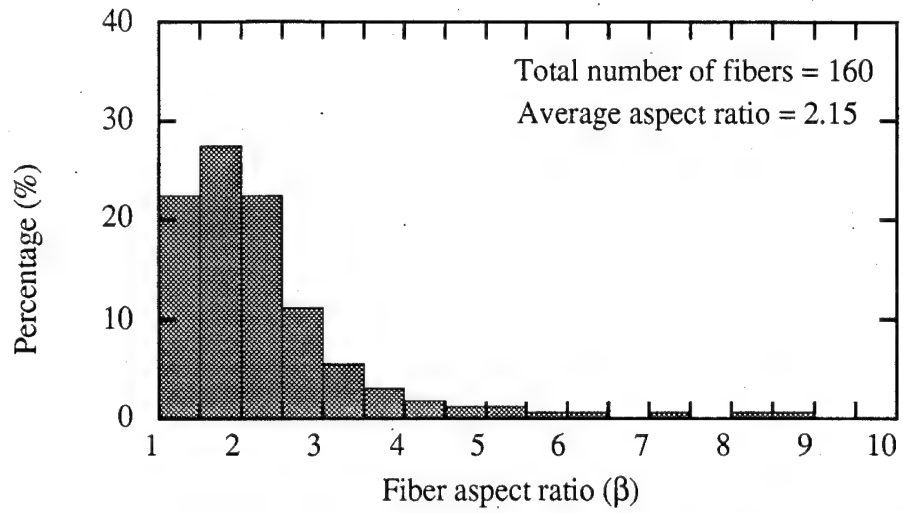


(b)

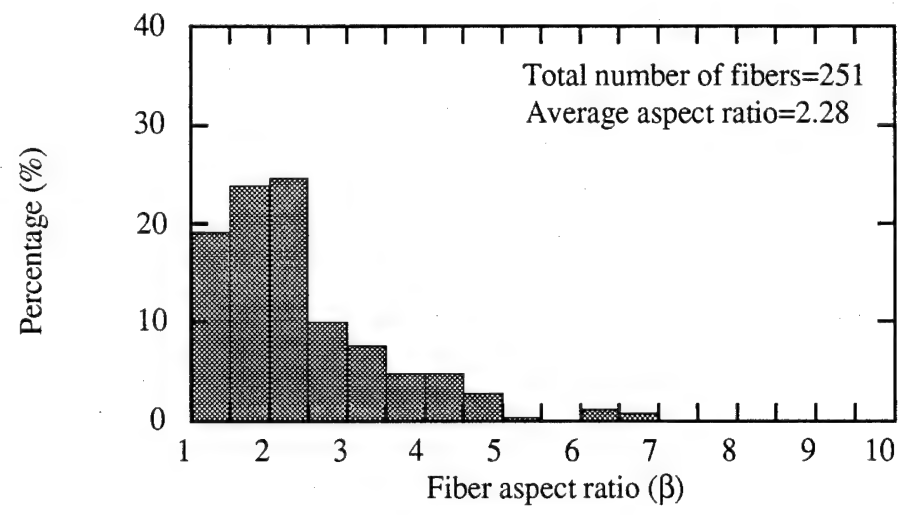


(c)

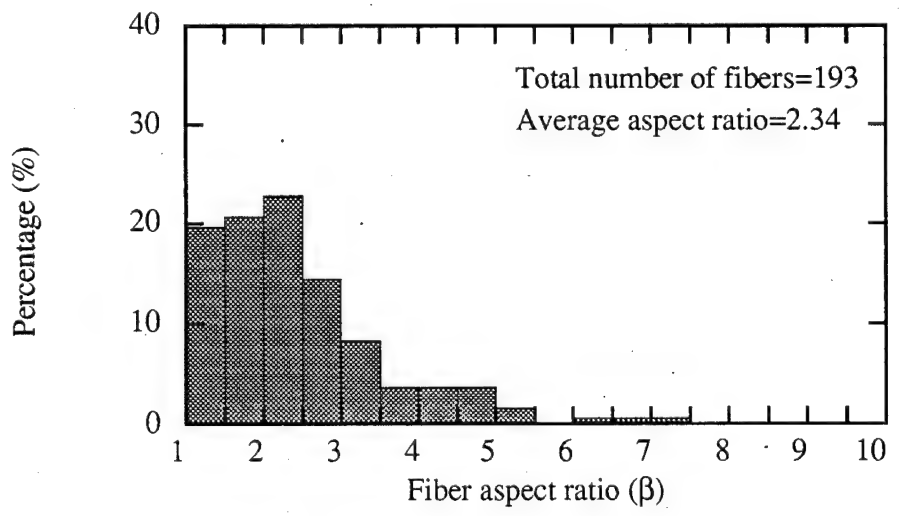
Figure 2.10 Typical microstructure of $\text{SiC}_\text{p}/\text{Al}$ composite observed by SEM: (a) as-received state, (b) as-tested under the applied stress of $\sigma^0=24$ MPa and $T_{\max}=300$ $^\circ\text{C}$ and (c) $T_{\max}=350$ $^\circ\text{C}$, respectively, where the horizontal direction (\leftrightarrow) coincides with the directions of the extrusion and applied stress.



(a)



(b)



(c)

Figure 2.11 Histograms showing the distribution of fiber aspect ratios from the microstructural studies on: (a) the as-received, (b) as-tested under $\sigma^0=24$ MPa and $T_{max}=300$ °C and (c) $T_{max}=350$ °C, respectively. Average aspect ratio is determined to be 2.25.

References

1. D. J. Lloyd: In High Performance Composite: Commonality of Phenomena, edited by K. K. Chawla, P. K. Liaw and S. G. Fishman, The Minerals, Metals and Materials Society, 1994, pp. 465-473.
2. M. Taya et al., "Creep and Thermal Cycling Fixture Design for Metal Matrix Composites," J. Exp. Mech., 35 (1995), 66-70.
3. M. Y. Wu and O. D. Sherby, "Superplasticity in a Silicon Carbide Whisker Reinforced Aluminum Alloy," Scripta Metall., 18 (1984), 773-776.
4. S. M. Pickard and B. Derby, "The Deformation of Particle Reinforced Metal Matrix Composites During Temperature Cycling," Acta Metall., 38 (1990), 2537-2552.

2.4 Fracture Toughness of PSZ-SS/PSZ Composite-PSZ Laminate*

Ceramics has not only high stiffness, high compressive strength and high hardness, but also good fatigue resistance, good creep and corrosion resistance. These material properties make ceramics very useful in engines, cutting tools and some structure designs in aerospace engineering. Despite the above advantages, the toughness or crack growth resistance of ceramics is low, typically $2\text{--}5\text{ MPa}\sqrt{\text{m}}$. This disadvantage really weakens the load carrying capacity of a ceramic structure and impedes the wide application of this material. One of the methods to improve the fracture toughness is to reinforce the ceramics with fillers (fibers and particles) and form a ceramic matrix composite (CMC). The microstructure in a CMC is normally homogeneous, i.e. the volume fraction of fillers is uniform spatially. It would be interesting to examine the fracture toughness as a function of crack extension (so called R-curve) of CMC if the microstructure of the CMC is not uniform. An example of such a CMC with non-homogeneous microstructure is shown in Fig. 2.11 where pure ceramic (partially stabilized zirconia, PSZ in short) sandwiches stainless steel/ PSZ composite (ceramic matrix composite, SS/PSZ composite in short). It would be valuable to assess the effect of the SS/PSZ composite layer on the R-curve behavior of the laminate which is expected to exhibit a transition behavior at the PSZ ceramic-SS/ PSZ composite interface as schematically indicated in Fig. 2.11. The purpose of this study is to assess the R-curve behavior of the PSZ-SS/PSZ composite-PSZ/laminate composite experimentally.

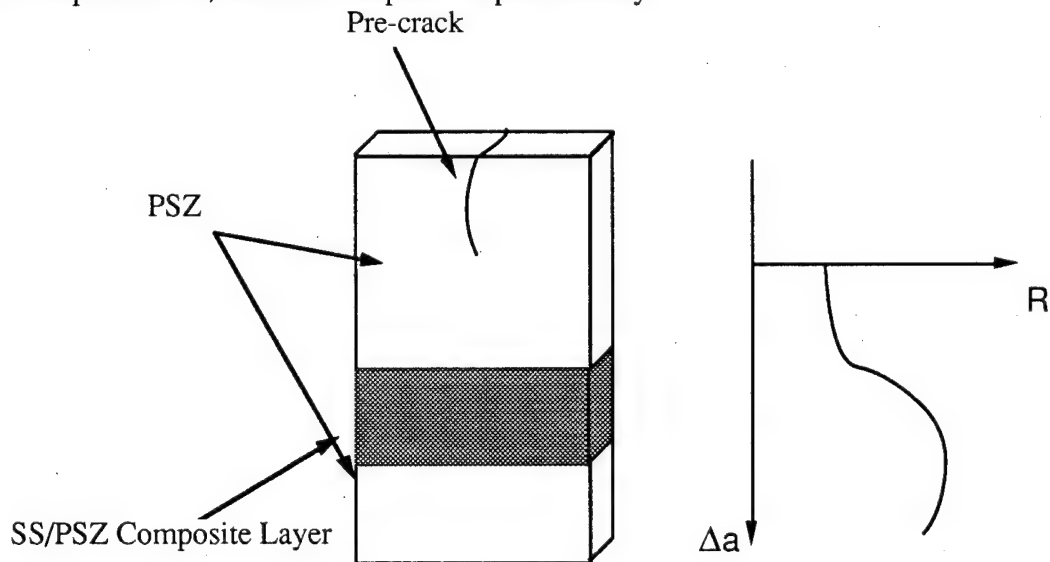


Figure 2.11 PSZ-SS/PSZ composite-PSZ laminate and expected R-curve*

* The results of this work were published in J. Amer. Ceram. Soc., Vol. 78 (6), 1995, pp. 1633-1639, "Experimental Study of the Fracture Toughness of a Ceramic/Ceramic-Matrix Composite Sandwich Structure," by Z. Liu, M. Taya, M. L. Dunn, and R. Watanabe.

2.4.1 Experiment

Loading Device and WL-DCB Specimen

The loading device shown in Fig. 2.12 can load or unload a specimen respectively by clockwise or counter clock-wise turn of the arm which is sensitively controlled by turning of the drive screw handle. The load is determined by the strain in the load cell which is connected with the strain gage indicator—model 3270, whose output numbers in the display are linearly related to the virtual load (P) on the specimen.

Unlike some other loading device in which the load is controlled by weight, this load is controlled by the displacement at the load point between loading pin and surface of the specimen. When the load increases, the displacement is increased, in the meantime, the increased displacement will reduce the load a little. This device is called displacement controlled loading device, or COD-feedback loading device, since this displacement is related to crack opening displacement (COD).

In order to control the speed of crack propagation, wedge-loaded double cantilever beam (WL-DCB) specimen with Chevron notch is selected (Fig. 2.13(a)). The cutting process is accomplished by using the diamond blade in the machine LEEMATIC 2000 surface grinders/slices.

Some improvements are made in the geometry and dimension of the specimen. The Chevron notch is replaced by the triangular notch (Fig. 2.13(b)), the V notch angle is reduced from 60° to 45° and the width of the specimen is cut significantly into a narrow one. By doing so, one can obtain a pre-crack more easily.

Moiré Interferential Optical System

In order to measure the fracture toughness, one can use data of COD of a specimen and the results of finite element analysis (hybrid-experimental-numerical method). Moiré interferential is a reliable displacement measurement method which can measure COD of the specimen used in this experiment. The details of the principle of the Moiré interferometry can be found elsewhere (Post, 1987).

Moiré interference can be produced by several different optical systems. The main part of the work is to obtain two coherent parallel lights from the right angle. In this experiment, a simple optical set-up as shown in Fig. 2.14 is used, where the second beam of coherent light is obtained with assistance of mirror 2 instead of two laser radiators. The function of the special filter and lens is to get a disk of parallel light, which should cover Mirror 2 and the specimen. The red laser beam comes from the Model 159 10mw Helium-Neon laser generator. Due to low power, there is no fan

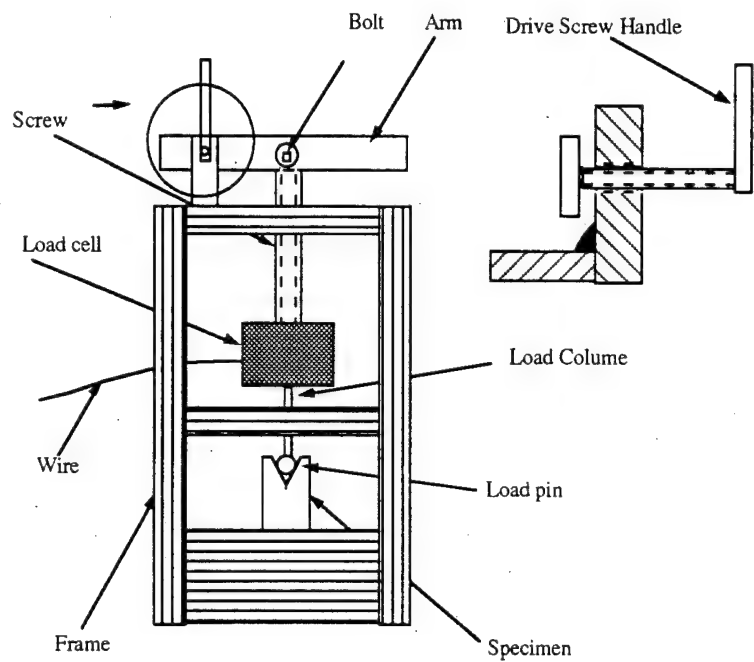


Figure 2.12 Loading device and WL-DCB specimen.

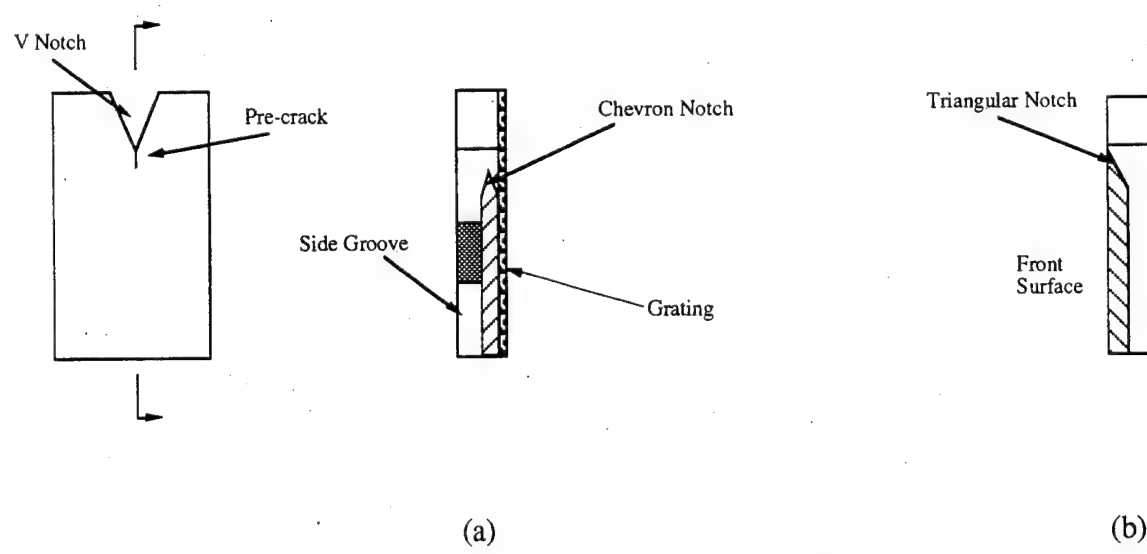


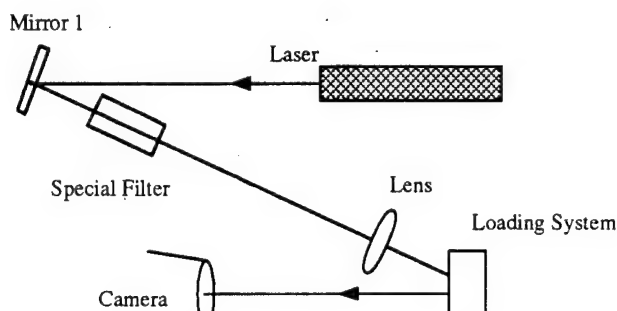
Figure 2.13 WL-DCB specimen: (a) chevron notch, (b) triangular notch.

in the radiator. This is very important, because if the vibration is brought from the fan, it will affect the fringes. In this experiment, the grating frequency is 1200 lines per millimeter, and the wavelength of the He-Ne red laser light is 6328nm which is equal to 6328×10^{-7} m, hence the angle of the incident light is given by

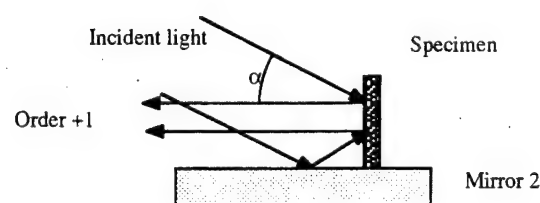
$$\alpha = \sin^{-1} \frac{f\lambda}{2} = \sin^{-1} \frac{1200 \times 6328 \times 10^{-7}}{2} = 22.3^\circ \quad (2.2)$$

Since the fringe pattern directly represents the displacement field, it is used to measure CODs which are in turn used to compute elastic energy. Following the principle of the moiré fringe in deformed field, the x-direction displacement (u) can be found in the fringe pattern, and given by

$$u = NP \quad (2.3)$$



(a)



(b)

Figure 2.14 Moiré interferometry system for displacement measurement.

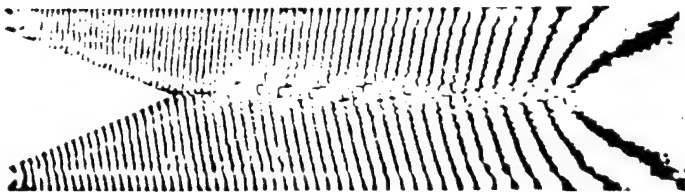


Figure 2.15 An example of Moiré pattern.

Where N is fringe order and P is pitch of the grating. There exists a difference between geometry Moiré and Moiré interferometry. In the Moiré interferometry, the pitch of the grating must be used as half of the real pitch. For example, if the pitch of the grating (P) is 1/1200 millimeter, when the displacement is calculated by Eq. (2.2), the effective pitch (P_{eff}) should be 1/2400 millimeter. Fig. 2.15 is one of the moiré fringe patterns observed in this experiment.

Basically, the zero-order fringe, which has no x -direction displacement on the fringe, is a bright straight line at the specimen's symmetric center connected with the crack tip. Next to the zero-order fringe is the dark half-order fringe, which represents displacement of the half pitch of the effective grating.

$$u = NP_{\text{eff}} = N \frac{P_{\text{real}}}{2} \times \frac{1}{2400} = 0.2083 \times 10^{-3} \text{ (mm)} \quad (2.4)$$

Similarly, the fringe order at load point can be counted, for example for $N = 56.5$, the displacement is

$$u = NP_{\text{eff}} = 56.5 \times \frac{1}{2400} = 23.542 \times 10^{-3} \text{ (mm)} \quad (2.5)$$

Since the load and geometry of the specimen are symmetrical, only a half of the specimen is used to compute the R-curve. However in reality, due to the error of the grating coating, the fringe pattern is often not symmetrical. Thus the average number is used to represent x -displacement.

Experimental Procedure

First, one must adjust the angle of the mirror 2 in Fig. 2.14 to obtain horizontal parallel fringe lines when the load is zero. The fewer these lines, the more accurate the optical system is adjusted. With the increase of the load, both the numbers of the fringes and the shape of the fringes are changed. In order to keep the fringe pattern symmetrical in this procedure, the angle of mirror 2 must be adjusted every time when an increase of load is applied. But only one direction of the angle needs to be adjusted, either up and down or left and right; otherwise, CODs of the specimen are not accurately shown by the fringe pattern. In fact, the absolute symmetric fringe pattern is very hard to maintain during the experiment, so the CODs measured at both edges are averaged.

Without a successive stable crack growth, the R-curve can not be obtained. Thus the load must be increased very slowly.

Computation of Energy Release Rate

Energy release rate is defined by

$$G = \frac{d(F-U)}{da} \quad (2.6)$$

where F is work done by external force, U is elastic energy contained in the specimen and a is the crack length. In the actual computation, the derivative in the Eq. (2.7) is approximated by the incremental form:

$$G_n = \frac{\Delta F - \Delta U}{\Delta a} = \frac{(F_{n+1} - F_n) - (U_{n+1} - U_n)}{(a_{n+1} - a_n)} \quad (2.7)$$

This requires the experimental procedure of continually recording the load, crack length and displacement from which the R-curve is computed.

Since PSZ and PSZ/SS composite are both brittle material, only elastic energy is considered in this case, and the analysis and computation can be based on linear elastic fracture mechanics (LEFM). In this fracture test, load in y direction is read by the strain gage indicator while the displacement in x direction at loading point by the Moiré fringe pattern.

External work and elastic energy can be computed by a finite element method (FEM). For a crack extension Δa in the specimen, a new mesh is generated and new external work and elastic

energy are computed. Then by the use of Eq. (2.4), the energy release rate is computed. The contribution to the energy change by Y component of the force (F_y) is so small, thus it can be neglected compared with the contribution by the displacement in x-direction. Then the Eq. (2.4) can be simplified as

$$G_n = \frac{U_n - U_{n+1}}{a_{n+1} - a_n} = R_n \quad (2.8)$$

In this equation, a_{n+1} is always larger than a_n and U_{n+1} is always less than U_n , hence the R_n is always positive.

Due to the symmetry of the specimen geometry and the load, only a half of the specimen geometry needs to be considered. Along the crack growth line, the denser mesh is needed and the node position around the crack tip should be changed to the quarter node. By doing so, a more accurate computation result can be achieved.

2.4.2 Result and Discussion

R-curve of PSZ-SS/PSZ Composite-PSZ Laminate

The experiment is performed on three specimens: one specimen made of PSZ only and two PSZ-SS/PSZ composite-PSZ laminate specimens with two different volume fraction of SS in the SS/PSZ composite area. The dimensions of the specimens are identical and they are shown in Fig. 2.16. The mechanical properties of SS, PSZ and SS/PSZ composite are shown in Table 2.2, where those of the composite are estimated by using the Eshelby's model [6].

In order to examine the effects of SS phase on the R-curve behavior in PSZ-SS/PSZ composite-PSZ laminate, two specimens are used: one contains 10% SS, another one 20% SS in SS/PSZ composite layer. As a reference, a pure PSZ specimen is also used. The results of R-curve (energy release rate) of these three specimen as a function of Δa are shown in Fig. 2.17, where SS/PSZ composite layer (CMC) region is indicated by horizontal bar.

It is often useful to convert R-curve to K_R - Δa relation, where K_R is the critical stress intensity factor or fracture toughness at a given crack length Δa . In plane stress condition

$$K_R = \sqrt{ER} \quad (2.9)$$

where E is modules of elasticity and R is crack growth resistance. Note in this formula, different values of E should be used in the different region. Fig. 2.18 is the K_R - Δa relation obtained from Fig. 2.17 and Eq. (2.9).

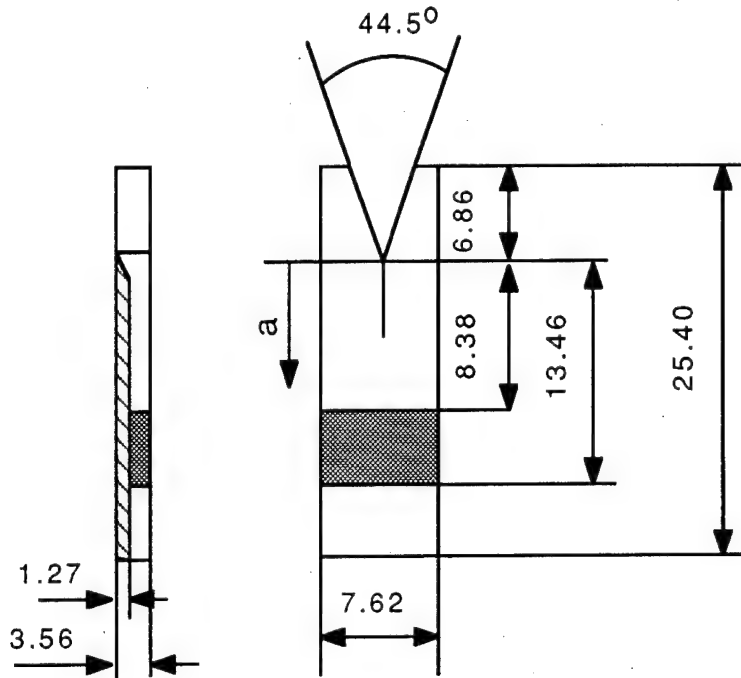


Figure 2.16 Dimensions of PSZ-SS/PSZ-PSZ laminate specimen.

Table 2.2 Mechanical Properties

	E (GPa)	Poisson's ratio ν	$CTE (10^{-6}/C^\circ)$
SS	196	0.26	14.0
PSZ	168.8	0.3	11.1
10%SS+90%PSZ	171.4	0.296	11.3
20%SS+80%PSZ	174.0	0.292	11.6

It is clear from Fig. 2.17 and 2.18 that the energy release rate (R) and fracture toughness (K_R) which are small during early stage of crack propagation, jump to a relatively large value once the crack advances the CMC region. The jump in terms of K_R is almost twice as large as that of unreinforced PSZ specimen. Fig. 2.17 and 2.18 also show the gradual increase in R - Δa or K_R - Δa curve in early stage of crack propagation characteristics with brittle materials.

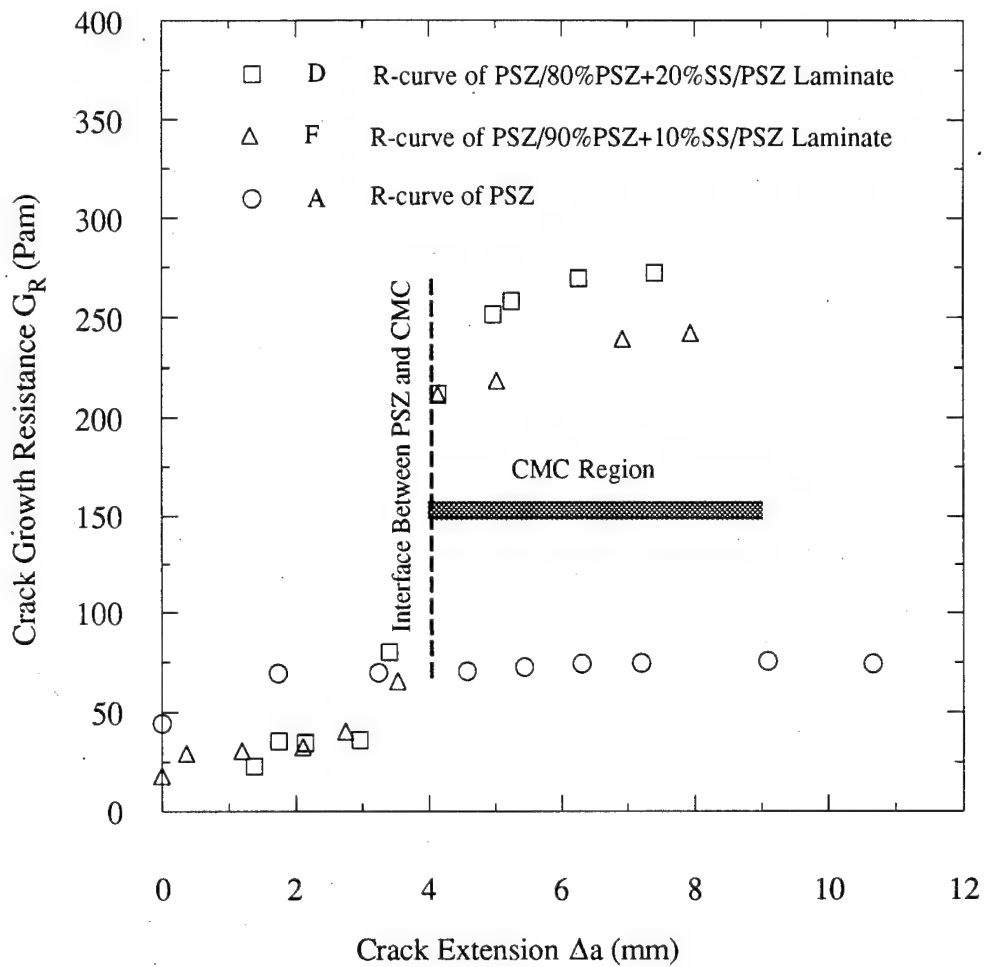


Figure 2.17 $R(G_R) - \Delta a$ relation.

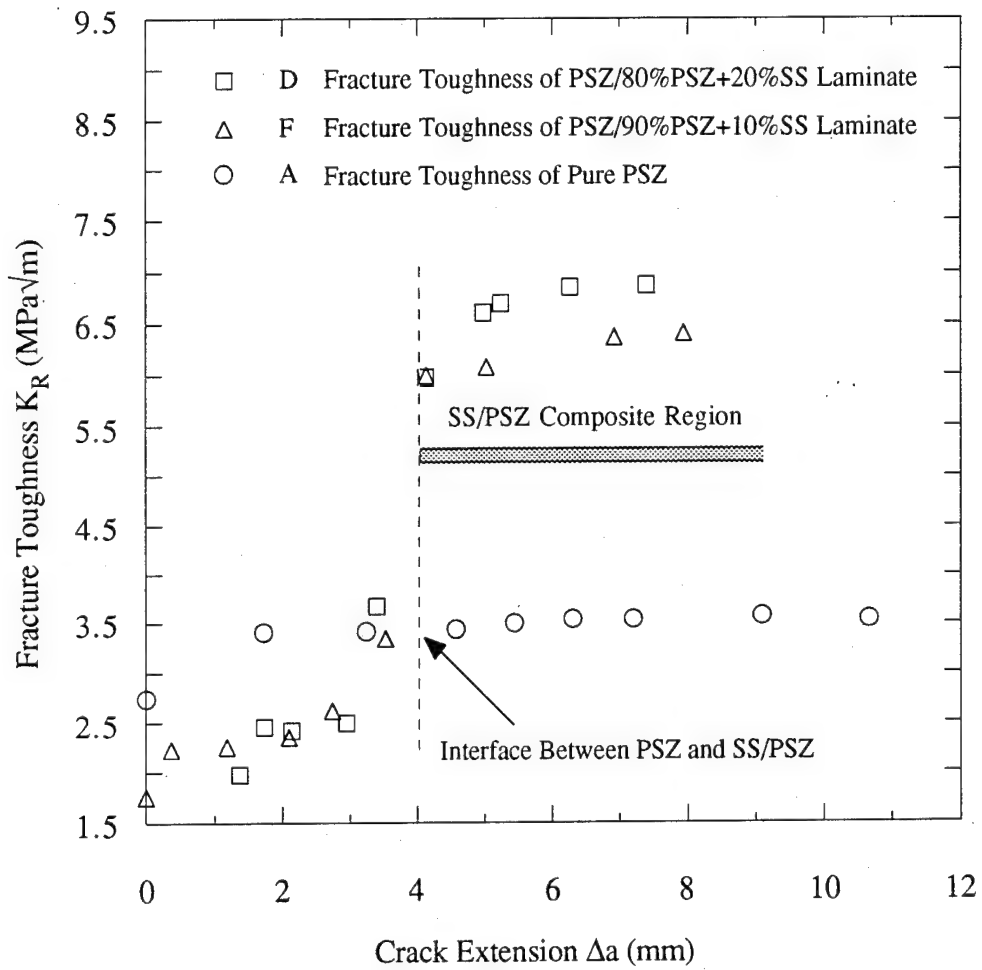


Figure 2.18 K_R - Δa relation.

2.4.3 References

1. Z. Li "R-curve behavior of PSZ/PSZ Matrix Composite/PSZ Laminate Structure" Master thesis of mechanical engineering in University of Washington, 1992
2. D. Broek, The Practical Use of Fracture Mechanics, Kluwer Academic, 1989
3. D. Post, . "Moire Interferometry". Handbook of Experimental Mechanics (A. S. Kobayashi, ed.). Englewood Cliffs, N.J., Prentice-Hall, pp. 314-387, 1987.
4. K. A. Holsapple, "FRED Input Instructions" at University of Washington, 1991.

5. O. C. Zienkiewicz, The Finite Element Method, pp.569-595, 1985.
6. M. Taya, R. J. Arsenault. Metal Matrix Composites: Thermomechanical Behavior, pergammon Press, Oxford, pp.32-36, 1989.
7. H. Tada " The Stress Analysis of Cracks" Del Research Corpotaion. pp.2.19-1.21, 1973
8. "Chevron-Notched Specimens" edited by Underwood, Freiman and Baratta, Philadelphia, Pa. ASTM, 1983
9. C.T. Yu and A. S. Kobayashi, "Fracture Process Zone in a Ceramic Composite", Technical Report No. UWA/DME/TR-91/4, 1991.

3. Analytical Study I: Dislocation Punching from Ceramic/Metal Interfaces*

3.1 Introduction

When two different materials are bonded, misfit strain exists at the interface at and around which high stress field is induced. This misfit strain at the interface is due to the mismatch in the stiffness of the materials and in coefficient of thermal expansion (CTE) under temperature change. The order of the misfit strain due to CTE mismatch can be quite large for larger temperature changes. Microscopically this misfit strain at the interface is accommodated by dislocations near the interface. When the magnitude of the stress field becomes too large, relaxation of the stress of large magnitude is more likely to take place. Punching of dislocations from the interface is such a relaxation mechanism and has been observed in dispersion-hardened alloys [1,2] metal matrix, composites [3-5], and metal coating/ceramic substrate system [6].

The dislocation punching model was first used by Ashby and Johnson [2] to explain the strengthening mechanism of dispersion-hardened alloys subjected to shear (plastic) strain γ where the punching of prismatic dislocation loops along the secondary slip planes is assumed. The work-hardening predicted by the Ashby's model is

$$\tau - \tau_y = 0.24\mu\sqrt{bf\gamma/d} \quad (3.1)$$

where τ and τ_y are the flow stress and initial yield stress in shear, μ , b and γ are the shear modulus, the Burgers' vector and plastic shear strain of the matrix, respectively, and f and d are the volume fraction and diameter of particles. This model predicts well the parabolic dependence of τ on γ observed in the experiment. The misfit strain in the Ashby's model before punching is represented by arrays of edge dislocations piled up at the particle/matrix interface. Tanaka and Mori [7] solved the problem of misfit strain at the interface by using the Eshelby's model [8] where the misfit (plastic) strain at the particle/matrix interface is smeared out to become "transformation strain" [8] or "eigenstrain" [9]. The stress-strain relation of a composite predicted by the Tanaka-Mori model is given by

$$\sigma_0 = \sigma_y + he_p \quad (3.2)$$

*The results of this work were published in J. Eng. Mater. Tech., Vol. 116, July 1994, pp. 408-413, "Dislocation Punching from Ceramic/Metal Interface," by M. Taya and T. Mori.

where σ_0 and σ_y are the flow stress and initial yield stress, h and e_p are the work-hardening rate and plastic strain along the loading direction. The linear relationship between $\sigma_0 - \sigma_y$ (work-hardening) and plastic strain e_p in the above equation agrees with the experiment for small range of plastic straining. For larger plastic straining, however, stress-strain curve deviates from the linear work-hardening predicted by the Tanaka Mori model. Tanaka et al. [10] proposed a model to account for non-linear work-hardening at larger strains by using a dislocation punching model.

Modeling of dislocation punching in a metal matrix composite subjected to temperature change ΔT was first studied by Arsenault and Shi [11] who used an equiaxed particulate (its length t) as a reinforcement and obtained the average dislocation density in the matrix metal, $\bar{\rho}$ given by

$$\bar{\rho} = \frac{12fe_T}{b(1-f)} \frac{1}{t} \quad (3.3)$$

where f is the volume fraction of particulates, e_T is CTE mismatch strain ($\Delta T \Delta \alpha$), b is Burgers' Vector. Once $\bar{\rho}$ is calculated, the increase in the matrix flow stress due to CTE mismatch strain, $\Delta \sigma_{CTE}$ may be estimated by

$$\Delta \sigma_{CTE} = \beta b \mu \sqrt{\bar{\rho}} \quad (3.4)$$

where β is a constant of order 1, μ is the matrix shear modulus.

Since 1986, more rigorous dislocation punching models have been developed by Taya and his co-workers, and they are aimed at various types of reinforcement geometry: spherical particle, short fiber, disc-shaped filler and continuous fiber. In this paper, we shall review recent studies on dislocation punching models for these types of reinforcement, and also the dislocation punching model for thin film/substrate system.

3.2 Dislocation Punching From a Short Fiber

Taya and Mori [12] studied analytically the dislocation punching from a short fiber in a short fiber metal matrix composite (MMC). A short fiber is simulated by a prolate ellipsoidal inhomogeneity to make use of the Eshelby's method and the CTE mismatch strain e_T is initially adhered to the fiber-matrix interface as surface dislocations (prismatic dislocation loops), Fig. 3.1(a). Due to the fact that the stress at fiber-ends is highest and the punching of the dislocation loops are favorable along the fiber axis (x_3 -axis), some of the dislocation loops are punched along the x_3 -axis, Fig. 3.1(b).

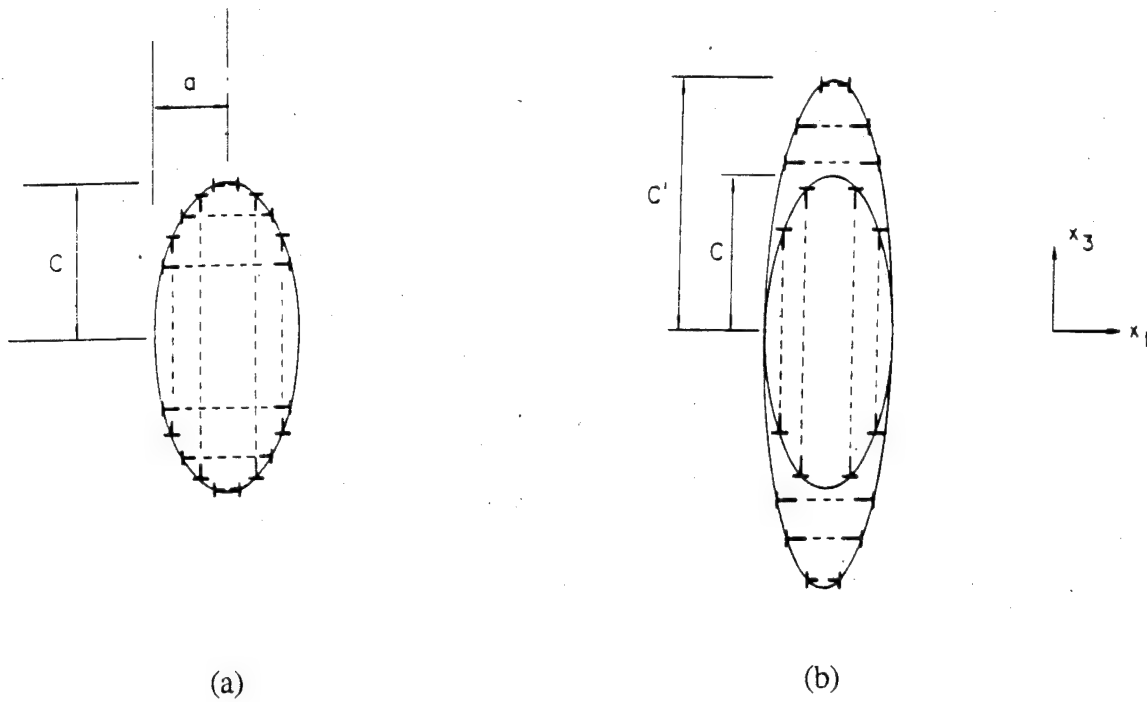


Figure 3.1 Analytical model used by Taya and Mori [12] to study the relaxation of CTE mismatch strain at short fiber/metal matrix interface by dislocation punching: (a) before punching (unrelaxed stage), (b) after punching (relaxed stage)

The stress field in and around a short fiber and the total strain energy of a short fiber MMC can be calculated if the following eigenstrains are given in the domains of fiber (Ω_1) and of the punched region encompassing the fiber (Ω_2):

$$\tilde{e}^{*1} = \begin{Bmatrix} e_T & 0 & 0 \\ 0 & e_T & 0 \\ 0 & 0 & 0 \end{Bmatrix} \text{ in } \Omega_1 \quad (3.5)$$

$$\tilde{e}^{*2} = \begin{Bmatrix} 0 & 0 & 0 \\ 0 & 0 & 0 \\ 0 & 0 & e_T \left(\frac{c}{c'} \right) \end{Bmatrix} \text{ in } \Omega_2 \quad (3.6)$$

where c' and c are the punching distance and half of short fiber length along the x_3 -axis, respectively, Fig. 3.1. The criterion for dislocation punching is given by

$$-\frac{\partial U}{\partial c'} = \frac{\partial W}{\partial c'} \quad (3.7)$$

where U is the total strain energy of the composite of Fig. 3.1(b) and its explicit expression is given elsewhere [12], and W is the total energy dissipation due to punching, i.e., plastic work required for the motion of the dislocation loops during punching and given by

$$W = \left(\frac{c}{a}\right) f k \left(\frac{c'}{c} - 1\right) e_T \quad (3.8)$$

where c/a is the fiber aspect ratio, k is the friction stress of the matrix metal against dislocation motion.

Eq. (3.7) provides the relations between punching distance (c') and several constituent parameters. Fig. 3.2 shows such an example, i.e. the punching distance (c') normalized by half of fiber length (c) as a function of fiber aspect ratio (c/a). Fig. 3.2 implies that the punching along the fiber axis would become more difficult as fiber aspect ratio increases. In this case, the punching is more likely to take place along the direction transverse to the fiber axis, as discussed in Section 3.3. The relaxation by dislocation punching results in lowering the stress field in around a short fiber. Table 3.1 shows the normal stress components (σ_{11} , σ_{22} and σ_{33}) normalized by 2μ where μ is the matrix shear modulus for relaxed (after punching) stage, Fig. 3.3(a) and non-relaxed (before punching) stage, Fig. 3.3(b). The stresses are calculated for several locations: within a fiber (A), just outside the fiber at equator (B) and just outside the fiber-ends (C). Table 3.1 indicates that the magnitude of the stress field in and around a short fiber in the relaxed stage indeed is smaller than that of the non-relaxed stage. The data used to compute the stress field (Table 3.1) and punching distance (Fig. 3.2) referred to SiC short fiber/Al system and are given elsewhere [12].

Table 3.1. Stress at points A, B and C (see Fig. 3)

$\frac{\sigma_{ij}}{2\mu} \times 10^{-2}$	For relaxed state			For non-relaxed state		
	11	22	33	11	22	33
A	-0.225	-0.225	-0.84	-0.245	-0.245	-1.184
B	-0.225	0.198	0.069	-0.245	0.213	0.119
C	0.0035	0.0035	-0.84	-0.149	-0.149	-0.184

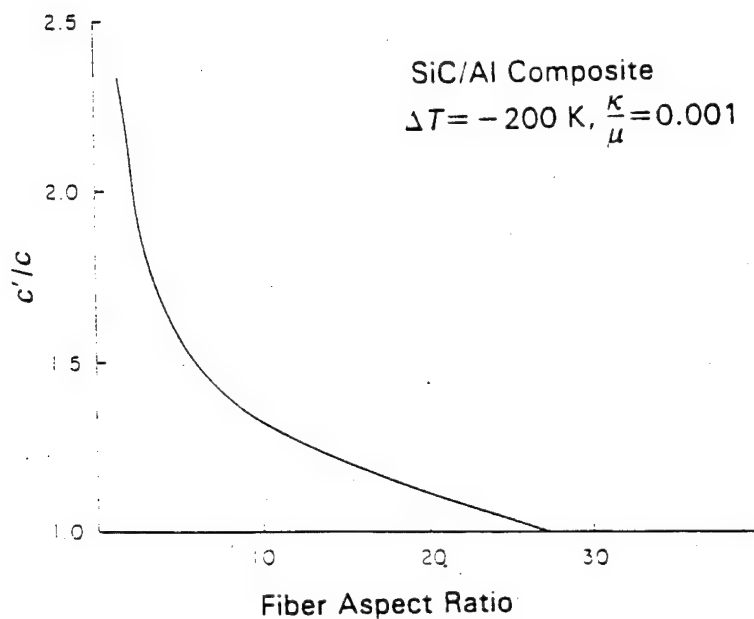


Figure 3.2 Punching distance (c') normalized by half of short fiber length vs. fiber aspect ratio (c/a) for SiC short fiber/Al matrix composite with $\Delta T = -200^\circ\text{C}$, $k/\mu = 0.001$.

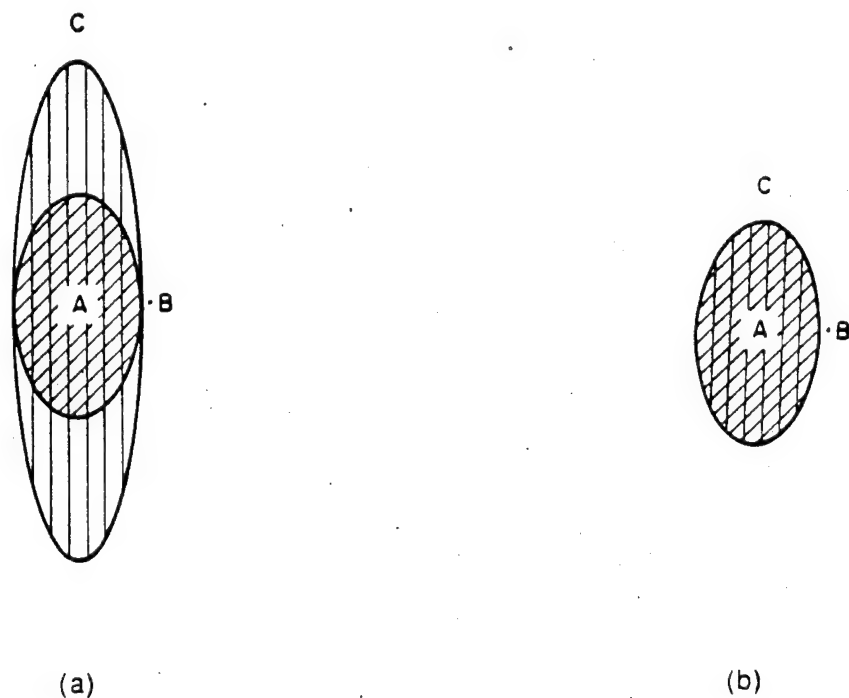


Figure 3.3 Stresses are calculated at points A, B, and C for (a) relaxed and (b) unrelaxed stages.

Dunand and Mortenson [13] modified the above model to account for partial relaxation by dislocation punching along the fiber axis. The eigenstrains based on this model are given by Eqs. (3.5) and (3.6) where (3,3) element in \tilde{e}^{*1} is replaced by $(1-\chi) e_T$ and that in \tilde{e}^{*2} by $\chi e_T \left(\frac{c}{c'} \right)$, where χ denotes the fraction of the misfit strain to be relaxed by dislocation punching. The modified model of Dunand and Mortenson appears to explain well their experimental results.

3.3 Dislocation Punching From a Spherical Particle

The dislocation punching from a spherical particle was studied both theoretically and experimentally by Taya et al. (1991). It is expected that the direction of dislocation punching from a spherical particle is spherically symmetric. Fig. 3.4(a), (b) and (c) show the CTE mismatch strain adhered to the particle-matrix interface as dislocation loops before punching, after punching, and the rearrangement of the dislocation loops, respectively. The dislocation punching shown by Fig. 3.4(b) should take a form of glide motion as illustrated by Fig. 3.5, i.e. during punching an edge dislocation is degenerated to two partial edge dislocations which move along the glide planes, and after punching, two edge dislocations are formed to one edge dislocation arrayed in a spherically symmetric manner. The eigenstrains representing the case of Fig. 3.4(b) (or Fig. 3.4(c)) are isotropic in a domain of punched spherical region including the particle (Ω_2) and given by

$$\tilde{e}^{*2} = \begin{Bmatrix} e_T \left(\frac{c}{c'} \right)^3 & 0 & 0 \\ 0 & e_T \left(\frac{c}{c'} \right)^3 & 0 \\ 0 & 0 & e_T \left(\frac{c}{c'} \right)^3 \end{Bmatrix} \quad (3.9)$$

The criterion for dislocation punching is given by Eq. (3.7). c' and c'' are defined by Fig. 3.4(b). The geometry after punching in a spherical particle MMC is shown schematically in Fig. 3.6 where (a) and (b) denote the case of extensive and less extensive punching, respectively. It is noted here that in the case of extensive punching, Fig. 3.6(a), the punched dislocations located at the boundary of Ω_2 are canceled out if they are overlapped with adjacent dislocations, resulting in no contribution of *geometrically necessary dislocations* to increase in the matrix flow stress. However, as the *geometrically necessary dislocations* are punched, *statistically stored dislocations* are left out in the wake region ($\Omega_2 - \Omega_1$) since the actual mode of the dislocation punching is not spontaneous, but successive punching of dislocation loops. Thus, for extensive punching, one can expect an increase in matrix flow stress due to the *statistically stored dislocations*.

The formulations of the stress and strain field, and also the strain energy of a composite, are again based on the Eshelby's method and its details are given elsewhere [5,14]. The average dislocation density for less extensive punching mode, Fig. 3.6(b) is given by

$$\bar{\rho} = \frac{6e_T f}{ab(1-f)} \quad (3.10)$$

where f is the volume fraction of particles, e_T is CTE mismatch strain, a is the radius of a spherical particle and b is Burgers' vector. A comparison between Eqs. (3.3) and (3.10) reveals that the averaged dislocation density in the matrix predicted by the Arseault and Shi model is twice as much as that by the Taya et al. model, if t is set equal to a . In the case of extensive punching, Fig. 3.6(a), the average dislocation density is computed by Shibata et al. (1992) and given by

$$\bar{\rho} = \frac{6fk\epsilon_T}{\mu b} \ln(f^{-1/3}) \quad (3.11)$$

It is noted that Eq. (3.11) was derived by accounting for only *statically stored dislocations*.

In order to predict the yield stress of a particle MMC, one should consider another strengthening mechanism, i.e. back stress strengthening which is to account for resistance of elastic particles against plastically deforming matrix metal. Hence the increase in the composite yield stress over the unreinforced metal is due to two mechanisms: dislocation punching as a result of relaxation of CTE mismatch strain at the interface ($\Delta\sigma_{CTE}$) and back stress ($\Delta\sigma_b$). In order to test the validity of the above strengthening mechanisms, Taya et al. [5] conducted experiment on SiC particle/6061 Al composite-T4 (SiC_p/Al). The mechanical properties of SiC_p/Al composite are given in Table 3.2.

Table 3.2. Material Properties

Parameter	Unit	Al Matrix	SiC Particle
Young's modulus	GPa	68.3	427
Yield strength	MPa	97.0	—
Poisson's ratio	1	0.33	0.17
CTE	$\times 10^{-6} \text{ C}$	23.6	4.3
Burgers' vector	nm	0.283	—
Average particle radius	μm	—	5.0

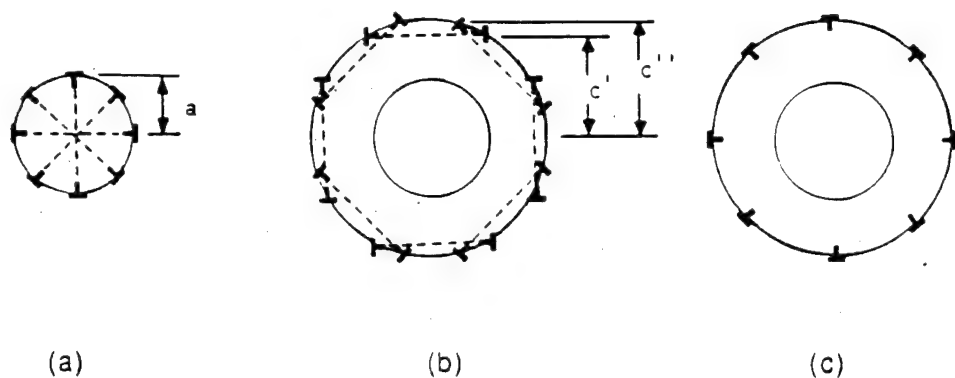


Figure 3.4 Dislocation punching model used by Taya et al. [5]: (a) CTE mismatch strain ϵ_T adhered to the particle/matrix surface as prismatic dislocation loops, (b) after punching to c' , (c) rearrangement of loops for spherical symmetry.

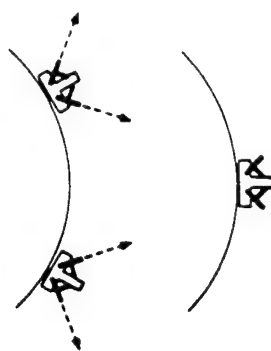


Figure 3.5 Dissociated dislocations make glide motion and are combined to form a new dislocation.

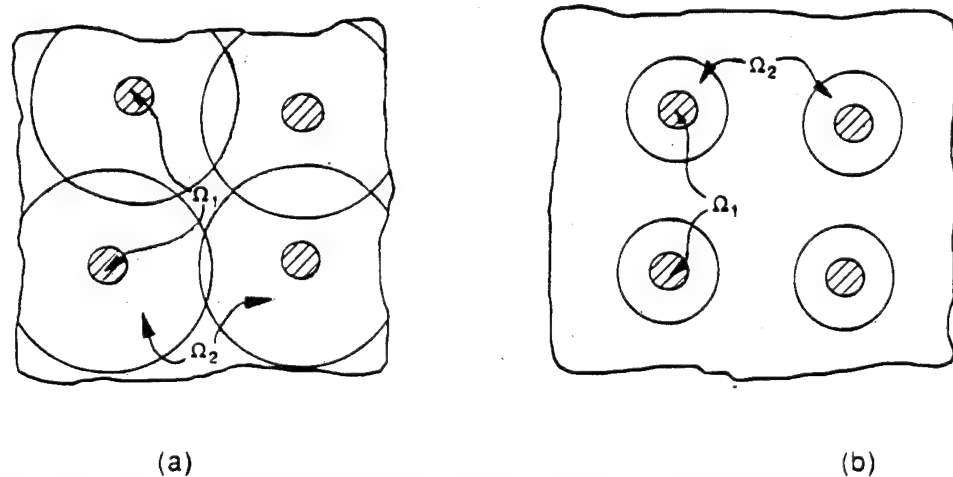


Figure 3.6 Punched regions in a particle MMC: (a) for extensive punching resulting in overlapping of the frontal boundaries and (b) for less extensive punching.

SiCp/Al specimens were solution-treated at 530°C, thus eliminating much of the dislocations induced by processing, then quenched to several different temperatures (T_q): room temperature, 0, -64, and -196°C, followed by tensile testing at these temperatures to measure the yield stresses. The purpose of quenching is to generate given CTE mismatch strain at the interface. Fig. 3.7(a) shows the composite yield stresses experimentally obtained (open circle) and predicted by the dislocation punching and backstress strengthening models (filled circle) as a function of temperature change by quenching, $\Delta T = T_q - 530$. In order to examine as to which strengthening mechanism is dominant, $\Delta\sigma_b$ and $\Delta\sigma_{CTE}$ are plotted in Fig. 3.7(b), indicating that $\Delta\sigma_{CTE}$ is larger than $\Delta\sigma_b$. Namely strengthening due to dislocation punching is dominant.

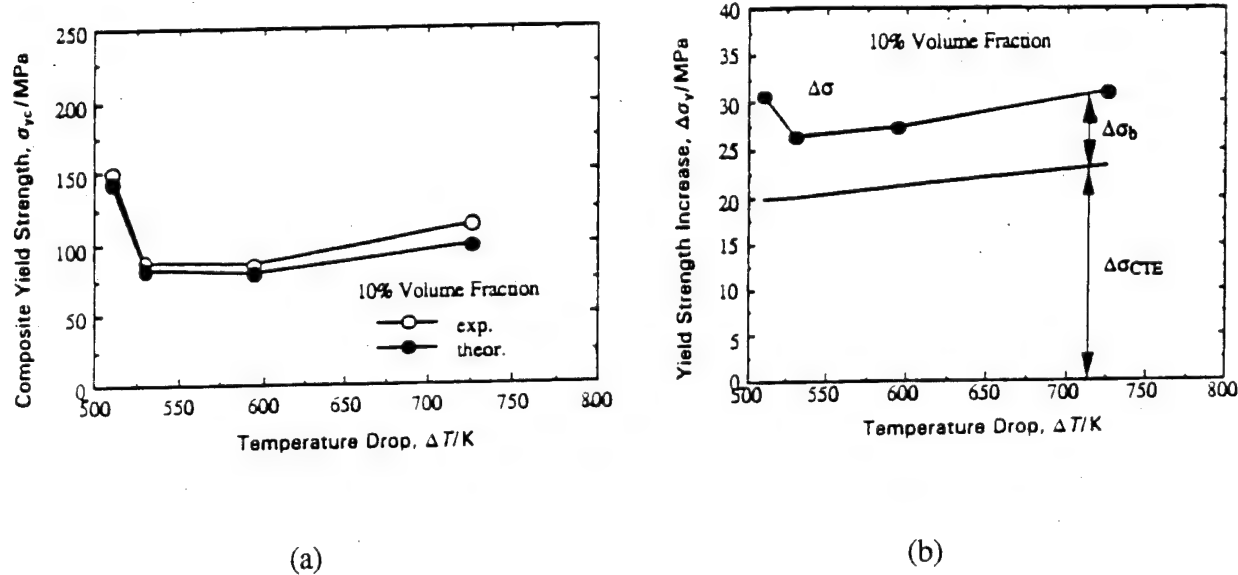


Figure 3.7 Composite yield stress vs. temperature change by quenching: (a) a comparison between the experiment and the prediction based on the dislocation punching model, (b) breakdown of the increase in the composite yield stress indicating strengthening due to dislocation punching ($\Delta\sigma_{CTE}$) dominant over that due to back stress ($\Delta\sigma_b$).

3.4 Dislocation Punching From a Continuous Fiber

As the results of Fig. 3.2 suggest, the dislocation punching from a continuous fiber in a continuous fiber MMC is more likely to take place along the transverse direction (transverse to the fiber axis). This was studied analytically by Shibata et al. [15]. The eigenstrains after punching are given by

$$\mathbf{e}^{*1} = \begin{Bmatrix} 0 & 0 & 0 \\ 0 & 0 & 0 \\ 0 & 0 & e_T \end{Bmatrix} \text{ in } \Omega_1 \quad (3.12)$$

$$\mathbf{e}^{*2} = \begin{Bmatrix} e_T \left(\frac{a}{R} \right)^2 & 0 & 0 \\ 0 & e_T \left(\frac{a}{R} \right)^2 & 0 \\ 0 & 0 & 0 \end{Bmatrix} \text{ in } \Omega_2 \quad (3.13)$$

where Ω_1 and Ω_2 denote the domains of the fiber and the punched region encompassing the fiber, respectively; a and R are the radii of the fiber and the punched region, respectively. By using the Eshelby's model to compute the total elastic energy of the composite and the criterion for punching, Eq. (3.7), and the dissipation energy for punching, one can obtain the punching distance (radius of the punched region) \bar{R} as

$$\bar{R} = a \left\{ \frac{(1 + 2\nu) \mu e_T}{2 (1 - \nu) k} \right\}^{1/2} \quad (3.14)$$

where μ and k are the shear modulus and friction stress of the matrix metal, respectively. Eq. (3.14) was obtained for a single continuous fiber embedded in an infinite matrix. The result of the punching distance \bar{R} for a continuous fiber MMC with finite volume fractions of fiber can be obtained similarly [15]. It is noted here that the yield criterion based on Hill's model

$$|\sigma_r - \sigma_\theta| = 2k \quad (3.15)$$

is not satisfied within the plastic domain ($\Omega_2 - \Omega_1$) where σ_r and σ_θ are radial and circumferential stress components. However, the average stress across the boundary of Ω_2 is defined by

$$\bar{\sigma}_{ij} = \lim_{\varepsilon \rightarrow 0} \left\{ \sigma_{ij}(R - \varepsilon) + \sigma_{ij}(R + \varepsilon) \right\} / 2 \quad (3.16)$$

satisfy the yield condition, Eq. (3.15) which gives rise to Eq. (3.14).

3.5 Dislocation Punching From a Planar Interface

The generation of dislocations at the interface of a thin coating/substrate system has been studied in terms of critical thickness of the coating-misfit strain relation [16,17]. These studies are aimed at epitaxial layers and the order of the critical thickness is normally much smaller, 10 ~ 100 nm. For a coated substrate system with non-epitaxial interface and intermediate coating thickness, the results of the above studies are not applicable.

Here we consider a metal thin coating/ceramic substrate with CTE driven misfit strain at the interface. The CTE misfit strain is defined by

$$e_{ij}^* = e^* \delta_{ij} \quad (3.17)$$

$$e^* = (\alpha_c - \alpha_s) \Delta T$$

where α_c and α_s are CTE of the coating and substrate, respectively, δ_{ij} is knocker's delta and ΔT is temperature change. First we examine the stress field before punching Fig. 3.8(a) and then the case of punching to some distance, Fig. 3.8(b).

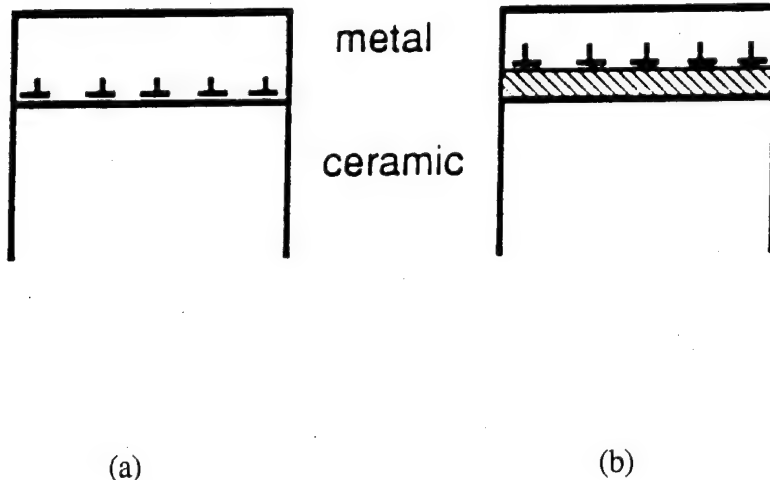


Figure 3.8 Dislocation punching model for a thin metal coating/ceramic substrate system: (a) before punching, (b) after punching to distance z .

It is assumed in this model that the thickness of coating is reasonably thin, so that out-of-plane stress component in the coating (σ_{33}) can be ignored, and also that the plane strain condition be held for in-plane directions, x_1 - and x_2 -axes within the coating.

Before Punching

By the assumption of plane strain along the x_1 - and x_2 -axes,

$$e_{11} = e_{22} = -e^* \quad (3.18)$$

where e_{ij} is elastic strain component. Hooke's law with $\sigma_{33} = 0$ gives rise to

$$\begin{aligned} e_{11} &= \frac{\sigma_{11}}{E} - \frac{v}{E} \sigma_{22} \\ e_{22} &= \frac{\sigma_{22}}{E} - \frac{v}{E} \sigma_{11} \\ e_{33} &= -\frac{v}{E} (\sigma_{11} + \sigma_{22}) \end{aligned} \quad (3.19)$$

where v is the Poisson's ratio of the coating.

From Eqs. (3.18) and (3.19) we obtain the in-plane stresses and out-of-plane strain as

$$\begin{aligned} \sigma_{11} = \sigma_{22} &= -\frac{E e^*}{(1 - v)} \\ e_{33} &= \frac{v}{1 - v} e^* \end{aligned} \quad (3.20)$$

Punching to Distance z

Assuming that the dislocation punching took place with its frontal boundary located Z from the interface, Fig. 3.8(b), we shall calculate the stress and strain field within the punched region (Ω_1) and elastic region (Ω_0) and also the condition for punching.

in Elastic Region (Ω_0):

Stress σ_{ij} and strain e_{ij} are the same as those in the coating before punching, i.e. given by Eq. (3.20).

in Plastic Region (Ω_1):

Denoting plastic strain in the punched region by e_{ij}^p and using the plane strain condition in the $x_1 - x_2$ plane and incompressibility of plastic strain, one arrives at

$$e_{11}^p = e_{22}^p = -e_T \quad (3.21)$$

$$e_{33}^p = 2e_T$$

and

$$\sigma_{ij} = 0 \quad (3.22)$$

It is noted that stresses in Ω_1 are all zero due to complete relaxation.

Computation of Elastic Energy U and Plastic Work W

The elastic energy per unit width along the x_2 -axis is given by

$$U = \frac{1}{2} \sigma_{ij} e_{ij} (\ell - z) \quad (3.23)$$

A substitution of Eqs. (3.18) and (3.20) into (3.23) yields

$$U = \frac{E e_T^2 (\ell - z)}{(1 - v)} \quad (3.24)$$

The plastic work per unit width, W is given by

$$W = \sigma_{ij} e_{ij}^p z \quad (3.25)$$

by using Eq. (3.21) and $\sigma_{11} = \sigma_{22} = \sigma_y$ (yield stress), W is reduced to

$$W = 4k e_T z$$

where $\sigma_y = 2k$ was used and k is yield stress in shear. The punching criterion is given by

$$-\frac{\partial U}{\partial Z} \geq \frac{\partial W}{\partial Z} \quad (3.26)$$

where the left term represents the driving force for punching while the right is the retarding force against punching. By substituting Eqs. (3.24) and (3.25) into (3.26) we obtain the condition for punching

$$e_T \geq \frac{4k(1-v)}{E} \quad (3.27)$$

Inequality (3.27) can be derived by invoking the yield criterion across the frontal boundary of the punched region, i.e. the interface between Ω_0 and Ω_1 , Fig. 3.8(b). The average stresses across the boundary are calculated by using Eqs. (3.16), (3.20) and (3.22).

$$\bar{\sigma}_{11} = \bar{\sigma}_{22} = -\frac{E e_T}{2(1-v)} \quad (3.28)$$

which is substituted into Hill's yield criterion

$$|\bar{\sigma}_{33} - \bar{\sigma}_{11}| \geq 2k \quad (3.29)$$

A substitution of Eq. (3.28) and $\sigma_{33} = 0$ into (3.29) leads to (3.27).

3.6 References

1. Hedges, S.M. and Mitchell, J.W., 1953, "Observation of Polyhedral Sub-Structure in Crystals of Silver Bromide," *Phil. Mag.*, Vol. 44, pp. 223-224.
2. Ashby, M.F. and Johnson, L., 1969, "On the Generation of Dislocations at Misfitting Particles in a Ductile Matrix," *Phil. Mag.*, Vol. 20, pp. 1009-1022.

3. Chawla, K.K. and Metzger, M. 1972, "Initial Dislocation Distribution in Tungsten Fibre-Copper Composites," *J. Mater. Sci.*, Vol. 7, pp. 34-39.
4. Vogelsang, M., Fischer, R.M. and Arsenault, R.J., 1986 "An In situ HVEM Study of Dislocation Generation at Al/SiC Interfaces in Metal Matrix Composites," *Metall. Trans.*, Vol. 17A, pp. 379-389.
5. Taya, M., Lulay, K.E., and Lloyd, D.J., 1991, "Strengthening of a Particulate Metal Matrix Composite by Quenching," *Acta Metall. Mater.*, Vol. 39, No. 1, pp. 73-87.
6. Shieh, F.S. and Sass, S.L., 1990, "Experimental and Theoretical Studies of the Dislocation Structure of NiO-Pt Interfaces," *Acta Metall. Mater.*, Vol. 38, No. 9, pp. 1653-1667.
7. Tanaka, K. and Mori, T. 1970, "The Hardening of Crystals by Non-Deforming Particles and Fibers," *Acta Metall.*, Vol. 18, pp. 931-
8. Eshelby, J.D. 1957, "The Determination of the Elastic Field of an Ellipsoidal Inclusion and Related Problems," *Proc. Roy. Soc.*, Vol. 241A, pp. 376-396.
9. Mura, T. 1987, *Micromechanics of Defects in Solids*, 2nd ed., Martinis Nijhoff.
10. Tanaka, K., Narita, K., and Mori, T., 1972, "Work Hardening of Materials with Strong Inclusions After Prismatic Punching," *Acta Metall.*, Vol. 20, p. 297.
11. Arsenault, R. J. and Shi, N., 1986, "Dislocation Generation due to Differences between the Coefficients of Thermal Expansion," *Mater. Sci. and Eng.*, 81, pp. 175-187.
12. Taya, M. and Mori, T., 1987, "Dislocations Punched Out Around a Short Fiber in a Short Fiber Metal Matrix Composite Subjected to Uniform Temperature Change," *Acta Metall.*, Vol. 35, p. 155.
13. Dunand, D.C. and Mortensen, A., 1991, "On the Relaxation of a Mismatching Spheroid by Prismatic Loop Punching," *Scripta Metall. Mater.*, Vol. 25, pp. 761-766.
14. Shibata, S., Taya, M., Mori, T., and Mura, T., 1992, "Dislocation Punching from Spherical Inclusion in a Metal Matrix Composite," *Acta Metall. Mater.*, Vol. 40, No. 11, pp 3141-3148.
15. Shibata, S., Mori, T., and Taya, M., 1992, "Stress Relaxation by Dislocation Punching to Radical Direction from a Long Fiber in a Composite," *Scripta Metall. Mater.*, Vol. 26, pp. 363-368.
16. Matthews, J.W. and Blakesee, A.E., 1974, "Defects in Epitaxial Multilayers," *J. Crystal Growth*, Vol. 27, pp. 118-125.
17. Freund, L.B., 1987, "The Stability of a Dislocation Threading a Strained Layer on a Substrate," *J. Applied Mech.*, Vol. 54, pp. 553-557.

4. Analytical Study II: Dimensional Change of MMCs

4.1 Analytical Model for Short Fiber Composites

4.1.1 Introduction

Dimensional stability in high temperature use environments is crucial for many metal matrix composite (MMC) applications. While MMCs reinforced by ceramic fibers offer creep resistance superior to the unreinforced metal, it is well known that the combination of relatively small applied stresses and cyclic thermal loading can result in creep rates far in excess of those observed during isothermal high temperature creep. Even in the absence of an applied stress, a detrimental dimensional change has been observed in a number of thermal cycled metal matrix composite systems. These effects are attributed to internal stresses that are developed during thermal cycling due to the coefficient of thermal expansion mismatch between the matrix and fibers. Creep and thermal cycling creep are among the least understood aspects of the deformation of MMCs, but are of utmost importance for the development of MMCs for high temperature structural applications.

Creep in short fiber metal matrix composites has been studied both experimentally and theoretically by numerous researchers. A comprehensive review is not attempted here, but the reader is referred to recent reviews by Taya [1] and Taya and Arsenault [2]. Recent works regarding modeling of creep of short fiber composites include Zhu and Weng [3-5], Wang and Weng [6], and Pan and Weng [7]. In these works, Eshelby's equivalent inclusion method [8] was combined with the Mori-Tanaka mean field approach [9] to estimate the stress redistribution due to an incremental creep of the metal matrix and the subsequent creep deformation of the composite. A similar approach was used by Taya and Mori [10] to model creep of a short fiber MMC during the high temperature hold stage of a cyclic thermal loading. With regards to thermal cycling and thermal cycling creep of short fiber MMCs, Derby [11] and Taya et al. [12] have recently provided a comprehensive review of the literature and a list of references with regards to both experimental and theoretical aspects can be found therein. Other recent contributions have been directed at understanding the effects of reinforcement geometry on the thermal cycling creep of short fiber MMCs through the development of idealized models and the application of finite element methods [13-15].

During isothermal creep of a MMC, degradation of the fiber matrix interface, often in the forms of void nucleation and growth followed by debonding, has been observed to lead to tertiary creep and creep fracture [16-19]. The accumulation of inelastic strain during thermal cycling has also been observed to be accompanied by the development of interfacial damage in the forms of

porosity, debonding, and an attached reaction zone containing radial cracks [20]. These damage processes, in both isothermal and thermal cycling creep further accelerate the inelastic strain accumulation and thus it is important to understand the evolution of damage and its effect on the overall response of the MMC.

This work is a continuation of the authors' study of creep, thermal cycling, and creep thermal cycling (thermal cycling with an applied stress) of metal matrix composites. In particular, a micromechanics-based analytical approach is proposed to model creep and thermal cycling creep of short fiber MMCs with interfacial damage. The approach is an extension of the analyses of Taya et al. [12] for creep, Taya and Mori [10] for thermal cycling, and Dunn and Taya [21] for creep thermal cycling of MMCs and is based on the combination of Eshelby's equivalent inclusion method [8] and the Mori-Tanaka mean field approach [9] (see for example [22]). Interfacial damage is modeled through a hybrid approach where the composite is assumed to contain both perfectly bonded fibers and fibers with damaged interfaces. The evolution of damage is described by an arbitrary statistical distribution. Efforts to correlate the statistical distribution of interfacial damage with experiment are currently underway and the results will be subsequently reported.

4.1.2 Analytical Model

It is assumed that initially all fibers are perfectly bonded to the matrix. At some point during the creep or thermal cycling creep loading, though, interfacial damage begins to occur. The effect of the damage is a loss in the ability to effectively transfer load from the matrix to the fibers. When damage has occurred, it is assumed that the aligned short fiber and matrix are still in mechanical contact except at and near the poles of the fibers. This characterization is based on numerous reports from the literature regarding debonding during creep and a microscopy study of thermal cycled W/FeCrAlY short fiber composites of which a typical micrograph is shown in Fig. 4.1 [23]. The fiber-matrix interface is assumed to be stress free in the x_3 direction but not in the x_1 and x_2 direction except in the vicinity of the fiber ends. This assumption seems reasonable when the interface between the short fiber is in tension, but may not be as valid when the stress field at the interface is compressive. These implications will be further discussed in the following section. The stress field in the debonded fibers is analyzed by following the approach proposed by Tanaka et. al. [24] to model the stress distribution in a spherical particle after cavitation. The stress field in the debonded fibers is simulated by that of a fictitious fiber with anisotropic moduli of $C_{ijkl}^d = 0$ with the exception of $C_{1111}^d = C_{2222}^d$ and $C_{1122}^d = C_{2211}^d$. It is noted that this reduction in moduli is only valid for the case considered here, aligned short fibers subjected to uniaxial mechanical loading along the axis of the fiber.

In this section, the response of a composite containing two types of short fibers (perfectly bonded and debonded) will be obtained. The debonded fibers are assumed to be described as discussed in the previous section and the criterion for progressive debonding will then be discussed in the following section. The domain of the analytical model, shown in Fig. 4.2, consists of an infinite metal matrix containing a random distribution of both perfectly bonded and debonded aligned short fibers. The domains of the entire composite and of the bonded and debonded fibers are denoted by D , Ω_b , and Ω_d respectively, and that of the matrix is thus denoted by $D - \Omega_b - \Omega_d$. The elastic moduli of the matrix and two types of fibers are C_m , C_b , and C_d , respectively. It is noted that C_m and C_b are defined in the standard manner while C_d has been defined in Section 2. In this work, bold and underscored symbols represent tensorial quantities. Both types of fibers are modeled as ellipsoidal inhomogeneities (prolate spheroids) and for simplicity both the matrix and fibers are assumed to be initially isotropic in stiffness and thermal expansion. To model the creep response of the composite, a constant applied stress, $\underline{\sigma}_o$, is assumed and in addition the idealized time-temperature thermal cycle shown in Fig. 4.3 is assumed during thermal cycling creep. It is assumed that the fibers deform elastically and the matrix is capable of elastic/plastic/creep deformations. The material properties, with the exception of the yield stress and creep properties of the matrix, are assumed independent of temperature. This assumption can be relaxed, however, and the analysis can be easily implemented in an incremental manner.

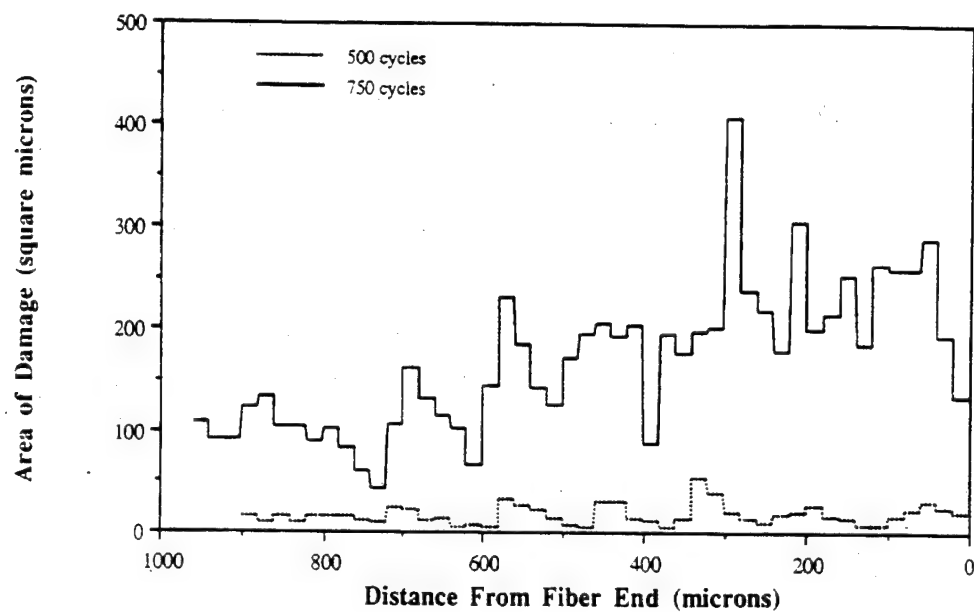
Creep of Short Fiber Metal Matrix Composites

Response to the Applied Stress

The overall response of the composite to the uniform applied stress, $\underline{\sigma}^o$, (with corresponding strain e^o) can be estimated by the use of Eshelby's equivalent inclusion method [8] coupled with the Mori-Tanaka mean field approach [9] as applied to a three-phase composite [25]. Through the equivalent inclusion method, the stress in a single representative perfectly bonded fiber is given by:

$$\underline{\sigma}^o + \underline{\sigma}^b = C_b [e^o + \bar{e} + e^b] = C_m [e^o + \bar{e} + e^b - e^{*\sigma_b}] \quad (4.1)$$

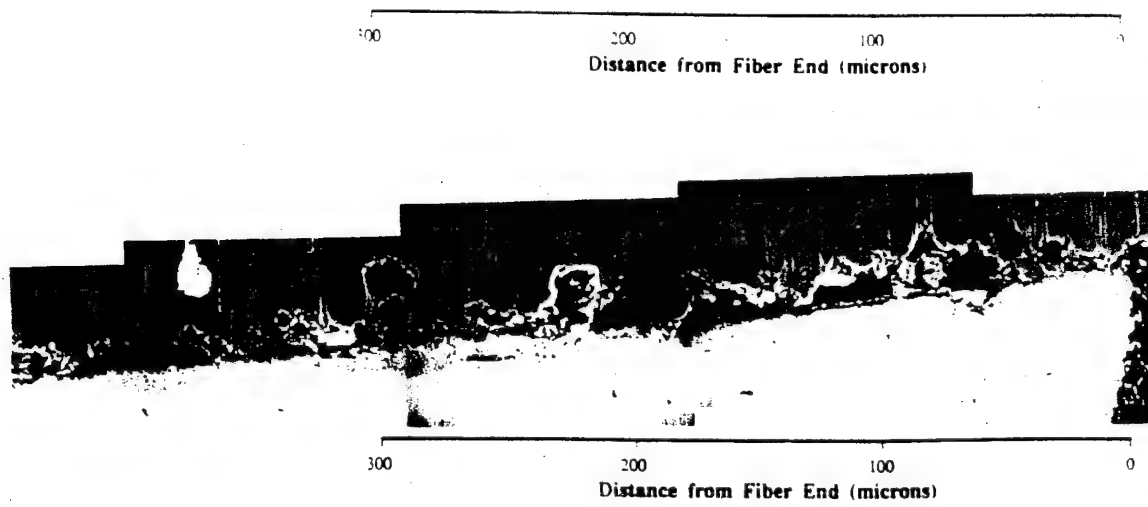
That in a single representative debonded fiber is given by:



(a)



(b)



(c)

Figure 4.1 Debonding of the interface in a short W fiber/FeCrAlY matrix composite subjected to thermal cycling: (a) area of interfacial damage, (b) SEM photograph at N=500 and (c) N=750.

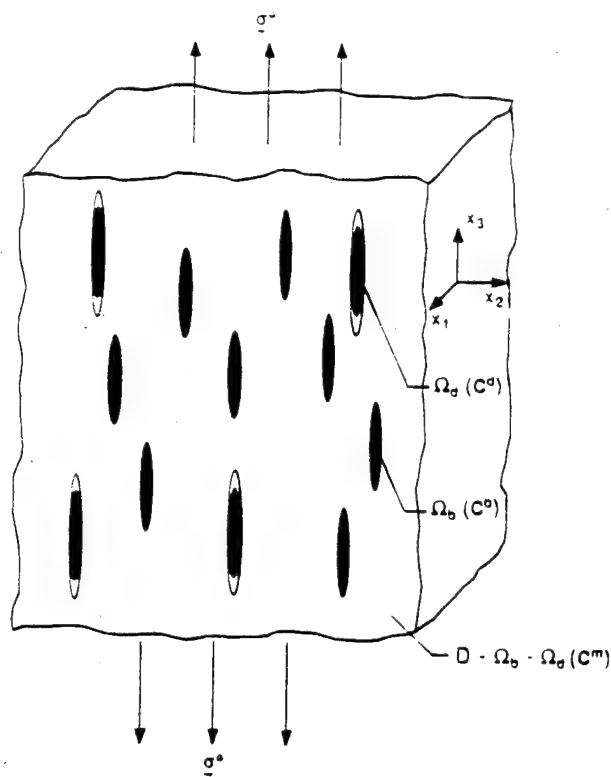


Figure 4.2 Analytical model.

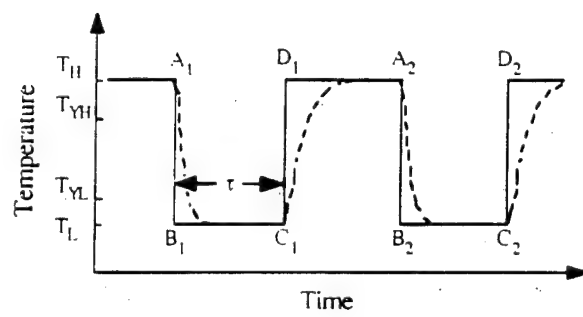


Figure 4.3 Idealized temperature-time relation.

$$\underline{\underline{\sigma}}^0 + \underline{\underline{\sigma}}^d = C_d [e^0 + \bar{e} + e^d] = C_m [e^0 + \bar{e} + e^d - e^{*\sigma_d}] \quad (4.2)$$

where \bar{e} is the volume averaged disturbance strain in the matrix and e^i and $e^{*\sigma_i}$ are the disturbance strain and fictitious eigenstrain in the i th domain ($i=b,d$) required for the simulation of the inhomogeneities by the equivalent inclusion, respectively. These can be expressed as:

$$\langle \underline{\underline{\sigma}} \rangle_m = C_m \cdot \bar{e} \quad (4.3)$$

$$e^i = S \cdot e^{*\sigma_i} \quad (4.4)$$

where S is Eshelby's tensor [8] and $\langle \underline{\underline{\sigma}} \rangle_m$ is the volume average of the disturbance stress (due to both Ω_b and Ω_d) in the matrix. Eshelby's tensor is a function only of the shape of the inhomogeneity and the elastic moduli (Poisson's ratio for isotropic materials) of the matrix and thus is the same for both the bonded and debonded fibers. It is not difficult to show that the volume average of $\underline{\underline{\sigma}}^i$ over the entire composite vanishes which results in:

$$\bar{e} = (S - I) \cdot [f_b e^{*\sigma_b} + f_d e^{*\sigma_d}] \quad (4.5)$$

where f is the volume fraction of fibers. After some manipulation, eqs. (4.1) - (4.5) yield $\langle \underline{\underline{\sigma}} \rangle_m$ which can be used to obtain the average stresses and strains in each phase and in the composite. Of particular interest are the average stress in the *matrix*, $\langle \underline{\underline{\sigma}} \rangle_m^0$, and the average strain of the *composite*, $\langle e \rangle_c^0$, which can be expressed as:

$$\langle \underline{\underline{\sigma}} \rangle_m^0 = R(C_m, C_b, C_d, S, f_b, f_d) \cdot \underline{\underline{\sigma}}^0 \quad (4.6)$$

$$\langle e \rangle_c^0 = H(C_m, C_b, C_d, S, f_b, f_d) \cdot \underline{\underline{\sigma}}^0 \quad (4.7)$$

Response to an Incremental Creep

An incremental creep of the matrix, de^C , results in a redistribution of stress from the creeping matrix to the elastic fibers, but as noted by Weng [26], is itself a stress-free process. Thus, Eshelby's equivalent inclusion method can be used to estimate the stress redistribution due to an incremental creep:

$$d\tilde{\sigma}^b = C_b \cdot [d\bar{\epsilon} + de^b + de^C] = C_m \cdot [d\bar{\epsilon} + de^b - de^{*C_b}] \quad (4.8)$$

$$d\tilde{\sigma}^d = C_d \cdot [d\bar{\epsilon} + de^d + de^C] = C_m \cdot [d\bar{\epsilon} + de^d - de^{*C_d}] \quad (4.9)$$

de^C and de^{*C_i} are the incremental creep of the matrix and the corresponding incremental eigenstrain and all other stress and strain increments are analogous to their previous definitions in eqs.(4.1) and (4.2). By a development similar to that used to obtain eqs. (4.6) and (4.7), the average stress increment in the matrix and strain increment of the composite due to an incremental creep of the matrix, de^C , can then be expressed as:

$$\langle d\tilde{\sigma} \rangle_m^{e^C} = U(C_m, C_b, C_d, S, f_b, f_d) \cdot de^C \quad (4.10)$$

$$\langle de \rangle_c^{e^C} = V(C_m, C_b, C_d, S, f_b, f_d) \cdot de^C \quad (4.11)$$

where due to the assumption of incompressibility and symmetry of deformation, de^C is given by $de^C = [-de^C/2, -de^C/2, de^C, 0, 0, 0]^T$.

For simplicity, the creep rate of the matrix is assumed to be described by the Mises J_2 creep flow rule Odqvist [27]:

$$\dot{\epsilon}_{ij}^C = k J_2^m \langle \sigma'_{ij} \rangle_m \text{ or } \dot{\epsilon}^C = \pm A |\sigma_m|^n \quad (4.12)$$

where $de^C = \dot{\epsilon}^C dt$. In eq. (4.12), J_2 , $\langle \sigma'_{ij} \rangle_m$, and σ_m are the second invariant, deviatoric components, and the flow stress of the average stress in the matrix and are all computed in the standard manner and as usual the (+) or (-) sign corresponds to the sign of the flow stress. The second of eqs. (4.12) results when axisymmetric deformation is present as will be assumed here. During creep of the matrix, the average stress in the matrix can be determined by integration of eq.

(4.12) with the initial condition of eq. (4.6). From the average stress in the matrix, the flow stress is determined as a function of ε^C , which in turn is a function of time. The flow stress can then be substituted into the power law of eq. (4.12) to yield a first order nonlinear ordinary differential equation in ε^C of the form:

$$\dot{\varepsilon}^C = A [(a \sigma^0 + b \varepsilon^C)]^n \quad (4.13)$$

For the applied uniaxial stress along the fiber (x_3) axis, the solution to the ODE of eq. (13) is:

$$\varepsilon^C(t) = \frac{1}{c} \left\{ (a \sigma^0)^{(1-n)} + (1 - n) A b t \right\}^{1/(1-n)} - \frac{a}{b} \sigma^0 \quad (4.14)$$

where a and b are functions of C_m , C_b , C_d , S , f_b , and f_d . It is noted that n is assumed to be independent of stress. This assumption can easily be relaxed to include the functional dependence of n on stress, however the resulting differential equation must then be integrated numerically. Finally, the creep strain of the composite is related to that of the matrix, $\varepsilon^C(t)$, through eq. (4.11).

Progressive Debonding

The model developed thus far is valid for an arbitrary combination of short fibers with bonded and damaged interfaces. The goal of this approach is to predict the progression of damage and its subsequent effect on the behavior of the composite. In other words, it is desired to understand how f_d , which is initially zero, evolves with the accumulation of inelastic strain. Here an attempt is made to relate f_d to the strength of the fiber-matrix interface through a statistical distribution function, the form of which will be obtained from careful experiment. Here it is assumed that the evolution of f_d can be described by the use of a three-parameter Weibull distribution as:

$$f_d = F(\sigma_{ib}) f_{tot} \quad (4.15)$$

where f_{tot} is the total volume fraction of fibers, i.e., $f_{tot} = f_b + f_d$ and $F(\sigma_{ib})$ is the cumulative density function:

$$F(\varepsilon_{tot}) = 1 - \exp \left[- \left(\frac{\sigma - \sigma_{ib}}{\theta - \sigma_{ib}} \right)^b \right] \quad \sigma \geq \sigma_{ib} \quad (4.16)$$

where b , σ_{ib} , and θ are the shape parameter, guaranteed value of σ (the stress σ_{33} at the interface), and the scale parameter respectively. Thus, f_d is a function of σ_{33} which is in turn a function of

time as σ_{33} increases as stress is redistributed from the creeping matrix to the elastic fibers. Equation (4.13) is still valid, but now it must be integrated numerically as a and b are now functions of time. Although a Weibull distribution is used here, it is emphasized that the proposed model is easily able to handle an arbitrary statistical distribution.

Thermal Cycling Creep of Short Fiber Metal Matrix Composites

In this section the development of an approach to model thermal cycling creep of short fiber metal matrix composites is outlined. The model extends that of Dunn and Taya [21] for thermal cycling creep of undamaged short fiber composites to model the effects and progression of interfacial damage in the same manner as was done with regards to isothermal creep in the previous section. Thus, only a brief outline of the approach will be given and the reader is referred to Dunn and Taya [21] for additional details.

The composite subjected to thermal cycling creep is assumed to be subjected a constant applied stress and then the idealized thermal cycle shown in Fig. 4.3. The initial response to the applied stress at A_1 of Fig. 4.3 is identical to that described in Section 4.2.1. During cooling (A_1 to B_1), the composite is subjected to the uniform temperature drop $\Delta T = T_L - T_H$ which induces a non-uniform thermal stress field in the composite due to the mismatch in coefficients of thermal expansion (CTEs) between the matrix and fibers. By use of the equivalent inclusion method, the inhomogeneities with thermal strain $e^{\Delta T}$ can be simulated by equivalent inclusions with fictitious eigenstrains $e^{*\Delta T}$ to yield:

$$\underline{\sigma}^b = C_b \cdot [\bar{e} + e^b - e^{\Delta T}] = C_m \cdot [\bar{e} + e^b - e^{*\Delta T} b] \quad (4.17)$$

$$\underline{\sigma}^d = C_d \cdot [\bar{e} + e^d - e^{\Delta T}] = C_m \cdot [\bar{e} + e^d - e^{*\Delta T} d] \quad (4.18)$$

where $e^{\Delta T} = (\alpha_b - \alpha_m) \Delta T$ is a result of the mismatch between the CTEs of the matrix, α_m , and the bonded and debonded fibers, $\alpha_b = \alpha_d$.

In a manner similar to that used to obtain eqs. (4.6) and (4.7), the average thermoelastic stress, $\underline{\sigma}_m^{\Delta T}$, and strain, $\underline{e}_c^{\Delta T}$, due to $e^{\Delta T}$ can be obtained as:

$$\underline{\sigma}_m^{\Delta T} = P(C_m, C_b, C_d, S, f_b, f_d, \alpha_b, \alpha_m) \Delta T \quad (4.19)$$

$$\underline{e}_c^{\Delta T} = Q(C_m, C_b, C_d, S, f_b, f_d, \alpha_b, \alpha_m) \Delta T \quad (4.20)$$

It is assumed that the temperature drop from T_H to T_L is sufficient to initiate uniform yielding of the matrix metal. The critical temperature change at which yielding of the matrix begins, $\Delta T_{cr}^L = T_H - T_{YL}$, can be found by subjecting the average thermoelastic stress in the matrix to the yield criterion:

$$3/2 \langle \underline{\sigma}' \rangle_m \cdot \langle \underline{\sigma}' \rangle_m = \sigma_{YL}^2 \quad (4.21)$$

where $\langle \underline{\sigma}' \rangle_m$ is the deviatoric portion of the thermoelastic stress and σ_{YL} is the yield stress of the matrix at T_L . When the applied stress is uniaxial along the x_3 -axis, the critical temperature change required for yielding of the metal matrix can then be expressed as:

$$\Delta T_{cr} = \frac{\sigma_{YL} - (R_{33} - R_{31}) \sigma^0}{P_3 - P_1} \quad (4.22)$$

The temperature drop from T_{YL} to T_L will then result in plastic deformation of the matrix.

To compute the plastic deformation, it is assumed that the temperature drop from T_{YL} to T_L induces a uniform plastic strain, e^{PL} , in the matrix and that the matrix is a non-hardening material. The assumption of a uniform plastic strain in the matrix neglects the effects of microyielding that is known to occur near the fiber-matrix interface upon relatively low temperature changes. It is the average stress field in the matrix, however, that is believed to influence the *macroscopic* deformation of the composite and this is the basis for the proposed approach. The uniform plastic strain, e^{PL} , is assumed to satisfy the incompressibility requirement $e_{ii}^{PL} = 0$ and as a result of symmetry (of both loading and microstructure) can be expressed as $e^{PL} = \epsilon^{PL} [-1/2, -1/2, 1, 0, 0, 0]^T = \epsilon^{PL} K$. The stress field due to e^{PL} can be computed by use of Eshelby's equivalent inclusion method where $e^{\Delta T}$ and $e^{*\Delta T}$ in eqs. (4.17) and (4.18) are replaced by $-e^{PL}$ and e^{*PL} respectively. The plastic strain, e^{PL} , can be determined by applying the yield criterion to the unknown *total* stress existing at T_L (B_1). With the plastic strain, e^{PL} , known, the average stress in the matrix and strain of the composite at B_1 can be expressed as:

$$\langle \underline{\sigma} \rangle_m^{B_1} = \langle \underline{\sigma} \rangle_m^{\sigma^0} + \langle \underline{\sigma} \rangle_m^{\Delta T} + \langle \underline{\sigma} \rangle_m^{e^{PL}} = R \cdot \underline{\sigma}^0 + P \cdot \Delta T + U \cdot e^{PL} \quad (4.23)$$

$$\langle \underline{e} \rangle_c^{B_1} = \langle \underline{e} \rangle_m^{\sigma^0} + \langle \underline{e} \rangle_m^{\Delta T} + \langle \underline{e} \rangle_m^{e^{PL}} = H \cdot \underline{\sigma}^0 + Q \cdot \Delta T + V \cdot e^{PL} \quad (4.24)$$

where U and V are defined by eqs. (4.10) and (4.11). During the low temperature plateau, $B_1 \rightarrow C_1$, no further deformations are assumed to occur and thus eqs. (4.8) and (4.9) describe the state of the composite at C_1 .

The thermoelastic stress developed during the heating process, $C_1 \rightarrow D_1$, is equal in magnitude but of opposite sign to that generated upon cooling. Reverse yielding, resulting in plastic strains ϵ^{PH} , may or may not occur depending on the values of σ_{YL} , the yield stress at T_H (σ_{YH}), and ΔT . The state of the composite at D_1 can be determined in the same manner as that upon cooling to yield:

$$\langle \sigma \rangle_m^{D_1} = R \cdot \sigma^o + U \cdot [\epsilon^{PL} + \epsilon^{PH}] \quad (4.25)$$

$$\langle e \rangle_c^{D_1} = H \cdot \sigma^o + V \cdot [\epsilon^{PL} + \epsilon^{PH}] \quad (4.26)$$

During the high temperature plateau, $D_1 \rightarrow A_2$, it is assumed that the flow stress existing at T_H (D_1) is further relaxed by bulk creep of the matrix. For simplicity, it is assumed that the creep properties of the composite matrix are the same as those of the unreinforced matrix alloy. Eshelby's equivalent inclusion method can be used to estimate the stress redistribution due to an incremental creep in the same manner as described in Section 4.2.1. Again the creep rate of the matrix is assumed to be described by eq. (4.12) which is integrated in the same manner outlined in Section 4.2.1 but now with the initial conditions of eq. (4.26) to provide the creep strain at the end of the high temperature plateau ($t = \tau$). Once $\epsilon^C(\tau)$ is obtained the overall state of the composite is:

$$\langle \sigma \rangle_m^{A_2} = R \cdot \sigma^o + U \cdot [\epsilon^{PL} + \epsilon^{PH} + \epsilon^C(\tau)] \quad (4.27)$$

$$\langle e \rangle_c^{A_2} = H \cdot \sigma^o + V \cdot [\epsilon^{PL} + \epsilon^{PH} + \epsilon^C(\tau)] \quad (4.28)$$

The stress-strain-time histories during the second and subsequent thermal cycles are computed in the same manner as that of the first thermal cycle except for the provision of a possible non-zero residual stress at A_2 which is easily accommodated. It turns out that the flow stress at the end of each subsequent thermal cycle is then the same as that at the end of the first.

Finally, a statistical distribution can be implemented to describe the progression of damage in a manner similar to that in Section 4.2.1. For the calculations presented in the following section, a three-parameter Weibull distribution is again used where here the cumulative density function is assumed to be a function of the accumulated inelastic strain. It is reiterated that the form of the statistical distribution has only been assumed and its precise form will be determined from careful experimental efforts which are presently underway. It is noted that the fiber-matrix interface is in compression during cooling and tension during heating [28]. Thus as damage evolves, it is probably more appropriate to use $f_{tot} = f_b + f_d$ during the heating portion of the thermal cycle and $f_{tot} = f_b$ during the cooling portion.

4.1.3 Sample Calculations

To illustrate, numerical computations have been performed using material properties typical of SiC whisker reinforced 6061-T6 Al as given by Morimoto et al. [17]. Unless otherwise noted, the creep thermal cycling parameters used are: $2\tau = 200$ s, $\Delta T = 350$ K, $\sigma_0 = 10$ MPa, α (aspect ratio) = 5, and $f_{tot} = .2$. The material properties used are $E_{Al} = 67.6$ GPa, $v_{Al} = .33$, $\alpha_{Al} = 24.7 \times 10^{-6}$ /K, $E_{SiC} = 427$ GPa, $v_{SiC} = .17$, $\alpha_{Al} = 4.3 \times 10^{-6}$ /K, $A_{Al} = 1.26 \times 10^{-16}$ Paⁿ/S, $n_{Al} = 4.88$.

Fig. 4.4 shows the predicted creep strain versus time for a total volume fraction of reinforcement, $f_{tot} = .15$, at various levels of debonding, $f_{tot} = .15$. It is seen that even though the matrix is assumed to be in steady-state creep, the composite exhibits a period of transient creep. It is readily apparent that the presence of debonded fibers dramatically affects the creep behavior of the MMC. Also shown in Fig. 4.4 are experimental results for a SiC whisker/6061-T6 Al short fiber composite which fall between the predictions for significant debonding. The analytical prediction for the stress at the fiber-matrix interface at time, $t=0$, is $\sigma_{ib} = 257$ MPa which significantly exceeds the ultimate strength of unreinforced 6061-T6 Al at 573K. It is thus likely that significant debonding existed from the onset which agrees with the predictions of the proposed model. In Fig. 4.5, the capabilities of the present model with regards to the effects of fiber-matrix debonding are illustrated. Fiber-matrix debonding is assumed to be described by the Weibull statistics of eqs. (4.15) and (4.16) where it is assumed that $\sigma_{ib}^0 = 180$ MPa (roughly twice the ultimate strength of 6061-T6 Al at 573K) corresponding to a fairly strong bond. The effects of the Weibull shape parameter on the creep strain of the composite are shown in Fig. 4.5 where the corresponding Weibull probability and cumulative density functions are shown in the inset. It is readily seen that the proposed approach allows simulation of the entire creep strain vs. time curve of an aligned short fiber composite with the exception of the creep rupture strain.

In Fig. 4.6, the accumulated strain as a function of the number of thermal cycles is shown for various values of f_d for a SiC/Al MMC subjected to thermal cycling creep loading. The highly nonlinear response as a function of f_d is clearly evident. The progression of damage appears as a jumping from the bottom line in Fig. 4.6 ($f_d = 0$) up to higher values of f_d with increasing N resulting in an overall nonlinear response of the composite. This is in qualitative agreement with experimental findings of Yoda et al.[29] and Armstrong et al. [23] for thermal cycling. The predicted accumulated strain of the composite subjected to creep only at T_H , based on the present theory (eqs. (4.8) - (4.14)) is far less than those under thermal cycling creep loadings, thus cannot be plotted in Fig. 4.6 (it would be almost zero in this scale of Fig. 4.6). It is clear that thermal cycling creep results in accumulated strains far in excess of those from isothermal creep which is consistent with numerous experimental reports. Finally, the effects of progressive damage are illustrated in Fig. 4.7 by employing the statistical description assumed in the previous section for

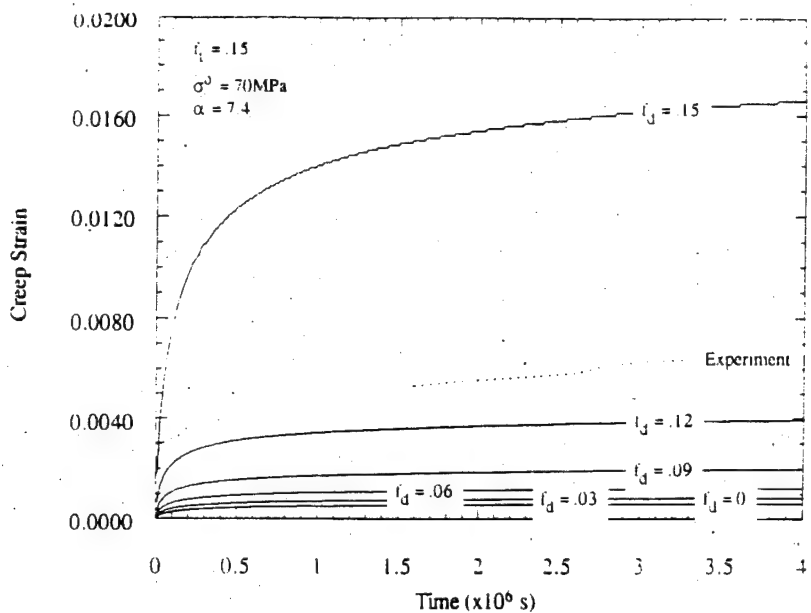


Figure 4.4 Predicted creep strain-time relation of a SiC whisker/6061 Al matrix composite for various volume fraction of debonded fiber (f_d).

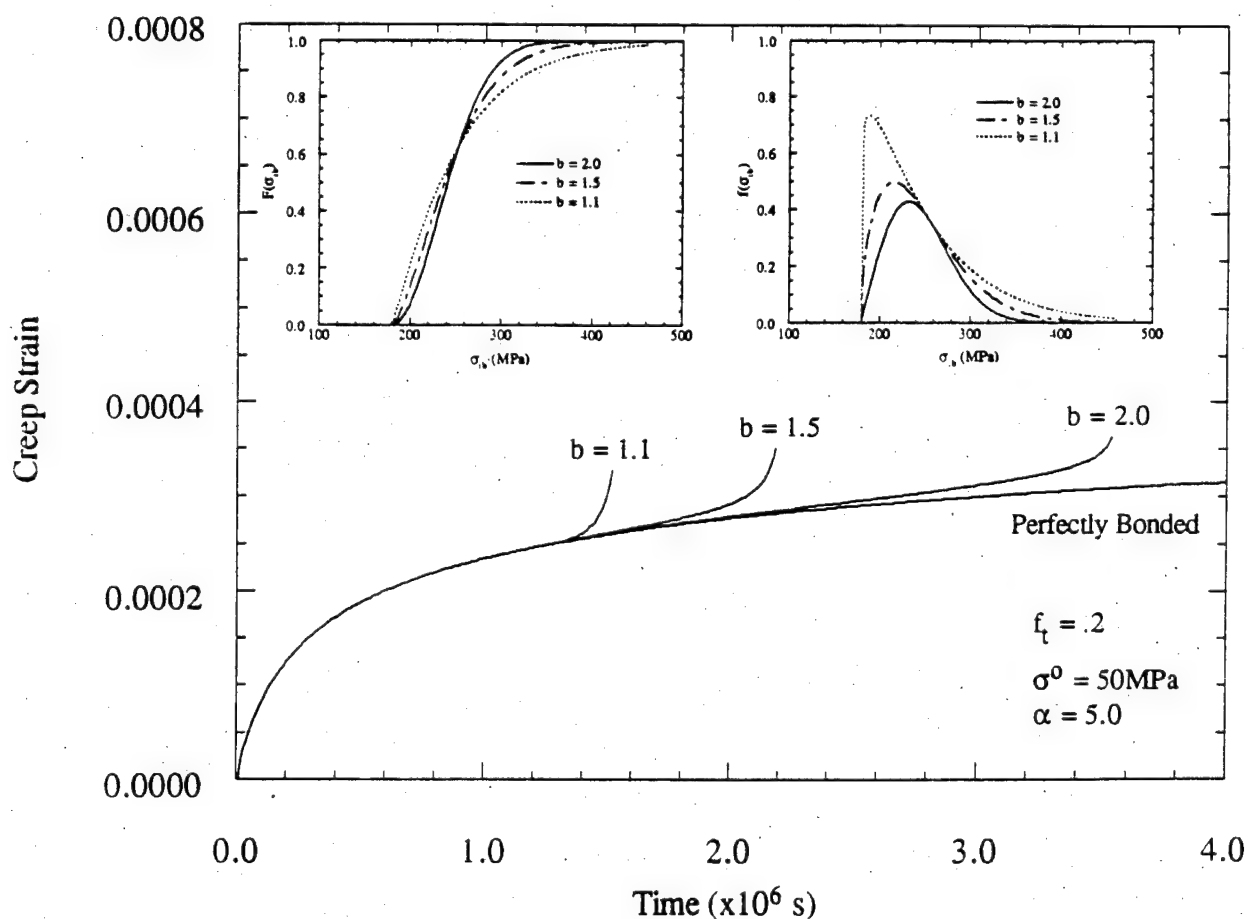


Figure 4.5 Predicted creep strain-time relation of a SiC whisker/6061 Al matrix composite for various values of shape parameter of Weibull function Eq. (4.16).

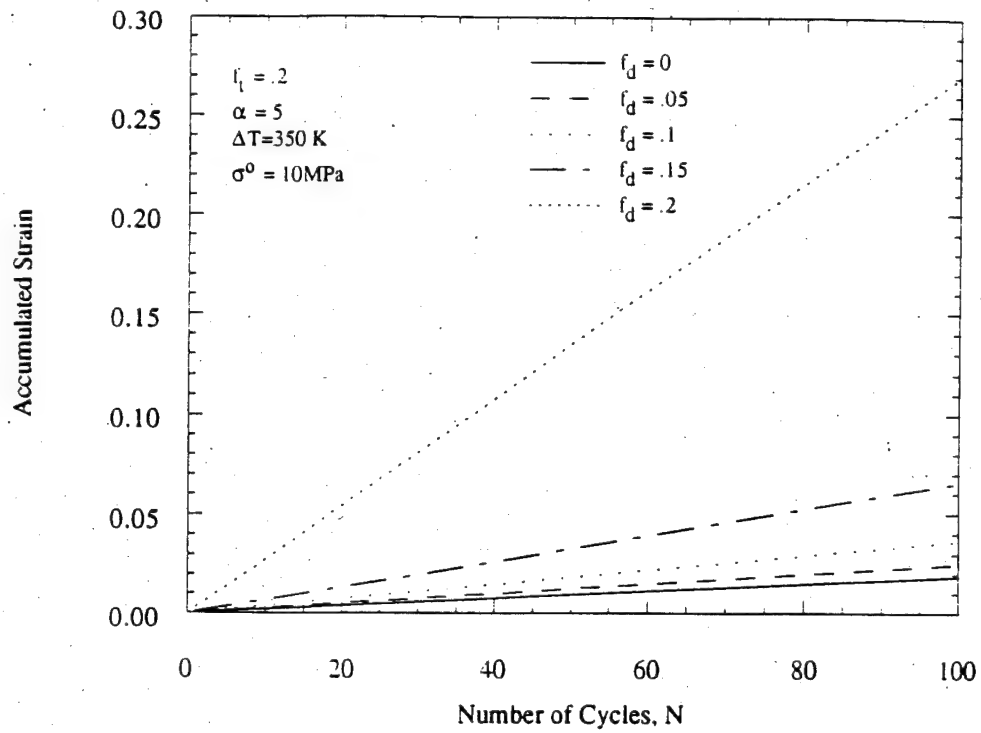


Figure 4.6 Predicted accumulated strain-thermal cycles relation of a SiC whisker/6061 Al matrix composite subjected to combined creep and thermal cycling.

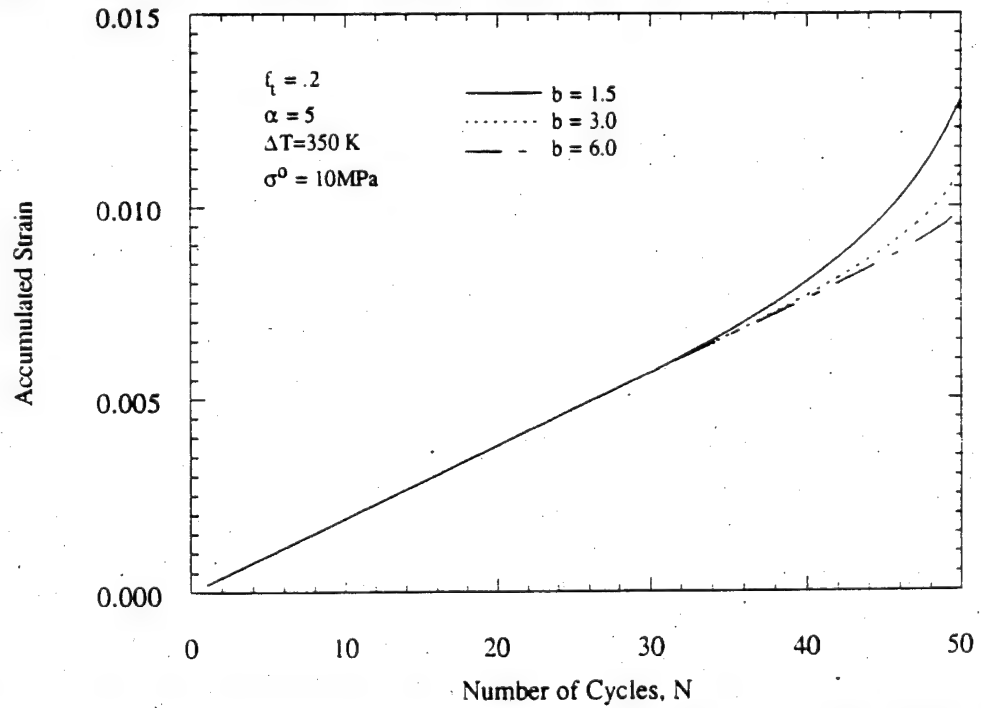


Figure 4.7 Predicted accumulated strain-thermal cycles relation of a SiC whisker/6061 Al matrix composite subjected to combined creep and thermal cycling for various values of shape parameter b .

various values of the shape parameter, b , at a guaranteed $\epsilon_{cr} = .01$. The effect of b is to broaden the distribution (as b increases) so that the development of damage after ϵ_{cr} is less abrupt as is evident in Fig. 4.7. Although the example shown in Fig. 4.7 is primarily an illustration of the capabilities of the proposed model, it is evident that the experimentally observed phenomena of increasing nonlinear strain accumulation with progressive damage can be described with this model. Efforts to correlate the interfacial damage with observed strain accumulation are currently underway.

4.1.4 References

1. M. Taya, 1991, "Creep Behavior of Metal Matrix Composites," in *Metal Matrix Composites: Mechanisms and Properties*, eds by R. K. Everett and R. J. Arsenault, Academic Press, pp. 189-215.
2. Taya, M., and Arsenault, R.J., 1989, *Metal Matrix Composites, Thermomechanical Behavior*, Permagon Press.
3. Zhu, Z. G. and Weng, G. J., 1989, "Creep Deformation of Particle-Strengthened Metal Matrix Composites," *J. Eng. Mat. and Technology*, Vol. 111, pp. 99-105.
4. Zhu, Z. G. and Weng, G. J., 1990a, "Creep Anisotropy of a Metal Matrix Composite Containing Dilute Concentration of Aligned Spheroidal Inclusions," *Mechanics of Materials*, Vol. 9, pp. 93-105.
5. Zhu, Z. G. and Weng, G. J., 1990b, "A Local Theory for the Calculation of Overall Creep Strain of Particle-Reinforced Composite," *International Journal of Plasticity*, Vol. 6, pp. 449-469.
6. Wang, Y. M. and Weng, G. J., 1992, "Transient Creep Strain of a Fiber-Reinforced Metal-Matrix Composite Under Transverse Loading," *J. Eng. Mat. and Technology*, Vol. 114, pp. 237-244.
7. Pan, H. H. and Weng, G. J., 1992, "An Energy Approach to the High-Temperature Creep of Fiber-Reinforced Metal-Matrix Composites," in *Damage Mechanics in Composites*, ASME AMD-Vol. 150/AD-Vol. 32, D. H. Allen and D. C. Lagoudas eds., ASME Winter Annual Meeting, pp. 195-212.
8. Eshelby, J. D., 1957, "The Determination of the Elastic Field of an Ellipsoidal Inclusion, and Related Problems," *Proceedings of the Royal Society of London*, Vol. A241, pp. 376-396.
9. Mori, T., and Tanaka, K., 1973, "Average Stress in Matrix and Average Elastic Energy of Materials With Misfitting Inclusions," *Acta Metallurgica*, Vol. 21, pp. 571-574.

10. Taya, M., and Mori, T., 1987, "Modeling of Dimensional Change in Metal Matrix Composites Subjected to Thermal Cycling," *Thermomechanical Couplings in Solids*, edited by H. D. Bui and Q. S. Nguyen, pp. 147-162.
11. Derby, B., 1991, in *Proc. of the 12th Riso International Symposium on Materials Science: Metal Matrix Composites - Processing, Microstructure, and Properties*, N. Hansen et al., eds., pp. 149-171.
12. Taya, M., Armstrong, W. D., and Dunn, M. L., 1993, "Thermal Cycling Damage of Metal Matrix Composites," *Applied Mechanics Reviews*, in press.
13. Zhang, H., Daehn, G. S., and Wagoner, R. H., 1991, "Simulation of the Plastic Response of Whisker Reinforced Metal Matrix Composites under Thermal Cycling Conditions," *Scripta Metall.*, Vol. 25, pp. 2285-2290.
14. Chen, Y. and Daehn, G. S., 1991, "The Thermal Cycling Deformation of a Particle Reinforced Metal Matrix Composite: Comparison Between a Model and Experimental Observations," *Scripta Metall.*, Vol. 25, 1543-1548.
15. Povirk, G. L., Nutt, S. R., and Needleman, A., 1992, "Analysis of Creep in Thermally Cycled Al/SiC Composites," *Scripta Metall.*, Vol. 26, pp. 461-466.
16. Nieh, T. G., 1984, "Creep Rupture of a Silicon Carbide Reinforced Aluminum Composite," *Metallurgical Transactions A*, Vol. 15A, pp. 139-146.
17. Morimoto, T., Yamaoka, T., Lilholt, H. and Taya, M., 1988, "Second Stage Creep of SiC Whisker/6061 Aluminum Composite at 573K," *J. Eng. Mater. Tech.*, Vol. 110, pp. 70-76.
18. Dragone, T. L., Schlautmann, J. J., and Nix, W. D., 1991, "Processing and Creep Characterization of a Model Metal Matrix Composite: Lead Reinforced with Nickle Fibers," *Metallurgical Transactions A*, Vol. 22A, pp. 1029-1036.
19. Pandey, A. B., Mishra, R. S., and Mahajan, Y. R., 1993, "Creep Fracture in Al-SiC Metal Matrix Composites," *Journal of Materials Science*, Vol. 28, pp. 2943-2949.
20. Echigoya, J., Taya, M., and Armstrong, W. D., 1991, "An Investigation into the Degradation Mode of W-ThO₂/FeCrAlY Metal Matrix Composite Under Thermal Cycling," *Materials Science and Engineering*, Vol. A141, pp. 63-66.
21. Dunn, M. L. and Taya, M., 1992, "Thermal Cycling Creep of Metal Matrix Composites," *Scripta Metallurgica*, Vol. 27, pp. 1349-1354.
22. Mura, T., 1987, *Micromechanics of Defects in Solids*, Second ed., Martinus Nijhoff Publisher.
23. Armstrong, W. D., Taya, M., and Dunn, M. L., 1991, "Strain Accumulation in Thermal Cycled Metal Matrix Composites," in *Damage and Oxidation Protection in High Temperature Composites*, ASME AD-Vol. 25-2, G. K. Haritos and O. O. Ochoa eds., ASME Winter Annual Meeting, pp. 51-66.

24. Tanaka, K., Mori, T., and Nakamura, T., 1970, "Cavity Formation at the Interface of a Spherical Inclusion in a Plastically Deformed Matrix," *Phil. Mag.*, Vol. 21, pp. 267-279.
25. Taya, M., and Chou, T. W., 1981, "On Two Kinds of Ellipsoidal Inhomogeneities in an Infinite Elastic Body: An Application to a Hybrid Composite," *International Journal of Solids and Structures*, Vol. 17, pp. 553-563.
26. Weng, G. J., 1987, "A Micromechanical Theory of High Temperature Creep," *J. Appl. Mech.*, Vol. 54, pp. 822-827.
27. Odqvist, F. K. G., 1974, *Mathematical Theory of Creep and Creep Rupture*; Oxford Press.
28. Takao, Y., and Taya, M., 1985, "Thermal Expansion Coefficients and Thermal Stresses in an Aligned Short Fiber Composite With Application to a Short Carbon Fiber/Aluminum," *Journal of Applied Mechanics*, Vol. 107, pp. 806-810.
29. Yoda, S., Kurihara, N., Wakashima, K. and Umekawa, S., 1978, "Thermal Cycling-Induced Deformation of Fibrous Composites with Particular Reference to the Tungsten-Copper System," *Metal. Trans.*, Vol. 9A, pp. 1229-1236.

4.2. Analytical Model for a Particulate Composite

4.2.1 Introduction

A metal matrix composite (MMC) consists of a matrix metal and reinforcements and its mechanical properties are normally superior to those of the unreinforced metal except for the fracture toughness and the thermal cycling creep resistance. The main reason for this defect of MMC is the mismatch of the coefficient of thermal expansion (CTE) between the matrix metal and reinforcements which is an inevitable characteristic of MMCs [1]. It is well known that the combination of relatively small applied stress and cyclic thermal loading can result in increased creep rates and superplastic deformations in metal matrix composites [2]. Even without an applied stress, a detrimental dimensional change has been observed in a number of thermal cycled metal matrix composite systems [3,4]. These effects are important aspects for study in the assessment of MMCs as candidates for high temperature structural applications requiring dimensional stability. Although a series of experiments on the thermal cycling creep behavior of discontinuous MMCs have been made [2,5-7], the analytical model to predict dimensional change still remains to be made.

For the analysis of the enhanced creep rate under creep/thermal cycle loading, the determination of internal stress is prerequisite. The existence of internal stress has been proved by the use of X-ray and neutron diffraction methods and the measurements of differences between compressive and tensile mechanical properties [8]. High internal stresses generated at the interface between the fiber and matrix are readily relaxed to a lower stress state by a dislocation punching. This phenomenon has been observed in a SiC whisker/Al composite in situ transmission electron microscopy study [9,10].

Hong et al. studied the thermal cycling creep behavior of SiC whisker/2024 Al composite both analytically and experimentally, and computed strain per thermal cycle by using the matrix creep equation of a hyperbolic sine type [5]. The average internal stress in the matrix induced by temperature change was estimated by using equation to fit the thermal cycling data at low stresses for the composite and was considered to be the local yield stress of the matrix. The matrix creep equation was constructed from the isothermal creep data of the composite in the transverse direction instead of unreinforced matrix. Although an applied stress is distributed to both the matrix and fiber, they considered the matrix stress to be the applied stress.

Daehn et al. also studied the thermal cycling creep behavior of SiC whisker/6061 Al composite both analytically and experimentally, whose model predicted strain rate by using the matrix creep equation of power law type [6]. The matrix stress consists of the shear stress from an applied stress and an axial stress from a temperature change and the resultant stress in the matrix

and its direction were computed by using 2-D Mohr circle approach. The elongation of the composite is assumed to result from the formation of voids at the ends of fiber. Although the model composite uses the fiber aspect ratio of 10, the thermal stress in the matrix was computed by using the concept of continuous fiber reinforced MMC and the isostrain assumption. In constructing the power creep law for the matrix, the exponent of power law, n , is selected as 11, which may be too high for the Al matrix.

Pickard and Derby extended the Greenwood et al. model to predict the thermal cycling creep rate of SiC particle/ Al 1100, where the strain per thermal cycle was computed by using the uniform time-independent plastic deformation of the matrix [7]. Greenwood et al. model was originally developed for the study on the phase transformation plasticity of metals at temperatures low compared with the melting temperature of the materials and small applied stress so that the creep of the matrix was neglected [11], which may not reflect the actual situation in the MMC subjected to thermal cycling creep loading at higher temperature than the homologous temperature. When the amplitude of temperature cycling is not large enough, the matrix yielding is localized around the reinforcement so that uniform yielding of the matrix is not physically realistic. The critical temperature change required to initiate such a full plastic flow on cooling and heating was derived using yield criterion, but the interaction effect between particles was not included.

Dunn and Taya constructed a model for the perfectly-bonded and debonded MMCs under the condition of large temperature cycling, where strain per thermal cycle was computed by using the time-independent plastic deformation of the matrix during cooling and heating, and the creep of the matrix during high temperature plateau and debonding at the fiber-matrix interface was used to explain the non-linear strain accumulation of MMCs associated with the later stage of thermal cycling [12]. For the perfectly-bonded interface, their prediction of the strain per thermal cycle becomes zero except the first cycle. If the CTE mismatch strain generated by temperature change is small so that the yielding of the matrix metal is localized around fibers, then the assumption of general yielding of the matrix in the entire matrix domain is not valid. Therefore, the internal stress needs to be estimated based on the localized plastic zone.

The purpose of this work is multi-fold: to observe the dimensional change of a MMC under combined creep and thermal cycling with small temperature change where the localized plastic deformation around particulates is expected to take place, to develop an analytical model to predict the dimensional change and to compare the analytical predictions with the experimental results. In this model, we focus on the combined effects of the internal stress, externally applied stress and the relaxation of the stress induced by creep strain. The temperature-induced internal stress is calculated based on stress-free temperature by using dislocation punching model [13] and the matrix stress carried by externally applied stress is also calculated, where the Eshelby's equivalent inclusion method [14] and Mori-Tanaka's mean field theory [15] are used. Finally, the predictions

will be compared with the experimental results by the use of material properties of each constituent and temperature profile as model inputs.

4.2.2. Analytical model

It is assumed in the present model that prolate particulates (hereafter particulates) are purely elastic and the matrix is elastic-plastic-creeping. The key analysis is the computation of the average stresses carried by the matrix. For the prediction of the dimensional change of a MMC under creep/thermal cycle loading, those stresses are induced due to the three driving sources: (1) temperature change, (2) applied stress and (3) the creep and diffusional relaxation of the matrix. The first is relaxed by dislocation punching, based on which the average matrix stresses are calculated at each temperature for a temperature profile of thermal cycle by using temperature-dependent yield stress. The amount of the second carried by the matrix is a function of material properties and particulate shape and calculated by using Eshelby type model. The last is assumed to be relaxed by a relaxation mechanism such as interfacial diffusion and calculated by Eshelby type model as well. Finally, the strain per cycle is numerically calculated by using the equation of matrix creep, the power law of Dorn type, where the above stresses are used as a driving source.

Matrix stress due to temperature change

Upon cooling by ΔT from a stress-free temperature (T_0) to a lower temperature (T), the CTE mismatch strain will be developed at the particulate-matrix interface and given by $\alpha^* = (\alpha_f - \alpha_m)\Delta T$ where α_f and α_m are the CTEs of the particulate and matrix, respectively and $\Delta T = T - T_0$. These strains are simulated by arrays of prismatic dislocation loops attached to the particulate-matrix interface where a particulate is modeled by a prolate spheroid (Ω_1). These loops are assumed to be punched out symmetrically to reduce the otherwise localized high stress field at the particulate-matrix interface and the punched-out dislocation loops are represented by another prolate spheroid (Ω_2) with e^{2*} ($= \{1 1 1 0 0 0\} \alpha^* / \eta$) where the aspect ratio of Ω_2 is assumed to be the same as Ω_1 . The illustration of the relaxed and non-relaxed states are given in Fig. 4.8.

The computational procedure used here is the same as that of Taya and Mori [16] except for a minor modification, thus only its brief summary is given in Appendix A. The stress fields in the donut-shaped domain of ($\Omega_2 - \Omega_1$) and in the domain of particulate (Ω_1) can be expressed as:

$$\sigma^2 = C_m \cdot (S - I) \cdot \left[(1 - \eta^3 f) e^{2*} - f e^{1**} \right] \text{ in } \Omega_2 - \Omega_1 \quad (4.29)$$

$$\underline{\sigma}^2 + \underline{\sigma}^1 = \mathbf{C}_m \cdot (\mathbf{S} - \mathbf{I}) \cdot \left[(1 - \eta^3 f) \mathbf{e}^{2*} + (1 - f) \mathbf{e}^{1**} \right] \text{ in } \Omega_1 \quad (4.30)$$

where \mathbf{e}^{1**} is the yet unknown fictitious eigenstrain introduced into Ω_1 and is solved as:

$$\mathbf{e}^{1**} = \mathbf{A}^{-1} \cdot (1 - \eta^3 f) \cdot (\mathbf{C}_m - \mathbf{C}_f) \cdot (\mathbf{S} - \mathbf{I}) \cdot \mathbf{e}^{2*} \quad (4.31)$$

where \mathbf{A} is given by Eq. (A-8) in Appendix A.

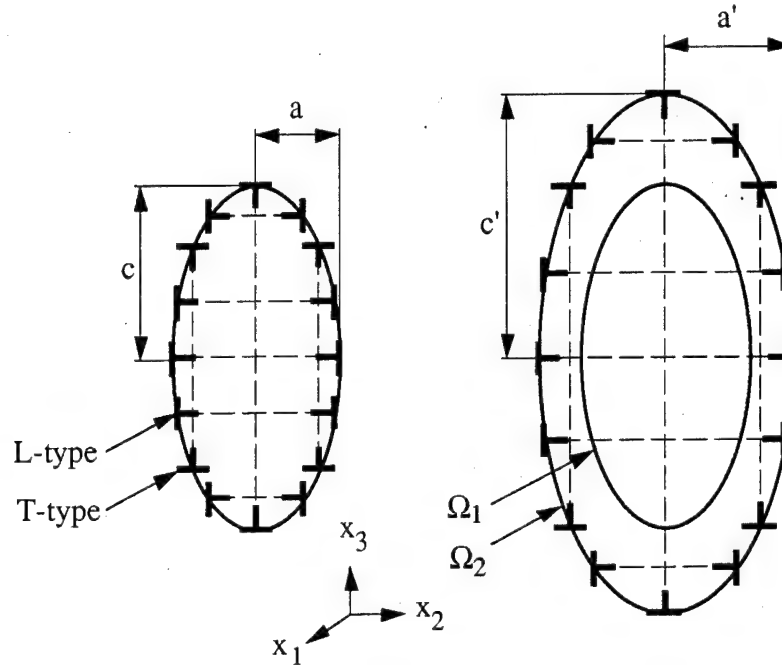


Figure 4.8 Prismatic dislocation loops generated by the mismatch of CTEs between the particulate and matrix and temperature change: (a) before punching and (b) after punching.

The normalized punching distance, η ($=c'/c$), is determined by using both the driving and retarding forces of dislocation motion. The driving force is a result of the decrease in the total potential energy as the loops are punched out and the retarding force is a resultant force opposing both climbing and gliding motions of dislocations. The criterion to determine the punching distance is proposed by Tanaka et al.[17]:

$$\frac{\partial U}{\partial \eta} = - \frac{\partial W}{\partial \eta} \quad (4.32)$$

where U and W denote the total potential energy of the composite and the total work dissipated by the motion of the dislocation loops over the punching distance, respectively. The U and W are calculated from the stress and strain fields in the composite and the geometrical consideration of dislocation movement and expressed as:

$$U = -\frac{1}{2}f \left[\eta^3 \tilde{\sigma}^2 \cdot \tilde{\epsilon}^{2*} + \tilde{\sigma}^1 \cdot \tilde{\epsilon}^{2*} \right] \quad (4.33)$$

$$W = \left[(\beta + 4) + \sqrt{2(1+\beta^2)}(4\beta+1) \right] f(\eta-1)k\alpha^* \quad (4.34)$$

where β and k denote the particulate aspect ratio and the yield stress of the matrix in shear, respectively. The detailed derivation of U and W is given in Appendix B.

By using Eq. (4.30) and the facts that the stress in the particulate is proved to be uniform by Eshelby and the integral of internal stress over the composite domain vanishes, $(1-f)\tilde{\sigma}_m + f\tilde{\sigma}_f = 0$, the average stress in the matrix due to the temperature change, $\tilde{\sigma}_m^T$, is computed as:

$$\tilde{\sigma}_m^T = -\frac{f}{1-f} \left(\tilde{\sigma}^2 + \tilde{\sigma}^1 \right) \quad (4.35)$$

Matrix stress due to applied stress

The stress externally applied to the composite material $\tilde{\sigma}^o$ shown in Fig. 4.9 is shared by the matrix and particulate. The stresses carried by each component are determined by its mechanical properties and particulate shape. By using the Eshelby's equivalent inclusion method, the average stress carried by the matrix under applied stress $\tilde{\sigma}^o$, $\tilde{\sigma}_m^A$, can be calculated as[12]

$$\tilde{\sigma}_m^A = \left[\mathbf{I} + f \mathbf{C}_m \cdot (\mathbf{S} - \mathbf{I}) \cdot \mathbf{A}^{-1} \cdot (\mathbf{C}_f - \mathbf{C}_m) \cdot \mathbf{C}_m^{-1} \right] \cdot \tilde{\sigma}^o \quad (4.36)$$

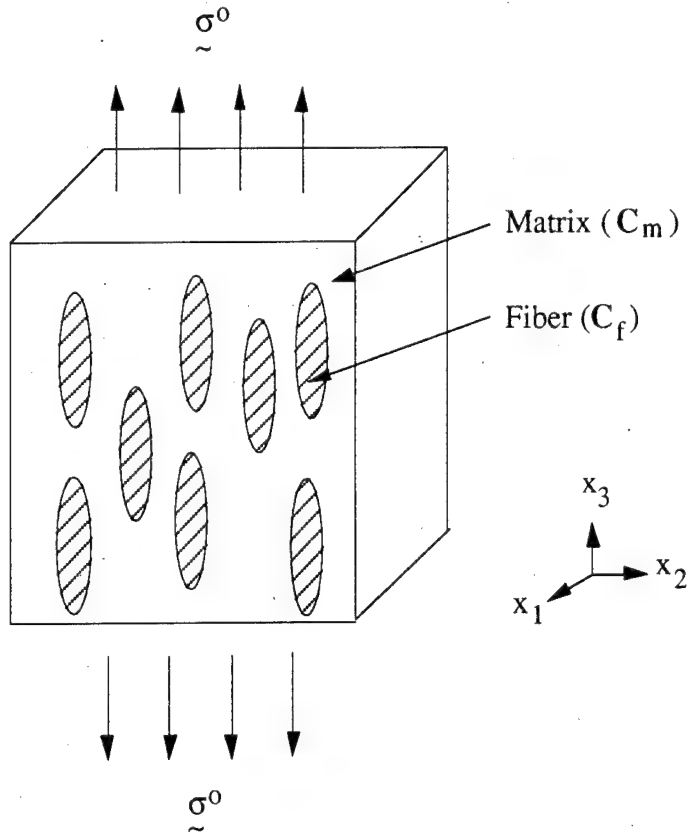


Figure 4.9 Idealized model for SiCp/Al composite with perfectly aligned particulates to compute the matrix stress due to an applied stress $\sigma_{\text{̃}}^0$.

Matrix stress due to matrix creep and interfacial diffusion

As creep strain is accumulated in the matrix domain, the matrix is hardened by the back stress due to geometrically necessary dislocations around particulates resisting against the otherwise homogeneous plastic deformation of the matrix. However, it has been also recognized that the back stress state is not stable and can be relaxed by some mechanisms[18]. It is assumed that interfacial diffusion takes place and relaxes some of the buildup of back stress[19]. Since the stress field in the particulate due to back stress and its diffusional relaxation becomes hydrostatic, it does not affect further plastic deformation of the matrix[20].

The small amount of uniform creep strain in the matrix, $\text{d}\epsilon_m (= \mathbf{B} \text{d}\epsilon_m)$, and its diffusional strain in the particulate, $\text{d}\epsilon_d (= \mathbf{B} \text{d}\epsilon_d)$, induce the stresses in the particulate, $\text{d}\sigma^c (= -(1-f)\mathbf{U} \cdot \text{d}\epsilon_m/f)$ and $\text{d}\sigma^d (= (1-f)\mathbf{U} \cdot \text{d}\epsilon_d/f)$, respectively, where $\mathbf{B} = \{ -1/2, -1/2, 1, 0, 0, 0 \}$ and $\mathbf{U} = f \mathbf{C}_m \cdot (\mathbf{S} - \mathbf{I}) \cdot \mathbf{A}^{-1} \cdot \mathbf{C}_f \cdot \mathbf{B}$. The detailed derivations of these stresses are given in

Appendix C. From the requirement of the diffusional relaxation, the 1- and 3- components of stresses satisfy the following[20]:

$$d\sigma_3^c + d\sigma_3^d = d\sigma_1^c + d\sigma_1^d \quad (4.37)$$

By inserting Eqs. (C-7) and (C-9) into Eq. (4.37), the diffusional strain in the particulate becomes equal in magnitude to the creep strain in the matrix, i.e.,

$$de_m = de_d \quad (4.38)$$

By using the requirement of internal stress in a composite: $(1-f)\sigma_m + f\sigma_f = 0$, the resultant matrix stress $d\sigma_m$ generated by the incremental creep and diffusional strains is calculated and canceled out:

$$d\sigma_m = \mathbf{U} \cdot (de_m - de_d) = 0 \quad (4.39)$$

Strain per thermal cycle

Since the creep resistance of silicon carbide is much higher than that of aluminum due to its high modulus and low diffusion rate, it can be assumed that SiC particulates do not deform plastically while Al matrix does during thermal cycling/creep. The creep rate of a composite depends only on the matrix creep rate which is assumed to obey the power law of Dorn type[21]. From Eqs. (4.35), (4.36) and (4.39), the matrix creep rate is obtained as

$$\dot{e}_m = \frac{A_0}{T} [\sigma_m^T + \sigma_m^A]^n \exp(-\frac{Q}{RT}) \quad (4.40)$$

where A_0 , T , R and Q are Dorn constant, temperature in Kelvin, gas constant and activation energy respectively and matrix stresses and strain are expressed in terms of equivalent quantities based on the Von-Mises yield criterion. Once the matrix creep rate is given, the composite strain rate, \dot{e}_c , is calculated by adding the creep and diffusional strain rates:

$$\dot{e}_c = (1-f)\dot{e}_m + f\dot{e}_d \quad (4.41)$$

By using Eqs. (4.38) and (4.41), we arrive at

$$\dot{e}_c = \dot{e}_m \quad (4.42)$$

Finally, the strain per thermal cycle of the composite can be computed by numerically integrating Eq. (4.40) over one thermal cycle:

$$e_c = \int_0^\tau \dot{e}_m dt \quad (4.43)$$

where τ is duration of one thermal cycle.

4.2.3. Results and discussion

The isothermal creep data of the matrix are required as input data for the analytical model, but only limited creep data are available. Using the creep data at the temperatures of 300 °C, the power law creep equation in the form of Eq. (4.40) is constructed, where Q is the activation energy of pure aluminum for lattice diffusion and is obtained from the literature[21]. The temperature-dependent yield stress of the matrix was measured and the results are shown in Fig. 4.10. The properties and parameters of each constituent material used in the present analysis are summarized in Table 4.1[22,23], where the stress-free temperature is assumed to be the solution-treatment temperature T_0 (=530°C).

Table 4.1 Material properties and parameters of the particulate and matrix used as model inputs.

Properties	Units	Al	SiC
E	GPa	70	427
v	-	0.33	0.17
α	$\times 10^{-6}$	23.6	4.3
f	-	0.8	0.2
A_0	-	1522	
n	-	4.73	
Q	KJ/mole	142	
T_0	°C	530	
β			2.25

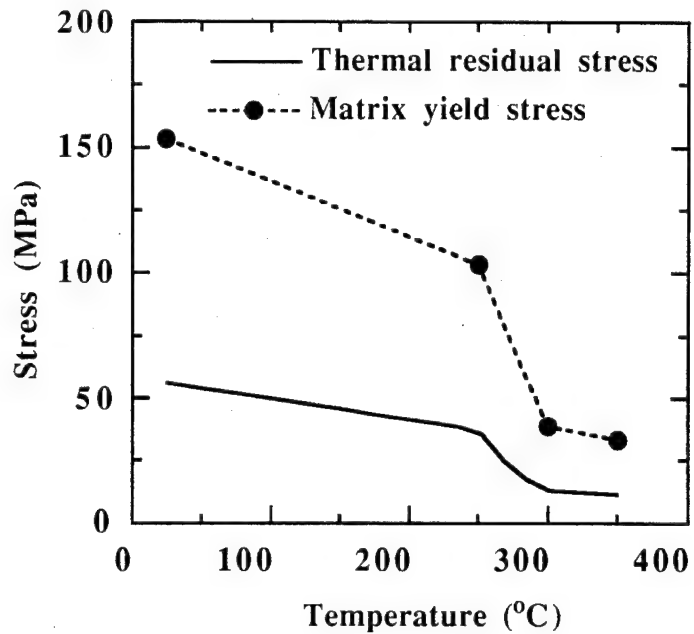


Figure 4.10 The predictions of thermal residual stress in the matrix at each temperature based on the temperature-dependent yield stress of the matrix.

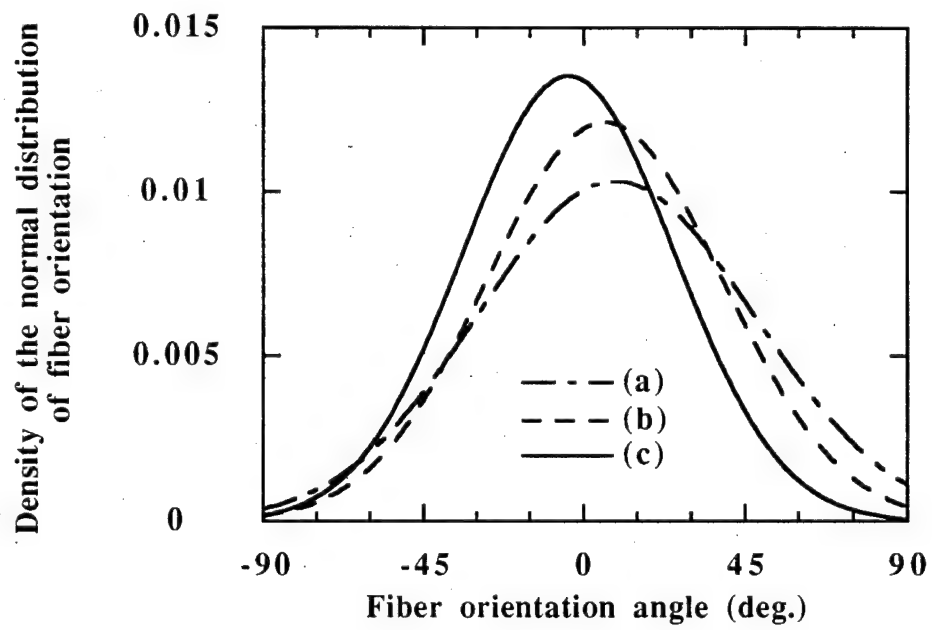


Figure 4.11 Results of microstructural studies on SiC_p/Al composite in terms of the density of the normal distribution of particulate orientation: (a) as-received state, (b) as-tested under the applied stress of $\sigma^0=24$ MPa and $T_{max}=300$ °C and (c) $T_{max}=350$ °C, respectively. Angle 0° means that the particulate major axis coincides with the directions of the extrusion and the applied stress.

Since SiC particulates in the composite are not spherical and are misoriented, the distributions of their aspect ratio and orientation angle are needed to predict dimensional change per cycle. The results of the aspect ratio of SiC particulates and the particulate orientation angle distributions of the as-received composite are shown in Figs. 2.11 (a) and 4.11 (a), respectively. These figures reveal that particulates are mostly oriented in the direction of extrusion and their average aspect ratio is 2.15, where angle 0° denotes the directions of the extrusion and applied stress loading axes. For the simplification of the analysis, we assume that particulates are perfectly aligned in the direction of extrusion. Fig. 2.11 also confirms that the average aspect ratio hardly changes during test. Takao et al. have examined the effect of variable aspect ratios on the stiffness and thermal expansion coefficients of a short fiber composite and concluded that the results predicted by using the average value of aspect ratio are not much different those of using variable aspect ratio unless the distribution of aspect ratio is extraordinarily scattered[24]. Thus, the use of the average aspect ratio of 2.25 in the model calculations is justified. Furthermore, the microstructural change due to the fracture of particulates during testing was examined by using micrographs shown in Fig. 2.10. The micrograph of Fig. 2.10 (c) showed the higher possibility of the fractured particulates than Figs. 2.10 (a) and 2.10 (b), while the micrograph of Fig. 2.10 (b) showed the less possibility of the fractured particulates than Fig. 2.10 (a). It can be concluded from these observations that the fracture of particulates does not take place during the creep thermal cycling, but during the processing of the composite.

The predicted internal stresses in the matrix due to the temperature change are plotted as a function of temperature in Fig. 4.10, which are expressed as the equivalent stresses (σ_e , $\sigma_3-\sigma_1$, based on Von-Mises yield criterion. Comparing them with the yield stress of the matrix shown in Fig. 4.10, it can be concluded that the temperature-induced stress strongly depends on the yield stress of the matrix.

The strains per thermal cycle at various applied stresses observed from the SiC_p/Al composites that were thermal-cycled with two different temperature profiles of $T_{\max}=350\text{ }^\circ\text{C}$ and $300\text{ }^\circ\text{C}$ are plotted in Fig. 4.12. The experimental results show that the strain per thermal cycle is an increasing function of an applied stress for both temperature profiles. Using the input parameters tabulated in Table 4.1, the predictions of the strain per thermal cycle of the composite under combined creep/thermal cycling by the present model are also plotted in Fig. 4.12.

For the creep thermal cycle of $T_{\max}=350\text{ }^\circ\text{C}$, the predicted results agree well with the experimental results. Although there exists a reasonably well agreement between the predictions and experiment, the predictions of the strain per cycle for the creep thermal cycle of $T_{\max}=300\text{ }^\circ\text{C}$ overestimate the experimental results. This discrepancy can be explained as follows. First, it is

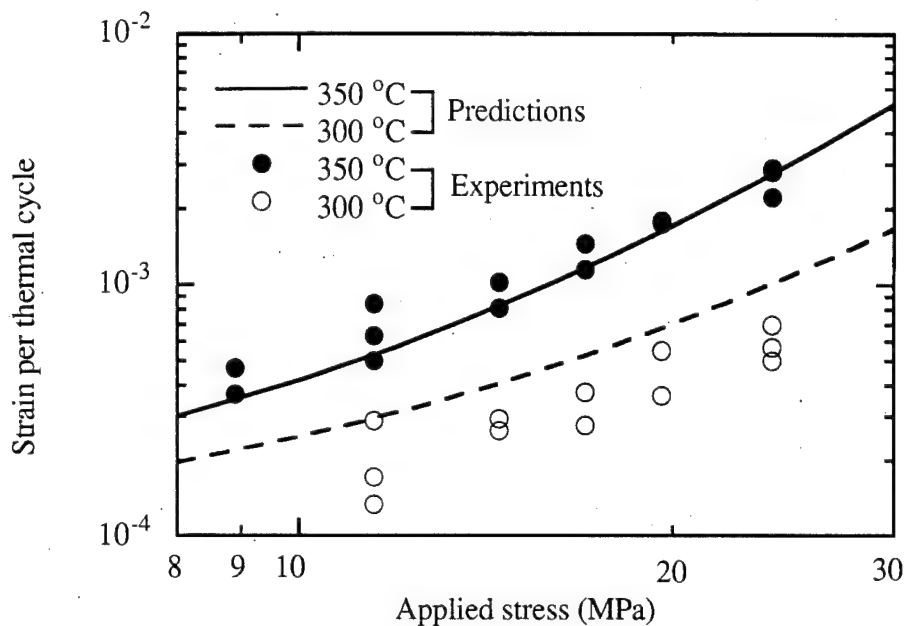


Figure 4.12 Comparison between the analytical and experimental results of strain per thermal cycle of SiC_p/Al composite subjected to temperature cycling and various applied stresses σ^0 : (1) the solid and open circles represent the experimental data for $T_{max}=350$ °C and 300 °C, respectively and (2) the solid and dotted lines denote the analytical results.

assumed that the interfacial diffusion takes place almost instantaneously at each time during thermal cycling. According to the models developed by Mori and his co-workers, the characteristic time of the interfacial diffusion is strongly dependent on the temperature and the calculation of the characteristic times for $T=350$, 300, 250 and 200 °C gives 0.5, 1.5, 5 and 20 seconds, respectively[20,25]. Thus, the recovery of back stress by diffusional relaxation is limited at low temperatures so that the unrelaxed back stress in the matrix lowers the extent of the plastic deformation of the matrix. Secondly, it has been also known that although SiC particulates are randomly distributed in the matrix before test, they are reoriented in the direction of an applied stress during testing[2,26]. This phenomenon was also observed by the microstructural studies on the as-received state and as-tested states, whose results are depicted in terms of the density of the normal distribution of particulate orientation and summarized in Fig. 4.11. The angle of particulate orientation is defined as the angle between the particulate major axis and the applied stress or extrusion direction. The composite with perfectly aligned particulates gives rise to higher dimensional change (strain per cycle) as compared with the composite with misaligned particulates. Because of less particulate reorientation at $T_{max}=300$ °C, the degree of misalignment of SiC particulates in a composite tested at $T_{max}=300$ °C is larger than that at $T_{max}=350$ °C. Therefore, the

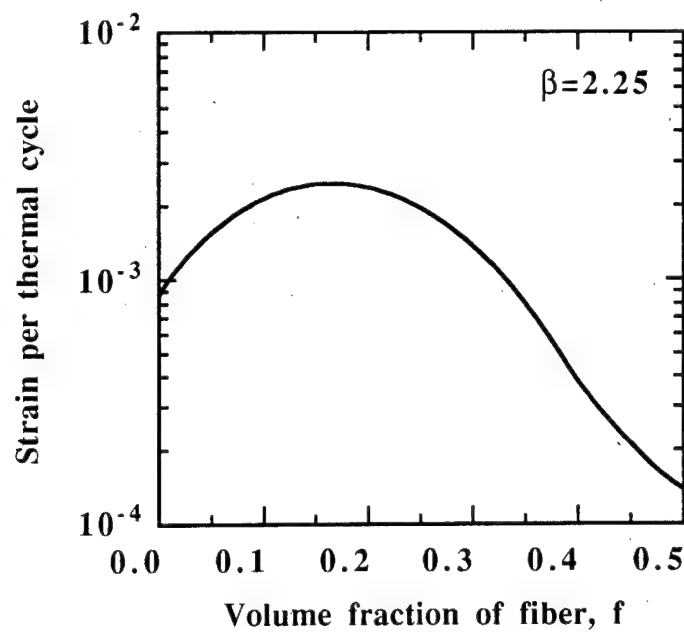


Figure 4.13 The predicted results of the effect of particulate volume fraction f on strain per thermal cycle of SiC_p/Al composite subjected to the temperature cycling of $T_{\max}=350$ $^{\circ}\text{C}$ and the applied stress of $\sigma^0=24$ MPa.

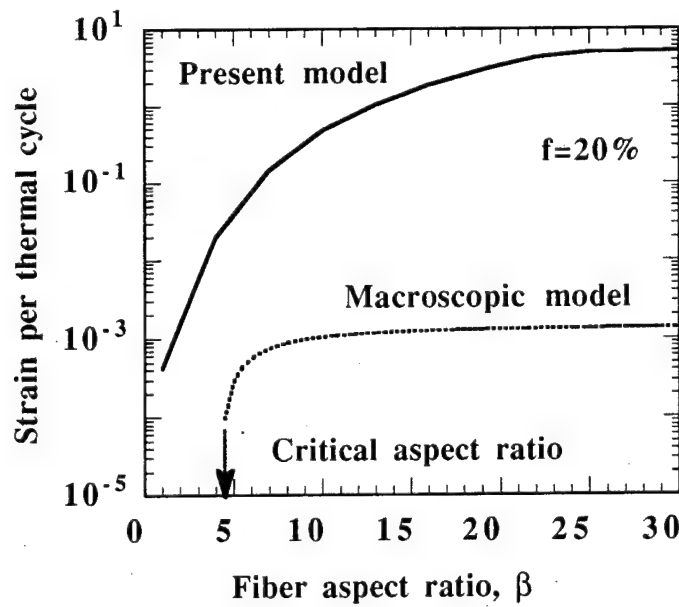


Figure 4.14 The predicted results of the effect of particulate aspect ratio β on strain per thermal cycle of SiC/Al composite subjected to the temperature cycling of $T_{\max}=350$ $^{\circ}\text{C}$ and the applied stress of $\sigma^0=24$ MPa by the present model and macroscopic model^[28].

predictions of strain per thermal cycle for the lower thermal cycle of $T_{max}=300$ °C become higher than the experimental values.

A parametric study is conducted to examine the effects of particulate volume fraction f and particulate aspect ratio for the case of $\sigma^0=24$ MPa and $T_{max}=350$ °C. The results of strain per thermal cycle as a function of f are shown in Fig. 4.13, where the maximum strain per cycle is obtained around $f=0.2$. This agrees with the observations by Pickard et al. where the peak value of strain per cycle takes place between $f=0.2$ and 0.3[7]. The effect of fiber aspect ratio on the strain per thermal cycle of the composite was examined by using two models, the present model and macroscopic model. The macroscopic model is the extension of the model for the pure thermal cycling of MMCs made by Taya and Mori[27] and assumes the idealized temperature profile of step-function type, a plastic deformation of the matrix during cooling and heating and interfacial diffusion during high temperature plateau process. The strain per thermal cycle by the present model results in much higher strain per thermal cycle than the macroscopic model, as fiber aspect ratio increases. This can be explained by the fact that the mode of dislocation punching considered in the present model was the simultaneous punching along both longitudinal and transverse directions, which is considered to be valid only for small particulate aspect ratio. Since the dislocation punching has preferred direction along the fiber major axis as fiber aspect ratio increases[18], the equivalent stress (σ_e) of the matrix induced by temperature change is overestimated by the present model, and the matrix creep rate is strongly dependent on σ_e . While the macroscopic model gives strain per thermal cycle only above the critical fiber aspect ratio (see Fig. 4.14). The assumption of uniform yielding of the matrix during cooling is more compatible with a MMC with larger aspect ratio of fibers. Therefore, *the validity of the present model is restricted to small aspect ratios up to 3*, beyond which the other models such as our previous model[27] should be applied. For the range between 3 and the critical aspect ratio, the present and macroscopic models can not predict the dimensional change accurately. It should be noted here that as f increases, this discrepancy of the predicted dimensional change between the present and the macroscopic models decreases, resulting in more smooth transition.

4.2.4. References

1. M. Taya and R. J. Arsenault, Metal Matrix Composites-Thermomechanical Behavior (Pergamon Press, 1989).
2. M. Y. Wu and O. D. Sherby, "Superplasticity in a Silicon Carbide Whisker Reinforced Aluminum Alloy," Scripta Metall., 18 (1984), 773-776.
3. W. G. Patterson and M. Taya: In: Fifth International Conference on Composite Materials, edited by W. C. Harrigan Jr., J. Strife and A. Dhingra, TMS-AIME, 1985, pp. 53-66.

4. C. M. Warwick and T. W. Clyne: In: *Fundamental Relationships Between Microstructures and Mechanical Properties of Metal Matrix Composites*, edited by M. N. Gungor and P. K. Liaw, TMS, 1989, pp. 209-223.
5. S. H. Hong et al., "Internal Stress Superplasticity in 2024 Al-SiC Whisker Reinforced Composites," *J. Comp. Mat.*, 22 (1988), 102-123.
6. G. S. Daehn, and G. Gonzalez-Doncel, "Deformation of Whisker-Reinforced Metal-Matrix Composites under Changing Temperature Conditions," *Metall. Trans.*, 20A (1989), 2355-2368.
7. S. M. Pickard and B. Derby, "The Deformation of Particle Reinforced Metal Matrix Composites During Temperature Cycling," *Acta Metall.*, 38 (1990), 2537-2552.
8. R. J. Arsenault and M. Taya, "Thermal Residual Stress in Metal Matrix Composite," *Acta Metall.*, 35 (1987), 651-659.
9. M. Vogelsang, R. J. Arsenault and R. M. Fisher, "An In Situ HVEM Study of Dislocation Generation at Al/SiC Interfaces in Metal Matrix Composites," *Metall. Trans.*, 17A (1986), 379-389.
10. R. J. Arsenault and N. Shi, "Dislocation Generation due to Differences between the Coefficients of Thermal Expansion," *Mat. Sci. and Eng.*, 81 (1986), 175-187.
11. G. W. Greenwood and R. H. Johnson, "The Deformation of Metals Under Small Stresses During Phase Transformation," *Proc. of the Royal Soc. of London*, A283 (1964), 403-422.
12. M. L. Dunn and M. Taya, "Modeling of thermal cycling creep damage of short fiber metal matrix composites," *Mat. Sci. and Eng.*, A176 (1994), 349-355.
13. M. Taya, J. K. Lee and T. Mori, To be published.
14. J. D. Eshelby, "The Determination of the Elastic Field of an Ellipsoidal Inclusion, and Related Problems," *Proc. of the Royal Soc. of London*, A241 (1957), 376-396.
15. T. Mori and K. Tanaka, 1973, "Average Stress in Matrix and Average Elastic Energy of Materials with Misfitting Inclusions," *Acta Metall.*, 21 (1973), 571-574.
16. M. Taya and T. Mori, "Dislocations Punched-out Around a Short Fiber in a Short Fiber Metal Matrix Composite Subjected to Uniform Temperature Change," *Acta Metall.*, 35 (1987), 155-162.
17. K. Tanaka, K. Narita and T. Mori, 1972, "Work Hardening of Materials with Strong Inclusions After Prismatic Punching," *Acta Metall.*, 20 (1972), 297-304.
18. C. T. Kim, J. K. Lee and M. R. Plichta, "Plastic Relaxation of Thermoelastic Stress in Aluminum/Ceramic Composites," *Metall. Trans.*, 21A (1990), 673-682.
19. K. Wakashima, B. H. Choi and T. Mori, "Plastic Incompatibility and its Accommodation by Diffusional Flow: Modeling of Steady State Creep of a Metal Matrix Composite," *Materials Sci. and Eng.*, A127 (1990), 57-64.

20. T. Mori, M. Okabe and T. Mura, "Diffusional Relaxation Around a Second Phase Particle," Acta Metall., 28 (1980), 319-325.
21. H. J. Frost and M. F. Ashby, Deformation-Mechanism maps (Pergamon Press, 1982).
22. D. J. Lloyd: In High Performance Composite: Commonality of Phenomena, edited by K. K. Chawla, P. K. Liaw and S. G. Fishman, The Minerals, Metals and Materials Society, 1994, pp. 465-473.
23. R. J. Arsenault and M. Taya, "Thermal Residual Stress in Metal Matrix Composite," Acta Metall., 35 (1987), 651-659.
24. Y. Takao and M. Taya, "The Effect of Variable Fiber Aspect Ratio on the Stiffness and Thermal Expansion Coefficients of a Short Fiber Composite," J. Comp. Mat., 21 (1987), 140-156.
25. E. Sato and K. Kuribayashi, "A Model of Internal Stress Superplasticity based on Continuum Micromechanics," Acta Metall., 41 (1993), 1759-1767.
26. Y. C. Chen, G. S. Daehn and R. H. Wagoner, "The Potential for Forming Metal Matrix Composite Components via Thermal Cycling," Scripta Metall., 24 (1990), pp. 2157-2162.
27. M. Taya and T. Mori, "Modeling of Dimensional Change in Metal Matrix Composite Subjected to Thermal Cycling," Thermomechanical Couplings in Solids (1987), 147-162.
28. R. Weertman and J. R. Weertman, Elementary Dislocation Theory, (Oxford University Press, 1992).
29. M. F. Ashby, "The Deformation of Plastically Non-homogeneous Materials," Phil. Mag., 21 (1970), 399-424.

Appendix A: stress fields in Ω_1 and $\Omega_2 - \Omega_1$

The composite domain is divided into three regions: (1) the matrix domain without dislocations ($D - \Omega_2$); (2) the punched-out domain (Ω_2); and (3) fiber domain (Ω_1), Fig. 4.8. With equation (3), the problem is changed to that of an inhomogeneous inclusion Ω_1 with C_f and \mathbf{e}^{2*} surrounded by a matrix with C_m and \mathbf{e}^{2*} which in turn is embedded in an infinite matrix domain. First apply Eshelby's equivalent inclusion method to a hypothetical composite which contains the punched-out domains (Ω_2) with uniformly distributed eigenstrain \mathbf{e}^{2*} (i.e., fibers are replaced by a material having matrix elastic constants). Then the resulting internal stress, σ_2^2 , in Ω_2 is given by

$$\sigma_2^2 = C_m \cdot (\bar{\mathbf{e}} + \mathbf{e}^{2*} - \mathbf{e}^{2*}) \quad (A-1)$$

where

$$\mathbf{e}^{2*} = \mathbf{S}^2 \cdot \mathbf{e}^{2*} \quad (A-2)$$

where \mathbf{e}^2 and \mathbf{S}^2 are the internal strain caused by inclusion Ω_2 and Eshelby's tensor related to Ω_2 and superscript 2 denotes the quantity related to Ω_2 .

Next introduce fiber (Ω_1) into the inside of Ω_2 . The stress field in the fiber domain caused by this introduction, $\tilde{\sigma}^2 + \tilde{\sigma}^1$, is given by Eshelby's equivalent inclusion method:

$$\begin{aligned}\tilde{\sigma}^2 + \tilde{\sigma}^1 &= \mathbf{C}_f \cdot (\bar{\mathbf{e}} + \mathbf{e}^2 - \mathbf{e}^{2*} + \mathbf{e}^1) \\ &= \mathbf{C}_m \cdot (\bar{\mathbf{e}} + \mathbf{e}^2 - \mathbf{e}^{2*} + \mathbf{e}^1 - \mathbf{e}^{1**})\end{aligned}\quad (\text{A-3})$$

where \mathbf{C}_f and \mathbf{C}_m are the stiffness tensor of the short fiber and the matrix, respectively. Since \mathbf{e}^1 is the disturbance strain due to the introduction of Ω_1 into Ω_2 , it is related to the fictitious eigenstrain (\mathbf{e}^{1**}) in Ω_1 :

$$\mathbf{e}^1 = \mathbf{S}^1 \cdot \mathbf{e}^{1**} \quad (\text{A-4})$$

where \mathbf{S}^1 is Eshelby's tensor of Ω_1 .

Since $\tilde{\sigma}^1$ and $\tilde{\sigma}^2$ are internally induced in the composite, the volume average of the internal stress over the entire composite domain must vanish:

$$\int_D (\tilde{\sigma}^1 + \tilde{\sigma}^2) dV = \mathbf{0} \quad (\text{A-5})$$

From this requirement with Eqs. (A-1~4), $\bar{\mathbf{e}}$ can be expressed as:

$$\bar{\mathbf{e}} = -f_2 (\mathbf{S}^2 - \mathbf{I}) \cdot \mathbf{e}^{2*} - f (\mathbf{S}^1 - \mathbf{I}) \cdot \mathbf{e}^{1**}. \quad (\text{A-6})$$

Here, f and f_2 denote the volume fractions of fibers and the punched-out domains, respectively and are related as $f_2 = \eta^3 f$. \mathbf{S}^2 denote Eshelby's tensor of Ω_2 and is equal to $\mathbf{S} = \mathbf{S}^1$. From Eqs. (A-1~6), the unknown \mathbf{e}^{1**} can be solved as

$$\mathbf{e}^{1**} = \mathbf{A}^{-1} \cdot (1 - f_2) (\mathbf{C}_m - \mathbf{C}_f) \cdot (\mathbf{S}^2 - \mathbf{I}) \cdot \mathbf{e}^{2*} \quad (\text{A-7})$$

where

$$\mathbf{A} = \{(\mathbf{C}_f - \mathbf{C}_m) \cdot [(1 - f) \mathbf{S}^1 + f \mathbf{I}] + \mathbf{C}_m\} \quad (\text{A-8})$$

By inserting Eqs. (A-2), (A-4) and (A-7) into Eqs. (A-1) and (A-3), the stresses in each domain result in the followings:

$$\tilde{\sigma}^2 = C_m \cdot (S - I) \cdot [(1 - \eta^3 f) e^{2*} - f e^{1**}] \text{ in } \Omega_2 - \Omega_1 \quad (A-9)$$

$$\tilde{\sigma}^2 + \tilde{\sigma}^1 = C_m \cdot (S - I) \cdot [(1 - \eta^3 f) e^{2*} + (1 - f) e^{1**}] \text{ in } \Omega_1 \quad (A-10)$$

Appendix B: work dissipated by the motion of dislocation loops

In order to estimate the dissipated energy during the motion of dislocation loops, we decompose the dislocation loops into two groups. The first, designated by L, is to relax the misfit strain in longitudinal direction; and the other, designated by T, is to relax the misfit strain in transverse direction. The dissipated energy due to the dislocation punching of the L-type dislocation loops will be derived in detail.

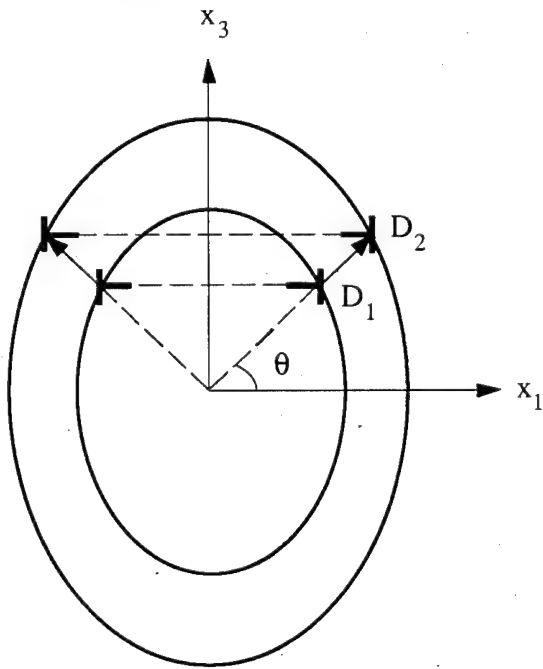


Figure B: A schematic figure depicts that a dislocation loop D_1 is punched out to a dislocation loop D_2 mathematically.

The dislocation punching considered in Figure B is based on the geometrical observation that the dislocation located at D_1 is punched out to D_2 . In reality, the dislocation punching takes place by

the combination of gliding and climbing motions, among which dislocation climb usually occurs at high temperatures, typically above half the melting temperature of the matrix[28]. Since the frictional stresses for gliding and climbing motions of dislocations are defined by k and $2k$ respectively, the resultant friction stress along the θ direction for L-type dislocation loops, σ_{θ}^L , can be expressed as

$$\sigma_{\theta}^L = k(2\cos\theta + \sin\theta) \quad (B-1)$$

where k is the yield stress of the matrix material in shear deformation and $\tan\theta = \frac{\beta\xi}{\sqrt{1-\xi^2}}$. The number of dislocation loops generated at the fiber-matrix interface, N_L , can be obtained using the relationship proposed by Ashby[29], $NAb = \Delta V$, and is given by $N_L = 2c\alpha^*/b$, where N , A , ΔV and b denote the number and area of dislocation loops, the volume change due to the CTE mismatch and the magnitude of the Burgers vector of the matrix, respectively. In addition, the distance, D_L , over which the dislocation located at D_1 moves to D_2 and the length of the prismatic dislocation loop, L_L , are expressed as:

$$D_L = (\eta-1) a \sqrt{\xi^2 + \beta^2(1-\xi^2)} \quad (B-2)$$

$$L_L = 2\pi a \sqrt{1-\xi^2} \quad (B-3)$$

where $\xi = x_3/c$ and β denotes the aspect ratio of fiber. Once the number of dislocation loops, the resultant friction stress, the distance moved and the length of dislocation are known, the dissipated work per the unit volume of the composite for the L-type dislocation loops, W_L , can be expressed as

$$W_L = f(\beta+4)(\eta-1)k\alpha^* \quad (B-4)$$

Using the same method used in the calculation of the dissipated work due to the punching process along the longitudinal direction, the dissipated work per unit volume of the composite, W_T , due to the transverse punching process can be calculated as:

$$W_T = \sqrt{2} f \sqrt{1+\beta^{-2}} (4\beta+1)(\eta-1)k\alpha^* \quad (B-5)$$

Therefore, the total dissipated work due to both longitudinal and transverse punching processes is the sum of Eqs. (B-4) and (B-5) and is equal to:

$$W = \left[(\beta + 4) + \sqrt{2(1+\beta^{-2})} (4\beta + 1) \right] f(\eta - 1) k \alpha^* \quad (B-6)$$

Appendix C: fiber stress due to the creep and diffusional strains

The small amount of uniform creep strain in the matrix, de_m , and its diffusional strain in the fiber, de_d , can be represented by using the assumption of incompressibility and axis-symmetry of deformation mode:

$$de_m = B de_m \quad (C-1)$$

$$de_d = B de_d \quad (C-2)$$

where $B = \{-1/2, -1/2, 1, 0, 0, 0\}$. By applying the Eshelby's equivalent inclusion method to a composite whose matrix has de_m , the stress in the fiber, $d\sigma^c$, due to the creep strain, de_m , can be expressed as:

$$\begin{aligned} d\sigma^c &= C_f \cdot (\bar{e} + e + de_m) \\ &= C_m \cdot (\bar{e} + e - e^*) \end{aligned} \quad (C-3)$$

where the disturbed strain e is related to the unknown eigenstrain e^* defined only in the fiber by

$$e = S \cdot e^* \quad (C-4)$$

Requirement of the integration of the internal stress over the entire composite domain being zero leads to

$$\bar{e} + f(e - e^*) = 0 \quad (C-5)$$

Eliminating \bar{e} and e from Eq. (C-3) by using Eqs. (C-4) and (C-5), e^* is given by

$$e^* = -A^{-1} \cdot C_f \cdot de_m \quad (C-6)$$

where \mathbf{A} is given by Eq. (A-8).

By inserting Eqs. (C-4~6) into Eq. (C-3), the stress in the fiber due to the creep strain can be expressed as

$$d\sigma_c = -\frac{1-f}{f} \mathbf{U} \cdot d\mathbf{e}_m \quad (C-7)$$

where

$$\mathbf{U} = f \mathbf{C}_m \cdot (\mathbf{S} - \mathbf{I}) \cdot \mathbf{A}^{-1} \cdot \mathbf{C}_f \cdot \mathbf{B} \quad (C-8)$$

By replacing $d\mathbf{e}_m$ with $-d\mathbf{e}_d$ in Eq. (C-7), the stress in the fiber due to the diffusional strain, $d\mathbf{e}_d$, can be obtained as:

$$d\sigma_d = \frac{1-f}{f} \mathbf{U} \cdot d\mathbf{e}_d \quad (C-9)$$

5. Analytical Study III: Stress Relaxation by Plastic Flow, Interfacial Sliding, and Diffusion in an Inclusion Bearing Material

5.1 Introduction

Many problems in materials science and mechanics are concerned with the relaxation of stresses, externally imposed or internally produced. Relaxation is a phenomenon of decreasing total energies by the occurrence of inelastic deformation, and the state of a minimum energy is called the complete relaxation. This subject was studied for several cases in terms of elastic states and kinetics in the past, interfacial or boundary sliding [1, 2], interfacial diffusion on the interface of or bulk diffusion around an inclusion (second phase particle) [3-8], and local plastic flow such as dislocation punching [9]. Interfacial diffusion was also used to study creep of a composite [10, 11].

The present paper discusses general conditions of elastic states after the complete relaxation caused by plastic flow, diffusion, and interfacial sliding or the combination of the latter two. The analysis is based on variational methods, with which the elastic state after the complete relaxation can be clearly perceived. Each mode of the above mentioned deformation of plastic character requires a certain physical condition. It is a subsidiary condition imposed on finding the minimum state of energy. Examining subsidiary conditions, one can see whether a mode is more effective in the relaxation than another. Some examples will be given to a specific mode of the relaxation.

5.2. Elastic State After Complete Relaxation

Let σ_{ij}^A be the stress present before the occurrence of stress relaxation. For simplicity, we consider that σ_{ij}^A is caused by an external traction on the boundary of a body D. However, σ_{ij}^A can be an internal stress.

5.2.1 Plastic flow

Suppose that plastic strain ε_{ij}^* is introduced in a domain Ω to relax σ_{ij}^A . Let u_i and σ_{ij} be the displacement and stress caused by ε_{ij}^* , respectively. The total potential energy change, F , due to ε_{ij}^* is written as

$$F\left[\underline{\epsilon}^*\right] = \frac{1}{2} \int_D \sigma_{ij}(u_{i,j} - \epsilon_{ij}^*) dv - \int_{\Omega} \sigma_{ij}^A \epsilon_{ij}^* dv, \quad (5.1)$$

after applying Colonetti's theorem. The first term in Eq. (5.1) is the elastic energy induced by ϵ_{ij}^* and the second term is the change in the potential energy of the external traction induced by ϵ_{ij}^* . If σ_{ij}^A is an internal stress, the second term is the interaction elastic energy between σ_{ij}^A and ϵ_{ij}^* . Since ϵ_{ij}^* is of plastic character, we have the condition

$$\epsilon_{ii}^* = 0 \quad \text{in } \Omega. \quad (5.2)$$

The minimum of Eq. (5.1) under the condition Eq. (5.2) is found by minimizing

$$G\left[\underline{\epsilon}^*\right] = \frac{1}{2} \int_D \sigma_{ij}(u_{i,j} - \epsilon_{ij}^*) dv - \int_{\Omega} \sigma_{ij}^A \epsilon_{ij}^* dv + \int_{\Omega} \lambda(x) \epsilon_{ii}^* dv \quad (5.3)$$

where $\lambda(x)$ is the Lagrange multiplier. The variation of Eq. (5.3) with respect to ϵ_{ij}^* is calculated as

$$\delta G\left[\underline{\epsilon}^*\right] = \int_{\Omega} (\sigma_{ij} + \sigma_{ij}^A - \lambda \delta_{ij}) \delta \epsilon_{ij}^* dv \quad (5.4)$$

Here, δ_{ij} is the Kronecker delta. Since $\delta \epsilon_{ij}^*$ is now arbitrary after λ has been introduced, G or F is minimized or equivalently the complete relaxation occurs when the total stress, $\sigma_{ij} + \sigma_{ij}^A$, becomes

$$\sigma_{ij} + \sigma_{ij}^A = \lambda \delta_{ij} \quad \text{in } \Omega. \quad (5.5)$$

Further, the equilibrium condition leads to

$$\lambda = \text{const.} \quad (5.6)$$

That is, the complete relaxation is attained when the total stress in a domain undergoing plastic deformation becomes uniformly hydrostatic, as schematically shown in Fig. 5.1 (a). This holds

irrespective of the shape and elastic constant of the domain Ω .

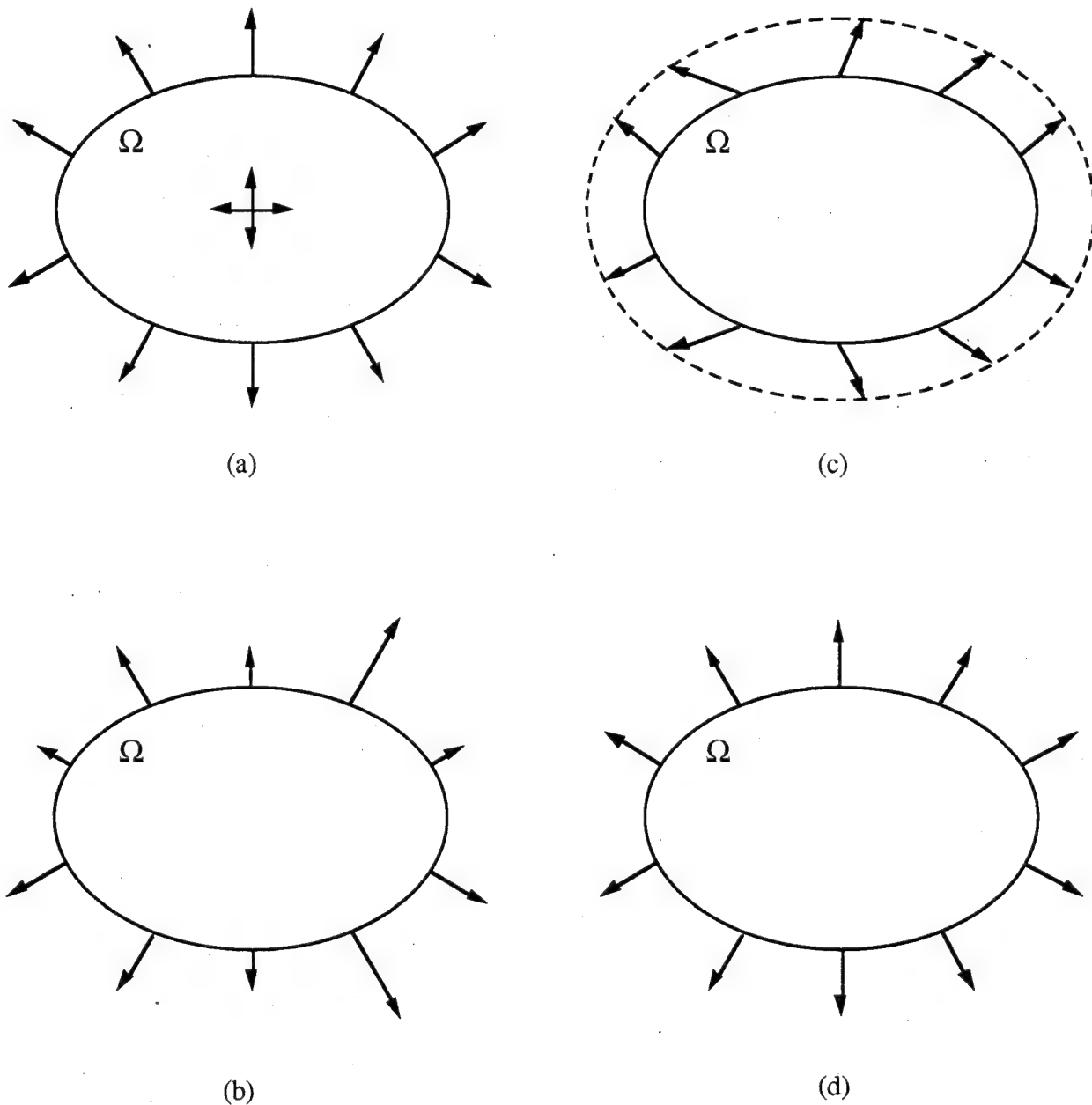


Figure 5.1. The elastic state in an inclusion Ω and the interfacial traction after the complete relaxation due to (1) plastic deformation in Ω , (b) sliding on the interface $|\Omega|$, (c) diffusion on $|\Omega|$ and the combined process of sliding and diffusion $|\Omega|$.

If Ω is an ensemble of unconnected subdomains, $\Omega_1, \Omega_2, \dots, \Omega_N$, the uniform hydrostatic stress changes, in general, from subdomain to subdomain. In particular, if a part of the surface of a subdomain is on a normal traction free surface of the body D , the stress in the subdomain vanishes after the complete relaxation.

We can exchange the role of inclusions with that of their surrounding matrix. If only the matrix deforms plastically, the equilibrium state is achieved when the total stresses in the matrix become uniform and hydrostatic. As will be discussed later, a practical subject covered by this case is creep in a composite or dispersion hardened alloy. Reinforcements in these materials are plastically strong.

Here, we will concentrate our discussion on a metal matrix composite. A composite under a constant external stress stops creep eventually, as the matrix approaches a uniform hydrostatic state with an increase in plastic (creep) strain in it. (Of course, this holds as long as other relaxation mechanisms, such as those to be discussed later, do not operate.) Exactly speaking, a creep rate approaches zero after a sufficient time of creep. Using the average field theory [12], this conclusion has been shown to be correct [13].

Also, we will show a result of two-dimensional FEM analysis to further substantiate this conclusion. An element, as shown in Fig. 5.2, contains a quarter of a cylindrical inclusion surrounded by a creeping matrix. Young's modulus of the cylinder is 2×10^5 MPa and its Poisson ratio 0.33. The matrix creep rate was assumed to be proportional to the cube of a tensile stress under a uniaxial loading condition. A constant load, corresponding to the average external tensile stress of 50 MPa, was applied along the vertical direction (X_3 -axis). The X_1 -axis was parallel to the horizontal direction. The origin of the coordinate system was in the center of the inclusion. The following boundary conditions were used: $u_1=0$ on $X_1=0$ and $u_3=0$ on $X_3=0$. For the other boundaries, the periodic boundary condition was imposed, by tying the nodes, i.e., keeping the total resultant force on the X_1 -surface (boundary perpendicular to the X_1 -axis) zero and the displacement some constant value. The actual FEM calculation was carried out, using the software, MARC, Version 6. We found that as time passed, the creep rate monotonically decreased. We believe that it must have approached zero, if a sufficiently long computing time had been allowed. At this stage, the von Mises stress became almost uniform and negligibly small in the creeping matrix, as shown in Fig. 5.2. Because of the creep law, proportional to the cube of the stress, further creep deformation became extremely slow in the stage corresponding to Fig. 5.2. The details of this study will be reported in a separate paper.

Contrary to the above conclusion, the FEM studies of Dragon and Nix [11] and Kim and McMeeking [14] on creep of a composite ascertained the existence of a stationary state. This is very puzzling in the light of the above theoretical analysis, which has also been numerically confirmed by our own FEM analysis. This is not due to the difference in the creep law, as can be

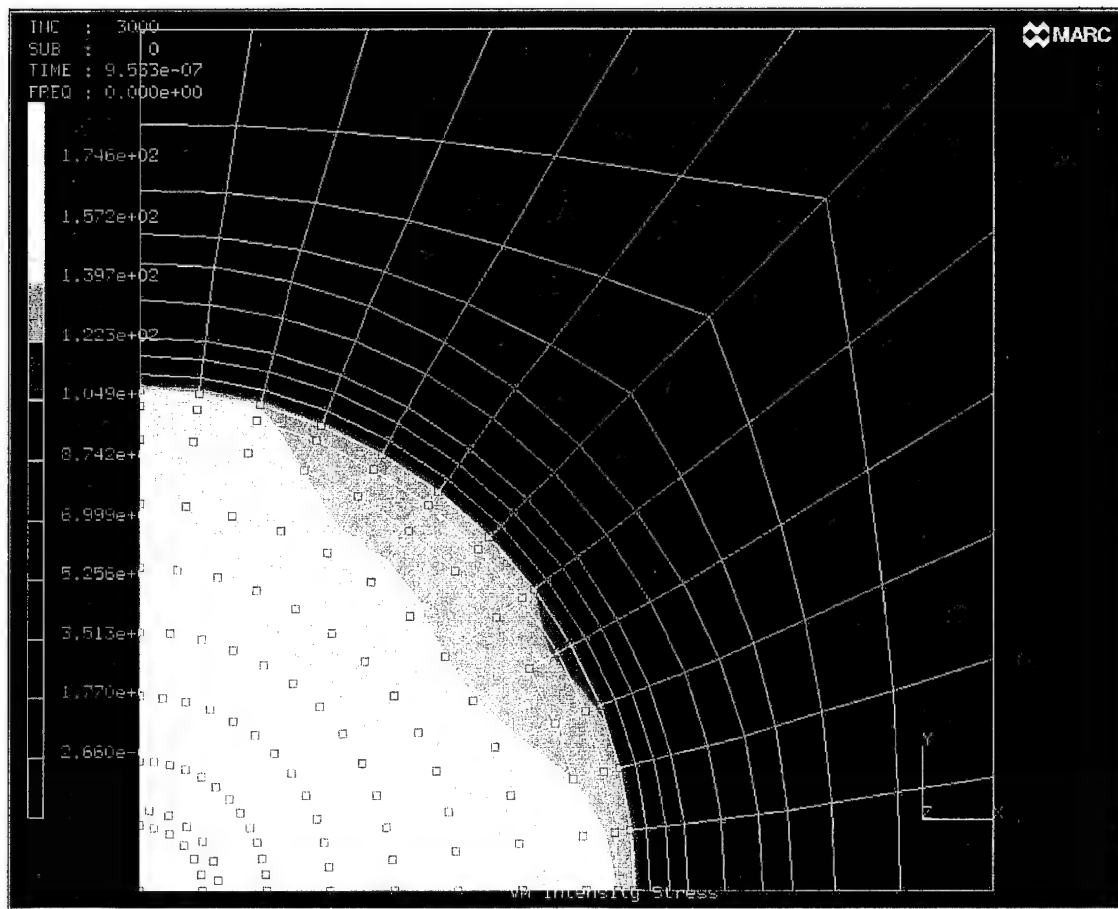


Figure 5.2. Two-dimensional FEM analysis. An elastic cylindrical inclusion is surrounded by a creeping matrix. The figure shows the map of the von Mises stress distribution when a creep rate becomes negligibly small after a sufficient creep time.

seen in Ref [14], but probably due to different boundary conditions. Kim and McMeeking used the boundary conditions: $u_3=0$, $\sigma_{13}=0$ on $X_3=0$, $u_1=0$, $\sigma_{13}=0$ on $X_3=0$ and $\sigma_{13}=0$ on the other boundaries. Dragon and Nix employed the conditions $u_1=0$, $\sigma_{12}=0$ on $X_1=0$, $u_2=0$, $\sigma_{12}=0$ on $X_2=0$, $u_{2,1}=0$, $\sigma_{12}=0$ on the other boundary normal to the fiber axis and $u_{1,2}=0$, $\sigma_{12}=0$ on the boundary parallel to the fiber axis. The adequacy of these boundary conditions should be reexamined.

Approximate analytical modeling of creep of a short fiber composite also led to stationary creep [15]. The following discussion shows that this result is incorrect. A composite or dispersion strengthened alloy shows larger work hardening than a single phase material. Analysis based on continuum mechanics or dislocation theory explains the larger work hardening [16,17]. At the same time, a hardening rate is shown to be independent of yield strength σ_y as long as the amount of plastic strain is small. This is valid in the extreme case of $\sigma_y \rightarrow 0$. Thus, we have a one-to-one correspondence between the external stress and plastic strain. If plastic deformation is time dependent, the equilibrium plastic strain for a given external stress will be reached eventually after a long time. This means that creep of a composite tends to stop, without attaining a stationary state.

Example 1: dislocation punching from a spherical inclusion

An infinitely extended, elastically isotropic and uniform body contains a spherical inclusion Ω_0 with the radius a , Fig. 5.3. σ_{ij}^A is thermal stress caused by the mismatch of thermal expansion between the inclusion and surrounding matrix. The pure shear state of σ_{ij}^A outside the inclusion can be relaxed by dislocation punching or equivalently by plastic deformation. In fact, it has been shown that if the plastic strain characterized by the strain [9]

$$\epsilon_{ij}^* = a^3 \epsilon^T \left(\frac{\delta_{ij}}{x^3} - 3 \frac{x_i x_j}{x^5} \right) \quad (5.7)$$

occurs in Ω , the total stress in Ω becomes hydrostatic; that is

$$\sigma_{ij} + \sigma_{ij}^A = -\frac{4\mu(1+\nu)}{3(1-\nu)} \epsilon^T \left(\frac{a}{R} \right)^3 \delta_{ij} \quad \text{in } \Omega. \quad (5.8)$$

Here, Ω stands for the spherically symmetric domain surrounding Ω_0 with the radius R . The center of Ω coincides with that of Ω_0 . μ is the shear modulus and ν is the Poisson ratio. ϵ^T is the

difference of thermal expansion between the inclusion and matrix, causing the eigenstrain $\varepsilon_{ij}^P = \varepsilon^T \delta_{ij}$ in Ω_0 . Although the hydrostatic stress in Ω is constant as required by Eq. (5.6), σ_{ij}^A and similarly σ_{ij} depends on the position x in Ω . σ_{ij}^A is written as

$$\sigma_{ij}^A = \frac{2\mu(1+\nu)}{3(1-\nu)} \varepsilon^T a^3 \left(\frac{\delta_{ij}}{x^3} - 3 \frac{x_i x_j}{x^5} \right) \quad \text{in } \Omega. \quad (5.9)$$

The reason why ε_{ij}^* is written in the form of Eq. (5.7) is given in Appendix 1.

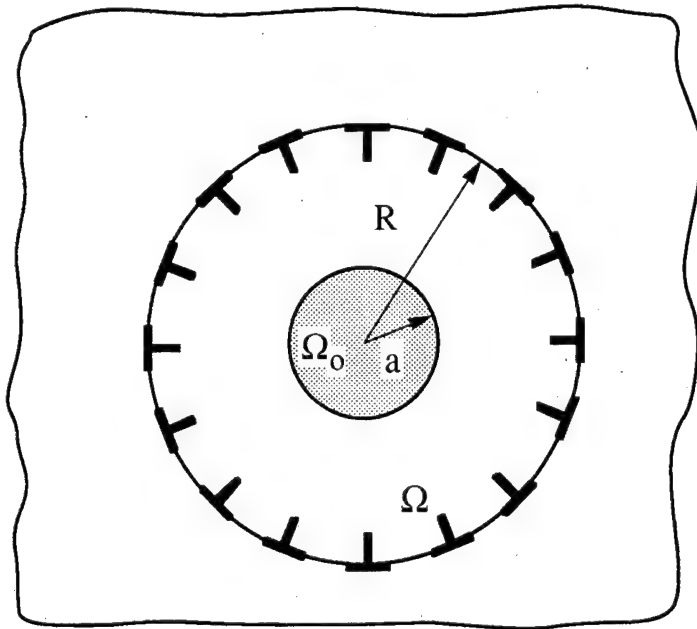


Figure 5.3. Inifinite matrix contains a spherical inclusion (Ω_0) surrounded by concentric spherical domain (Ω) where discloations are punched from the boundary of Ω_0 .

5.2.2 Sliding on the interface of an inclusion

This subject was extensively studied by Mura and his co-workers [18, 19], assuming that the total tangential traction on the interface $|\Omega|$ of an inclusion vanishes after sliding on $|\Omega|$. The following analysis justifies this assumption and indeed shows that it is the energy minimum condition. The pertinent quantities appearing in the following discussions are defined in Fig. 5.4. Let the sliding on $|\Omega|$ be b_i . b_i is the jump in displacement u_i at $|\Omega|$, that is

$$b_i = u_i(\text{in}) - u_i(\text{out}) \quad \text{on } |\Omega|. \quad (5.10)$$

b_i defined by Eq. (5.10) is generally called Somigliana dislocations.

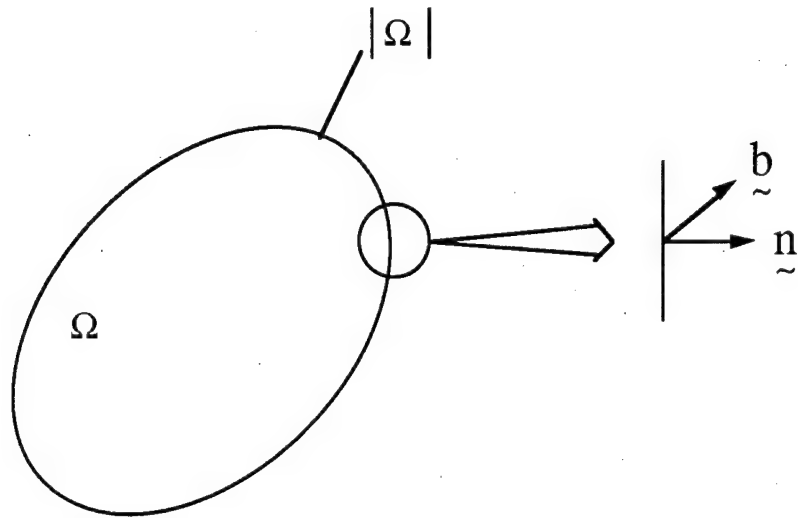


Figure 5.4. An inclusion Ω , its surface $|\Omega|$, a unit normal vector \hat{n} and the jump in displacement \hat{b} are defined in the figure.

The total energy $F[\hat{b}]$ is written as

$$F[\hat{b}] = \frac{1}{2} \int_{|\Omega|} \sigma_{ij} n_j b_i ds + \int_{|\Omega|} \sigma_{ij}^A n_j b_i ds \quad (5.11)$$

where σ_{ij} is the stress due to b_i and n_j is the unit outward normal vector on $|\Omega|$. The two terms in the right hand side of Eq. (5.11) have identical meanings to those in Eq. (5.1). b_i must satisfy

$$-n_i b_i = 0 \quad \text{on } |\Omega|. \quad (5.12)$$

This equation means that the Somigliana dislocations under consideration are of glide type.

Under condition Eq. (5.12), Eq. (5.11) becomes minimum when

$$G[\hat{b}] = \frac{1}{2} \int_{|\Omega|} \sigma_{ij} n_j b_i ds + \int_{|\Omega|} \sigma_{ij}^A n_j b_i ds - \int_{|\Omega|} \lambda n_i b_i ds \quad (5.13)$$

reaches a minimum state. Taking the variation of G with respect to b_i , the condition for the minimum of G is found as

$$\sigma_{ij}n_j + \sigma_{ij}^A n_j = \lambda(x)n_i \quad \text{on } |\Omega|. \quad (5.14)$$

That is, the complete relaxation by interfacial sliding occurs when the total traction on the interface becomes normal to the interface or the tangential traction vanishes. This result is shown in Fig. 5.1 (b).

Example 2: a spherical inclusion in an isotropic body

This subject was studied by Ghahremani [20] and Mura and Furuhashi [18]. Mura and Furuhashi took an approach similar to the present one but gave an incorrect factor in the expression for b_i . This was corrected later [21] and is recorded in Appendix 2 in the present paper.

Example 3: a circular cylinder in an isotropic body

A circular cylinder Ω of the radius a exists parallel to the x_3 axis. An external stress σ_{ij}^A ($i, j = 1, 2$) is applied at infinity. The tangential traction due to σ_{ij}^A is

$$T_i^A = \sigma_{ij}^A n_j - \sigma_{k\ell}^A n_k n_\ell n_i \quad \text{on } |\Omega|. \quad (5.15)$$

where σ_{ij}^A is the deviatoric part of σ_{ij}^A . Since the hydrostatic stress, $(\sigma_{11}^A + \sigma_{22}^A)/2$, does not cause the tangential traction, it can be excluded in analysis. Noting the form of Eq. (5.15), we postulate that b_i is given as

$$b_i = B_{ij}a^2 x_j - B_{k\ell} x_k x_\ell x_i. \quad (5.16)$$

Using the paper by Asaro [22] and Asaro and Barnett [23], the stress σ_{ij} due to Eq. (5.16) is calculated as

$$\sigma_{ij} = -\frac{3\mu}{2(1-\nu)} \delta_{ij} B_{k\ell} x_k x_\ell - \frac{\mu}{2(1-\nu)} B_{ij} (a^2 - 3x^2) \quad \text{in } \Omega. \quad (5.17)$$

Therefore, if B_{ij} is taken as

$$B_{ij} = -\frac{(1-v)}{\mu a^2} \sigma_{ij}^A \quad (5.18)$$

the total tangential traction $|\Omega|$ vanishes as verified by

$$\sigma_{ij}n_j - \sigma_{k\ell}n_k n_\ell n_i + \sigma_{ij}^A n_j - \sigma_{k\ell}^A n_k n_\ell n_i = 0. \quad (5.19)$$

5.2.3 Local diffusion around an inclusion

What we are concerned with here is the relaxation achieved by the removal of some mass from certain areas and the deposit of them on other areas (mass transport). At the moment, we do not specify the path of diffusion. This subject was, to our knowledge, first studied by Koeller and Raj [3] for a cylindrical inclusion, confining the diffusion path on the interface. Their solution is incomplete in the sense of mechanics. Thus, we will show our analysis here.

Eq. (5.11) is again used. Instead of Eq. (5.12), the conditions described by

$$b_i = \alpha(x)n_i \quad \text{on } |\Omega| \quad (5.20)$$

and

$$-\int_{|\Omega|} n_i b_i ds = -\int_{|\Omega|} \alpha ds = 0 \quad (5.21)$$

are imposed. The removal or deposit of some mass on $|\Omega|$ leads to Eq. (5.20) and the local conservation of mass to Eq. (5.21). Although the diffusion path is not specified, the removal or deposit of mass occurs only on $|\Omega|$. The Somigliana dislocations defined by Eq. (5.20) are of prismatic type.

The total energy change F is minimized when

$$G[\alpha] = \frac{1}{2} \int_{|\Omega|} \sigma_{ij} n_j \alpha n_i ds + \int_{|\Omega|} \sigma_{ij}^A n_j \alpha n_i ds - \lambda \int_{|\Omega|} \alpha ds \quad (5.22)$$

reaches a minimum. Taking the variation of Eq. (5.22) with respect to α , we find that G is minimized when

$$\sigma_{ij}n_j n_i + \sigma_{ij}^A n_j n_i = \lambda \quad \text{on } |\Omega|. \quad (5.23)$$

Since the Lagrange multiplier λ is constant in this case, it is clear that the relaxation is completed when the total normal traction on $|\Omega|$ becomes constant. In other words, if the normal traction is position dependent, a mass transport occurs further to decrease the energy. As formulated by Koeller and Raj [3], we may state that the gradient of chemical potential of an atom along the interface drives diffusion. As the above analysis indicates, the chemical potential should be taken proportion to the normal traction, regardless of hoop stresses. Although it appears redundant, we may add that the tangential traction still remains and its magnitude is position dependent. The traction on $|\Omega|$ after the different relaxation is schematically shown in Fig. 5.1 (c).

Example 4: a spherical inclusion in an isotropic body

The normal traction N^A due to σ_{ij}^A is given by

$$N^A = \sigma_{k\ell}^A n_k n_\ell \quad \text{on } |\Omega|. \quad (5.24)$$

This encourages us to postulate that b_i is written in a form of

$$b_i = B_{k\ell} x_k x_\ell x_i \quad (5.25)$$

which satisfies the conditions Eq. (5.20). We also anticipate that $B_{k\ell}$ is proportional to the deviatoric part of σ_{ij}^A , since the hydrostatic stress is uniform on $|\Omega|$ and does not induce a mass transport. The above anticipation means that

$$B_{kk} = 0 \quad (5.26)$$

Note that Eq. (5.26) with Eq. (5.25) assures the condition Eq. (5.21). By conducting calculation similar to that involved in Example 3, the stress σ_{ij} caused by Eq. (5.25) is calculated as

$$\begin{aligned}
\sigma_{ij} = & \frac{148\mu\nu}{35(1-\nu)} \delta_{ij} B_{k\ell} x_k x_\ell \\
& + \frac{4\mu}{35(1-\nu)} \left\{ -2(7-4\nu) B_{ij} x^2 - 12\nu(B_{i\ell} x_\ell x_j + B_{j\ell} x_\ell x_i) \right. \\
& \left. + 2(7-10\nu) \delta_{ij} B_{k\ell} x_k x_\ell + \frac{7}{3}(5-\nu)a^2 B_{ij} \right\} \quad \text{in } \Omega.
\end{aligned} \tag{5.27}$$

If B_{ij} is taken as

$$B_{ij} = -\frac{105(1-\nu)}{4\mu(35+11\nu)a^2} \delta_{ij}^A, \tag{5.28}$$

the total normal traction becomes independent of the position, that is

$$\sigma_{ij} n_j n_i + \sigma_{ij}^A n_j n_i = -\sigma_{kk}^A / 3 \quad \text{on } |\Omega|. \tag{5.29}$$

Example 5: a circular cylinder in an isotropic body

Similar to Example 4, we postulate that b_i has a form

$$b_i = B_{k\ell} x_k x_\ell x_i \quad (i, k, l = 1, 2). \tag{5.30}$$

By conducting a similar calculation to that having led to Eq. (5.27), it can be shown that the stress σ_{ij} due to Eq. (5.30) is given by

$$\sigma_{ij} = \frac{\mu}{2(1-\nu)} \left\{ 3\delta_{ij} B_{k\ell} x_k x_\ell + (2a^2 - 3x^2) B_{ij} \right\} \quad \text{in } \Omega. \tag{5.31}$$

The position independent condition of the total normal traction on $|\Omega|$ gives

$$B_{ij} = -\frac{(1-\nu)}{\mu a^2} \delta_{ij}^A. \tag{5.32}$$

Interestingly, this is exactly the same as Eq. (5.18). Combining Eqs. (5.31) and (5.32), we have

$$\sigma_{ij} = -\frac{3}{2a^2} \delta_{ij} \sigma_{kk}^A x_k x_\ell - \frac{1}{2} \left(2 - 3 \frac{x^2}{a^2} \right) \sigma_{ij}^A \text{ in } \Omega, \quad (5.33)$$

after the complete relaxation. The total normal traction is now

$$\sigma_{ij} n_j n_i + \sigma_{ij}^A n_i n_j = \sigma_{kk}^A / 2 \quad \text{on } |\Omega|. \quad (5.34)$$

Eq. (5.32) together with Eq. (5.30) satisfies Eqs. (5.20) and (5.21).

5.2.4 Combination of interfacial sliding and local diffusion

The total energy change is given by Eq. (5.11). However, this case requires the subsidiary condition for b_i written as

$$-\int_{|\Omega|} n_i b_i ds = 0. \quad (5.35)$$

Thus, our problem is to minimize

$$G[b] = \frac{1}{2} \int_{|\Omega|} \sigma_{ij} n_j b_i ds + \int_{|\Omega|} \sigma_{ij}^A n_j b_i ds - \lambda \int_{|\Omega|} n_i b_i ds. \quad (5.36)$$

For G to be minimum, the condition

$$\sigma_{ij} n_j + \sigma_{ij}^A n_j = \lambda n_i \quad \text{on } |\Omega| \quad (5.37)$$

must be satisfied. Here λ is constant, that is, the stress is completely relaxed when the total traction on $|\Omega|$ becomes constant and normal to $|\Omega|$, as shown in Fig. 5.1 (a). The total stress in an inclusion is not necessarily uniform nor hydrostatic. To emphasize this point, we drew Fig. 5.1 (d) differently from Fig. 5.1 (a), where the uniform hydrostatic state is schematically shown. The total stress in Fig. 5.1 (d) becomes uniformly hydrostatic at any point within Ω for an elastically uniform inclusion. This particular case was noted by Eshelby [24]. He mentioned that for an ellipsoidal inclusion Ω with an incoherent interface, having the transformation strain (eigenstrain) ϵ_{mn}^T , the total stress σ_{ij}^R in the inclusion is found by solving

$$\begin{aligned}\sigma_{ij}^R &= C_{ijkl}(S_{k\ell mn}\varepsilon_{mn}^{**} - \varepsilon_{k\ell}^{**}) \quad \text{in } \Omega \\ &= P\delta_{ij}\end{aligned}\quad (5.38)$$

with

$$\varepsilon_{kk}^{**} = \varepsilon_{kk}^T. \quad (5.39)$$

Here, C_{ijkl} is an elastic constant and $S_{k\ell mn}$ the Eshelby tensor [25]. The reasoning for Eqs. (5.38) and (5.39) is as follows:

The original ε_{mn}^T , in general, results in a stress σ_{ij}^T which is not hydrostatic but uniform in Ω . Thus, normal and tangential tractions due to σ_{ij}^T are not uniform on $|\Omega|$. This drives sliding and mass transport on $|\Omega|$. (Note that sliding and diffusion can occur quite easily on an incoherent interface.) The Somigliana dislocations, b_i , satisfy the condition Eq. (5.35). After σ_{ij}^T is completely relaxed, the total traction on $|\Omega|$ becomes uniform and normal to $|\Omega|$. Since only an elastically uniform inclusion is considered here, the stress in the inclusion becomes hydrostatic, Pd_{ij} , see Eq. (5.38). b_i can be extended to the interior of Ω , as shown by Asaro [22]. As will be shown later, the dilatation of the eigenstrain ε_{ij}^* which gives the identical stress to that due to b_i and is defined by the negative of the gradient of b_i inside Ω is zero. Thus, the dilatation of the total eigenstrain, $\varepsilon_{ij}^T + \varepsilon_{ij}^*$, is equal to that of ε_{ij}^T , see Eq. (5.39).

Example 6: a spherical inclusion in an isotropic body

Since the hydrostatic component of σ_{ij}^A causes a uniform normal traction and no tangential traction on $|\Omega|$, we will only consider the case of $\sigma_{12}^A = \sigma_0$. Apparently we can take

$$b_1 = -\varepsilon^* x_2, \quad b_2 = -\varepsilon^* x_1, \quad \text{other components are zero, on } |\Omega|. \quad (5.40)$$

As will be shown later, the stress σ_{ij} due to Eq. (5.40) can be calculated by giving Ω the eigenstrain ε_{ij}^*

$$\varepsilon_{12}^* = \varepsilon^*, \quad \text{other components are zero.} \quad (5.41)$$

σ_{ij} is now

$$\sigma_{12} = -\frac{2\mu(7-5\nu)}{15(1-\nu)} \varepsilon^*, \quad \text{other components are zero, in } \Omega. \quad (5.42)$$

Thus, if ε^* is taken to satisfy

$$\varepsilon^* = \frac{15(1-\nu)}{2\mu(7-5\nu)} \sigma_0, \quad \text{in } \Omega \quad (5.43)$$

the total stress, $\sigma_{ij}^A + \sigma_{ij}$, becomes zero in Ω , a special case of the present subsection. Note that Eq. (5.40) satisfies Eq. (5.35) and that b_i is not always normal nor parallel to $|\Omega|$. This requires that b_i must be achieved by the combination of mass transport and sliding.

What Mori, Okabe, and Mura [4] and Onaka, Okada, and Kato [8] considered as the stress relaxation around an ellipsoidal inclusion is not solely due to interfacial diffusion but also accompanies sliding, correction of Mori's earlier paper [4].

5.2.5 The combination of sliding on $|\Omega|$ and mass transport to $|\Omega|$ from an outer free surface

This case also holds for the case that vacancies flow to $|\Omega|$ from an outer free surface of the body D. No subsidiary condition is required when we minimize Eq. (5.11). It is apparent that the total energy is minimized when

$$\sigma_{ij} n_j + \sigma_{ij}^A n_j = 0 \quad \text{on } |\Omega|. \quad (5.44)$$

That is, when the inclusion under consideration becomes free from the traction on its interface. For all practical purposes, one can say that the inclusion becomes unstressed. This is the case studied by Srolovitz et al. for a spherical inclusion [5]. The stress free state, the condition of the most effective relaxation, holds for an inclusion of any shape. Note that interfacial sliding must occur in addition to diffusion.

If we impose the subsidiary condition of

$$b_i = \alpha n_i \quad \text{on } |\Omega|, \quad (5.45)$$

by excluding sliding, the minimum of Eq. (5.11) is achieved when

$$\sigma_{ij}n_j n_i + \sigma_{ij}^A n_j n_i = 0 \quad \text{on } |\Omega|. \quad (5.46)$$

This is the special case of subsection 2.3. However, the total normal traction is zero, but the tangential traction, in general, remains to be further relaxed.

5.3. Discussion

The results of the variational analysis, Eqs. (5.5), (5.14), (5.23), (5.37), (5.44), and (5.46), are necessary conditions to describe an energy minimum state. Adopting the line used by Huang and Mura [26], we can see that these conditions are also sufficient ones.

Let us take interface related phenomena. Let b_i and σ_{ij} be the Burgers vectors of the Somigliana dislocations and those stresses due to them which satisfy the necessary conditions. Suppose that δb_i is introduced, resulting in changes $\delta \sigma_{ij}$ in the stresses. Then, the change in the total potential energy is expressed as

$$\begin{aligned} & F[\underline{b} + \delta \underline{b}] - F[\underline{b}] \\ &= \frac{1}{2} \int_{|\Omega|} (\sigma_{ij} + \delta \sigma_{ij}) n_j (b_i + \delta b_i) ds + \int_{|\Omega|} \sigma_{ij}^A n_j (b_i + \delta b_i) ds - \frac{1}{2} \int_{|\Omega|} \sigma_{ij} n_j b_i ds - \int_{|\Omega|} \sigma_{ij}^A n_j b_i ds \quad (5.47) \\ &= \frac{1}{2} \int_{|\Omega|} \sigma_{ij} n_j \delta b_i ds + \frac{1}{2} \int_{|\Omega|} \delta \sigma_{ij} n_j b_i ds + \frac{1}{2} \int_{|\Omega|} \delta \sigma_{ij} n_j \delta b_i ds + \int_{|\Omega|} \sigma_{ij}^A n_j \delta b_i ds. \end{aligned}$$

Because of the Maxwell-Betti reciprocal theorem

$$\int_{|\Omega|} \sigma_{ij} n_j \delta b_i ds = \int_{|\Omega|} \delta \sigma_{ij} n_j b_i ds, \quad (5.48)$$

Eq. (5.47) is rewritten as

$$\begin{aligned} & F[\underline{b} + \delta \underline{b}] - F[\underline{b}] \\ &= \int_{|\Omega|} (\sigma_{ij} + \sigma_{ij}^A) n_j \delta b_i ds + \frac{1}{2} \int_{|\Omega|} \delta \sigma_{ij} n_j \delta b_i ds. \quad (5.49) \end{aligned}$$

Because of the conditions, Eqs. (5.14), (5.23), (5.37), (5.44), and (5.46), together with the corresponding subsidiary conditions Eqs. (5.12), (5.20), (5.21), (5.35), and (5.45), the first term

in Eq. (5.49) vanishes. The second term is the elastic energy of the Somigliana dislocations of the Burgers vector δb_i . It must be positive for non-vanishing δb_i . Thus,

$$F[b + \delta b] > F[b], \quad (5.50)$$

which proves that the necessary conditions are also the sufficient ones. Almost identical discussion can be given to the case of plastic flow.

The energy expressions, Eqs. (5.1) and (5.11), do not contain an energy dissipation term. The energy dissipation in plastic flow depends on the path or mode of deformation. It is caused by non-zero resistance to plastic flow. Thus, the direct application of Eq. (5.5) is only valid for creep deformation, since no threshold stress exists in creep. Similarly, the interface related relaxations, sliding and diffusion, occur with no threshold stress. Thus, the resulting expressions, Eqs. (5.14), (5.23), (5.37), (5.44), and (5.46), are always valid. Diffusion is caused by a gradient of a chemical potential of an atom; the chemical potential is proportional to stresses. Thus, diffusion occurs if a stress is position dependent even when its magnitude is small. Similarly, interfacial sliding occurs proportional to the tangential traction on an interface, as evidenced experimentally by grain boundary sliding [27] and analyzed theoretically [28].

Now, the strength of relaxations due to specific modes examined in the present paper is discussed. The strength here means the effectiveness of the relaxation modes: the larger the energy decrease, the more effective the process. The sliding and diffusion processes cannot be compared, since the conditions for the two processes, Eqs. (5.12), (5.20) and (5.21), are independent of each other. Mathematically, this is expressed by the fact that Eq. (5.12) is not a part of Eqs. (5.20) and (5.21), or (5.20) and (5.21) is not of Eq. (5.12). On the other hand, the combination of sliding and diffusion ($S \cup D$) has the condition Eq. (5.35) which includes the condition Eq. (5.12) for sliding (S) and those Eqs. (5.20) and (5.21) for diffusion (D). Thus, we have

$$F_{\min}(S \cup D) \leq F_{\min}(S) \quad (5.51)$$

$$F_{\min}(S \cup D) \leq F_{\min}(D), \quad (5.52)$$

that is, the combined sliding and diffusion process is more effective in relaxation than the separately occurring sliding and diffusion processes. In this respect, one should recall that the climb and annihilation process of an Orowan loop (shear loop) also accompanies diffusion (pipe-diffusion) and glide motion [29]. This is the process to relax internal stresses developed by plastic deformation in an inclusion bearing material. When all the loops are annihilated, the total energy

becomes zero; the lowest energy state. Similarly, if bulk diffusion from or to a normal traction free surface is allowed, we have a more effective way of relaxation. This is because no condition for mass conservation such as Eqs. (5.21) and (5.35) is imposed in a process allowing bulk diffusion. It is clear that bulk diffusion with sliding reduces energies more effectively than that without sliding.

The combined process of sliding and diffusion can be compared with plastic flow. As shown by Asaro,[22] the stress caused by b_i on the interface $|\Omega|$ of an inclusion Ω can be reproduced by giving the eigenstrain

$$\varepsilon_{ij}^* = -(b_{i,j} + b_{j,i})/2 \quad \text{in } \Omega \quad (5.53)$$

to Ω . If we understand ε_{ij}^* such that ε_{ij}^* is produced by plastic flow ($\varepsilon_{ii}^* = 0$), we have

$$-b_{i,i} = 0 \quad \text{in } \Omega. \quad (5.54)$$

Integrating Eq. (5.54) in Ω and applying the Gauss-Green theorem, we see

$$-\int_{|\Omega|} b_i n_i ds = 0, \quad (5.55)$$

which is identical to Eq. (5.35). That is, the condition for plastic flow (P) is included in the condition for the combination of sliding and diffusion. On the other hand, the condition Eq. (5.35) does not necessarily lead to that in Eq. (5.2) for every point in Ω . Thus,

$$F_{\min}(S \cup D) \leq F_{\min}(P). \quad (5.56)$$

In short, the most effective process to achieve the stress relaxation is the one allowing bulk diffusion and interfacial sliding among all the processes examined in the present study.

However, what occurs in an actual situation also depends on kinetics. Bulk diffusion takes a long time and can be excluded at low temperatures when interfacial sliding and diffusion can occur with a sufficient rate. The kinetics cannot be discussed in a general manner even when the relaxation process is limited to interfacial phenomena, the kinetics depends on the shape of an inclusion [8]. Confining to interfacial phenomena and separately examining sliding and diffusion, one can see from other studies [2-5, 8] that the relaxation occurs in the first order kinetics. For a round-shaped or cylindrical inclusion, the relaxation time is proportional to the cube of the inclusion radius for interfacial diffusion (τ_D) and to the radius for interfacial sliding (τ_S). Thus,

above a critical radius, the rate-controlling process in the interfacial relaxation is diffusion. We can roughly estimate the critical radius. Ignoring the detailed geometrical factor, the relaxation times are given as [2-4]

$$\tau_D \equiv \frac{kT}{D} \frac{a^3}{h\mu\Omega} \quad (5.57)$$

$$\tau_s \equiv \frac{a\eta}{\mu h} \quad (5.58)$$

Here, D is the interfacial diffusivity, a the radius, h the thickness of the interface layer, Ω the atomic volume, h the interface viscosity and kT has the usual meaning. For a disordered boundary such as an incoherent inclusion/matrix interface Ashby [28] estimated

$$\eta = \frac{kT}{8bD} \quad (5.59)$$

where b is the atomic size. Eqs. (5.58) and (5.59) result in

$$\tau_s \equiv \frac{kT}{D} \frac{a}{8\mu b h} \quad (5.60)$$

Since $h \approx b$ and $\Omega \approx b^3$, Eqs. (5.57) and (5.60) lead to the critical radius of the order of the atomic size. Thus, for an ordinary inclusion to be discerned as a second phase, sliding occurs first, followed by interfacial diffusion. It was in fact evidenced by several experiments [30-32] with the observations that the annihilation rate of internal stresses in Fe-particles embedded in Cu is inversely proportional to the cube of the particle radius. Of course, the annihilation must be accompanied by sliding. This interfacial diffusion will also accompany sliding, occurring fast, to achieve the condition, Eq. (5.37). The coexistence of sliding and diffusion is necessary, similar to diffusional creep of a polycrystal which accompanies grain boundary sliding [1].

Finally, we will briefly discuss the case that σ_{ij}^A is produced by an external load. When the load is removed, the internal stress due to ε_{ij}^* on b_i remains. This means that the stress is again relaxed by a reverse process. The reverse process follows the path of a forward process or a different path. In the former case, a body behaves as an anelastic material. The latter case is realized, for example, when a forward process is plastic deformation in a matrix surrounding inclusions and a reverse process is achieved by the combination of local diffusion and sliding on the interface of the inclusions.

5.4. Summary

The stress relaxation in an inclusion bearing material has been examined from a mechanics point of view with the aid of variational approach. Four processes have been dealt with: plastic flow, interfacial sliding, local diffusion, and bulk diffusion. Some of them have been combined. Each process or combination involves a physical process which restricts the plastic strain or sliding. The restriction involves a subsidiary condition when one seeks the minimum state of the total energy achieved by a particular relaxation process. The minimum state is described by an elastic state designated by the relaxation process under consideration. By examining the subsidiary conditions the effectiveness of two relaxation processes can be compared.

5.5. References

1. Raj, R. and Ashby, M.F., Metall. Trans., 2, 1113 (1971).
2. Shibata, S., Jasiuk, I., Mori, T. and Mura, T., Mech. Materials, 9, 229 (1990).
3. Koeller, R.C. and Raj, R., Acta Metall., 26, 1551 (1978).
4. Mori, T., Okabe, M. and Mura, T., Acta Metall., 28, 319 (1980).
5. Srolovitz, D.J., Petkovic-Luton, R.A. and Luton, M.J., Phil. Mag. A, 48, 795 (1983).
6. Srolovitz, D.J., Luton, M.J., Petkovic-Luton, R., Barnett, D.M. and Nix, W.D., Acta Metall., 32, 1079 (1984).
7. Onaka, S., Miura, S. and Kato, M., Mech. Materials, 8, 285 (1990).
8. Onaka, S., Okada, T. and Kato, M., Acta Metall., 39, 971 (1991).
9. Shibata, S., Taya, M., Mori, T. and Mura, T., Acta Metall., 40, 3141 (1992).
10. Rosler, J., Bao, G. and Evans, A.G., Acta Metall., 39, 2733 (1991).
11. Dragon, T.L. and Nix, W.D., Acta Metall., 38, 1441 (1990).
12. Mori, T. and Tanaka, K., Acta Metall., 21, 571 (1973).
13. Mori, T. and Wakashima, K., to appear in Proc. J. Weentman Symp. TMS, Anaheim, Feb. 1996.
14. Kim, K.T. and McMeeking, R.M., Mech. Materials, 20, 153 (1995).
15. Goto, S. and McLean, M., Acta Metall. Mater., 39, 165 (1991).
16. Tanaka, K. and Mori, T., Acta Metall., 18, 931 (1970).
17. Brown, L. M. and Stobbs, W. M., Phil Mag., 23, 1185 (1971).
18. Mura, T. and Furuhashi, R., J. Appl. Mech., 51, 308 (1984).
19. Mura, T., Jasiuk, I. and Tsuchida, E., J. Solids Structures, 21, 1165 (1985).
20. Ghahremani, F., Int. J. Solids Structures, 10, 825 (1980).

21. Furuhashi, R., Mori, T. and Mura, T., Res. Report, Faculty of Eng. Meiji Univ., 60, 39 (1991).
22. Asaro, R.J., Int. J. Eng. Sci., 13, 271 (1975).
23. Asaro, R.J. and Barnett, D.M., J. Mech. Phys. Solids, 23, 77 (1975).
24. Eshelby, J.D., Progress in Solid Mechanics, North-Holland, Amsterdam, 2, 86 (1961).
25. Eshelby, J.D., Proc. Roy. Soc. London, A241, 376 (1957).
26. Huang, J.H. and Mura, T., Appl. Mech. Rev., 47, No. 1, Part 2, S10 (1994).
27. Ke, T.S., Phys. Rev., 71, 533 (1947).
28. Ashby, M.F., Surf. Sci., 31, 498 (1972).
29. Mori, T. and Tokushige, H., Acta Metall., 25, 635 (1977).
30. Monzen, R., Kato, M. and Mori, T., Acta Metall., 37, 3177 (1989).
31. Monzen, R. and Mori, T., Materials Sci. Eng. A, 149, 53 (1991).
32. Monzen, R. and Mori, T., Materials Sci. Eng. A, 209 (1993).
33. Mura, T., , Micromechanics of Defects in Solids, Martinus Nijhoff, Dordrecht, p. 343 (1991).

Appendix 1: Dislocation punching from a spherical inclusion referred to Fig. 5.3.

Because of the spherical symmetry, we can assume that the displacement, u_i^* , the derivative of which gives the plastic strain is expressed by

$$u_i^* = \frac{x_i}{x} f(x) \quad (A1)$$

Here $f(x)$ is a function, to be determined, of the distance from the center to the point x ,

$$x = \sqrt{x_i x_i} \cdot \varepsilon_{ii}^* = u_{i,i}^* = 0 \text{ gives}$$

$$-\frac{df}{dx} - 2 \frac{f}{x} = 0 \quad (A2)$$

This is solved as

$$f(x) = \frac{c}{x^2} \quad (A3)$$

with a constant c . Inserting Eq. (A3) into Eq. (A1) and differentiating u_i^* , we have ε_{ij}^*

$$\varepsilon_{ij}^* = c \left(\frac{\delta_{ij}}{x^3} - 3 \frac{x_i x_j}{x^5} \right) \quad \text{in } \Omega. \quad (\text{A4})$$

The eigenstrains inside Ω_0 and in Ω jump on $|\Omega_0| = |\Omega|$. Thus, surface dislocations are defined [33]. The vanishing condition for the surface dislocations on $|\Omega|$ gives

$$c = \varepsilon^T / a^3. \quad (\text{A5})$$

In this calculation, we excluded impotent dislocations [33], since they produce no elastic field.

Appendix 2: Spherical sliding inclusion.

The stress field due to sliding b_i on the interface of a spherical inclusion in an isotropic body. The hydrostatic component of σ_{ij}^A does not induce the tangential traction T_i^A on $|\Omega|$. Thus, only the deviatoric part ' σ_{ij}^A ' is included in the calculation. T_i^A is written as

$$T_i^A = ' \sigma_{ij}^A n_j - ' \sigma_{k\ell}^A n_k n_\ell n_i, \quad (\text{A6})$$

with which we postulate that b_i is given by

$$b_i = B_{ij} a^2 x_j - B_{k\ell} x_k x_\ell x_i. \quad (\text{A7})$$

Defining the eigenstrain ε_{ij}^* with Eqs. (5.53) and (A7), we can calculate the stress σ_{ij} due to b_i as

$$\begin{aligned} \sigma_{ij} = & 2\mu \frac{(7-5v)}{15(1-v)} a^2 B_{ij} - \frac{168\mu v}{35(1-v)} \delta_{ij} B_{k\ell} x_k x_\ell \\ & + \frac{4\mu}{35(1-v)} \left\{ 2(7-4v) B_{ij} x^2 + 12v(B_{i\ell} x_\ell x_j + B_{j\ell} x_\ell x_i) \right. \\ & \left. - 2(7-10v) B_{k\ell} x_k x_\ell \delta_{ij} - \frac{7}{3}(5-v)a^2 B_{ij} \right\} \quad \text{in } \Omega. \end{aligned} \quad (\text{A8})$$

The stress outside Ω is very complicated and is not recorded here.

The tangential traction T_i due to σ_{ij} on $|\Omega|$ is

$$T_i = \sigma_{ij}n_j - \sigma_{k\ell}n_k n_\ell n_i. \quad (A9)$$

The condition

$$T_i + T_i^A = 0 \quad (A10)$$

gives

$$B_{ij} = -\frac{35(1-v)}{2\mu(21+v)a^2} \sigma_{ij}^A. \quad (A11)$$

6. Analytical Study IV: Dislocation Punching in Functionally-Graded Materials

6.1 Introduction

As a metal/ceramic composite is subjected to temperature change ΔT , a stress field of large magnitude is induced due to the difference in the coefficients of thermal expansion (CTE) and ΔT . Some relaxation processes must operate to reduce the large stresses. Dislocation punching is one of them and has successfully been applied to dispersion hardened alloys [1-3] and metal matrix composites [4-9]. Consequences of the punching have been examined in terms of a strength decrease or increase.

When a metal/ceramic interface is planar, a similar relaxation mechanism by dislocation punching from the interface is expected to occur. Shieh and Sass [10] studied both theoretically and experimentally the dislocation mechanisms to relax thermal stress in a Pt film on NiO substrate. They suggested that as a sample is cooled from high temperature to room temperature, the dislocation punching takes place first in a climb mode, then followed by a glide mode process during further cooling. Parallel to the dislocation punching from a thin metal coating/ceramic substrate system, the generation of dislocations at a metal/ceramic interface has also been studied in terms of critical thickness [11,12]. These studies were aimed at epitaxial layers. Taya and Mori [13] recently examined a dislocation punching mechanism from a single interface of a thin metal coating over a thick ceramic substrate, using a simple analytical model. They examined a criterion for the punching to occur and determined a critical magnitude of the CTE mismatch strain, beyond which the punching occurs. A thin metal coating over a ceramic substrate is widely used in electronic packaging, where the microstructure of a thin metal coating bonded to a ceramic substrate can be tailored to form a functionally graded material (FGM), the composition being smoothly graded from metal to ceramic phases.

In this report, we will develop a new dislocation punching model for FGM. Using Eshelby's inclusion theory [14] and the average field approach [15], the punching condition and plastic strain in a metal phase will be determined. A FGM layer consists of sublayers with different compositions of metal and ceramic. The relaxation of thermal stress in these sublayers, hereafter called simply layers, will be examined. The analysis is rather simple, since the compositions of metal and ceramic phases changes one-dimensionally perpendicular to the interface between the substrate and overlayer. We will determine the critical CTE mismatch strain to induce the relaxation as a function of the volume fraction of the ceramic phase.

6.2 Model and Analysis

6.2.1 Elastic analysis

A functionally-graded material (FGM) consists of several thin coating layers and a thick ceramic substrate as schematically shown in Fig. 6.1. The i -th layer can be approximated as a flat inclusion, parallel to the substrate/overlayer interface. The direction normal to the interface is along the x_3 -axis. When such a flat inclusion with uniform eigenstrains exists in an infinite matrix, all the components of the stress and total strain in the matrix become zero [16]. Here, the eigenstrain and total strain are defined with respect to the matrix. Thus, the inclusion causes no stress field outside it. This means that as far as the thickness of a substrate is sufficiently large, the elastic state of the i -th layer can be examined, independent of the other layers. The present model assumes that the thickness of the i -th layer is much smaller than that of the substrate. We further assume that the i -th layer has uniform eigenstrain as a whole when the overall elastic state is evaluated for the layer. The overall elastic state is an ensemble of those of the constituting phases. The latter can be calculated, using the average field theory [15].

Consider that FGM is subjected to a temperature change and then a thermal mismatch strain relative to the ceramic substrate is generated in the metal phase due to CTE mismatch. There are two conceivable structures in the i -th layer: ceramic inclusions are surrounded by a metal matrix (Model A), Fig. 6.2 (a), and metal inclusions are present in a ceramic matrix (Model B), Fig. 6.2 (b). In Fig. 6.2 inclusions are shown as isolated spherical islands. The CTE mismatch strain in the metal relative to the ceramic substrate is given by

$$\varepsilon_{ij}^T = (\alpha_m - \alpha_c) \Delta T \delta_{ij} = \alpha^* \delta_{ij} \quad (6.1)$$

where α_m and α_c are the CTEs of metal and ceramic, respectively, and ΔT is the temperature change.

Suppose that the relaxation is achieved by uniform plastic strain ε_p^p in the metal phase, as given by

$$\varepsilon_p^p = \varepsilon_p [1 \ 1 \ -2 \ 0 \ 0 \ 0] \quad (6.2)$$

where ε_p is the magnitude of the plastic strain along the x_1 and x_2 directions.

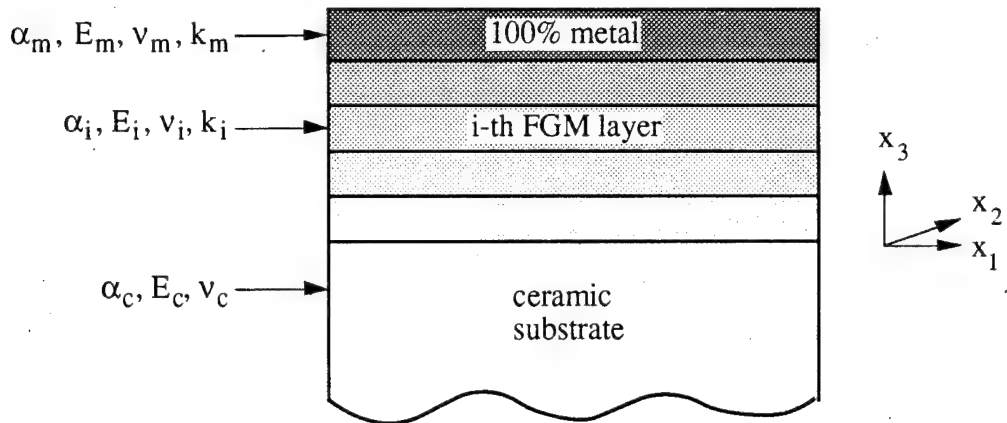


Figure 6.1 Schematic diagram of FGM which has multiple layers from a ceramic substrate to a metal layer.

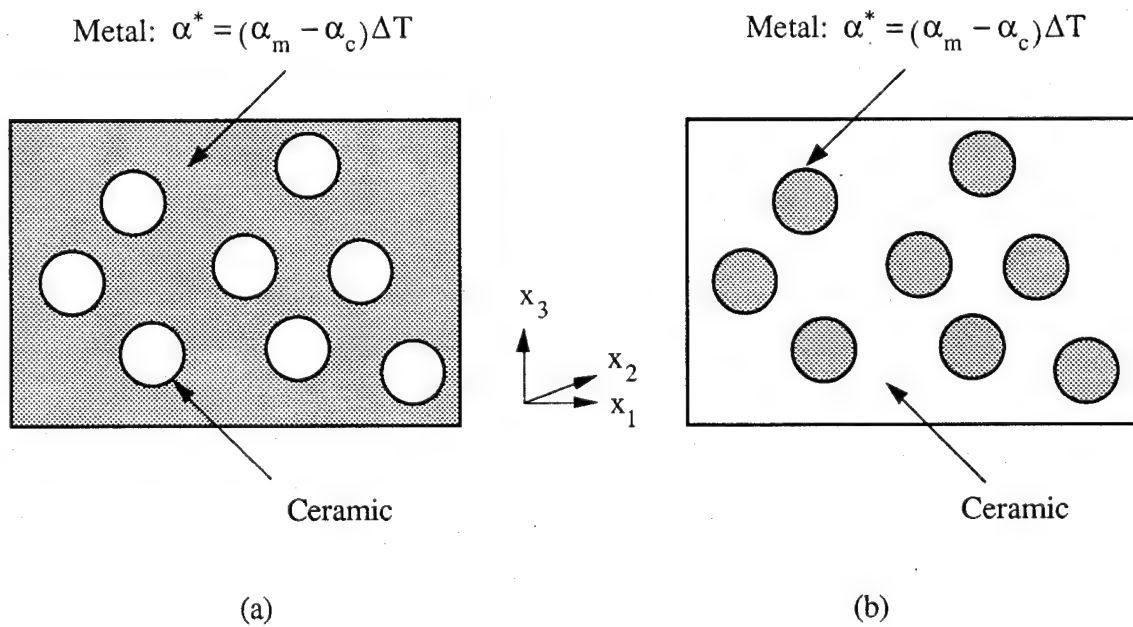


Figure 6.2 Microstructure of the i -th layer: (a) Model A and (b) Model B.

Now, we will examine the elastic state of the i -th layer when a temperature change is induced. If thermal stress is large, relaxation due to plastic deformation in the metal phase occurs. This relaxation is equal to dislocation punching from the interfaces between FGM layers. This problem can be analyzed by conducting the following hypothetical procedure, using Model A. This hypothetical procedure is employed to apply the average field theory [15]. Model B is similarly dealt with, by changing the roles of elastic constants for the matrix and inclusions. First,

the i -th layer is hypothetically removed from FGM. Next, a temperature change is introduced, inducing eigenstrains in the metal, Eq. (6.1). Further, plastic strains, Eq. (6.2), whose magnitude is to be determined later, are introduced into the metal matrix. Now, we will apply the Eshelby theory [14] to the isolated i -th layer. Since the eigenstrains, Eqs. (6.1) and (6.2), are defined in the matrix (metal), we will superimpose $-\tilde{\epsilon}^T$ and $-\tilde{\epsilon}^P$ over the whole domain of the i -th layer so that the resulting problem can be reduced to the Eshelby's elasticity problem where the eigenstrains are only given in the ceramic inclusions. This induces no additional stress. By using the equivalency condition and assuming that the ceramic particles are ellipsoidal, the average stress σ_c in the ceramic particles is calculated by solving

$$\begin{aligned}\sigma_c &= \mathbf{C}_c \cdot \left(\bar{\mathbf{e}} + \mathbf{e} + \tilde{\epsilon}^T + \tilde{\epsilon}^P \right) \\ &= \mathbf{C}_m \cdot \left(\bar{\mathbf{e}} + \mathbf{e} - \tilde{\epsilon}^{1*} \right).\end{aligned}\quad (6.3)$$

Here \mathbf{C} is the stiffness tensor, \mathbf{e} is the total strain in a single particle, $\bar{\mathbf{e}}$ is the average elastic strain in the matrix domain, $\tilde{\epsilon}^{1*}$ is the equivalent eigenstrain of the equivalent inclusion yet to be determined, subscripts m and c refer to the matrix metal and ceramic particle, respectively. The integration of the stress over the whole i -th layer vanishes, thus giving

$$\bar{\mathbf{e}} = -f \left(\mathbf{e} - \tilde{\epsilon}^{1*} \right) \quad (6.4)$$

The total strain \mathbf{e} is related to $\tilde{\epsilon}^{1*}$ through Eshelby's tensor \mathbf{S} as

$$\mathbf{e} = \mathbf{S} \cdot \tilde{\epsilon}^{1*} \quad (6.5)$$

From Eqs. (6.3)~(6.5), the average stress in the metal matrix due to both the CTE mismatch strain and the plastic strain, $\sigma_m^{m,T}$ and $\sigma_m^{m,P}$, respectively, can be computed as

$$\sigma_{11}^{m,T} = \sigma_{22}^{m,T} = \sigma_{33}^{m,T} = -2f\mu_m\zeta\alpha^* \quad (6.6)$$

$$\sigma_{11}^{m,P} = \sigma_{22}^{m,P} = 2f\mu_m\gamma_{11}\epsilon_p, \quad \sigma_{33}^{m,P} = 2f\mu_m\gamma_{33}\epsilon_p \quad (6.7)$$

where f and μ_m denote the volume fraction of ceramic particles and the shear modulus of the metal, respectively. γ_{11} , γ_{33} and ζ are given by

$$\gamma_{11} = \frac{2 \frac{\mu_c}{\mu_m} [- (5v_m + 9)(C_{22} + 2C_{12}) + (5v_m + 1)(C_{21} + 2C_{11})]}{15(1 - v_m)(C_{11}C_{22} - C_{12}C_{21})} \quad (6.8)$$

$$\gamma_{33} = \frac{4 \frac{\mu_c}{\mu_m} [- (5v_m + 1)(C_{22} + 2C_{12}) + 4(C_{21} + 2C_{11})]}{15(1 - v_m)(C_{11}C_{22} - C_{12}C_{21})} \quad (6.9)$$

$$\zeta = \frac{2(1 + v_m)}{3(1 - v_m)} [(1 - f)P + 1] \quad (6.10)$$

where v represents the Possion ratio of the matrix metal,

$$P = \frac{2(1 - 2v_m)(3\bar{\lambda} + 2\bar{\mu})}{(1 - v_m) \left\{ (1 - f) \frac{(1 + v_m)}{(1 - v_m)} (3\bar{\lambda} + 2\bar{\mu}) + 3[f(3\lambda_c + 2\mu_c) + (1 - f)(3\lambda_m + 2\mu_m)] \right\}} \quad (6.11)$$

$$\bar{\lambda} = \lambda_c - \lambda_m, \bar{\mu} = \mu_c - \mu_m. \quad (6.12)$$

λ is Lame's constant and C_{11} , C_{12} , C_{21} and C_{22} are tabulated in Appendix. In these calculations, Eqs. (6.8)~(6.11), we have assumed that the ceramic particles are spherical.

The elastic energy change ΔU_1 per unit volume of the i -th layer is defined as $\frac{1}{2D} \int_{\Omega} \sigma_{ij} (\epsilon_{ij}^p + \epsilon_{ij}^T) dv$, where D and Ω denote the volume of the i -th layer and the domain of the ceramic particles. ΔU_1 can be computed from Eqs. (6.1), (6.2), (6.6) and (6.7), and is calculated as

$$\Delta U_1 = -f(1 - f)\mu_m \left[2\Delta\gamma \epsilon_p^2 + (2\gamma_{11} + \gamma_{33})\alpha^* \epsilon_p - 3\zeta(\alpha^*)^2 \right] \quad (6.13)$$

with $\Delta\gamma = \gamma_{11} - \gamma_{33}$.

Finally, the freed i -th layer, hypothetically detached in the previous stage, is reattached to FGM. Since the i -th layer has a permanent strain due to the plastic and CTE mismatch strains relative to the ceramic substrate, the whole i -th layer should be elastically strained until the total strain in the i -th layer becomes equal to the strain of the substrate. The average total strain of the i -th layer is the sum of the CTE mismatch strain, plastic strain and eigenstrain accounting for different elastic moduli of the i -th layer and can be expressed as

$$\tilde{\epsilon}_{ij}^{*a} = \tilde{\epsilon}_{ij}^T + \tilde{\epsilon}_{ij}^P + f \tilde{\epsilon}_{ij}^{1*} \quad (6.14)$$

where $\tilde{\epsilon}_{ij}^{1*}$ is defined in Eq. (6.3). The first two terms are to compensate the uniformly superimposed eigenstrains, $-\tilde{\epsilon}_{ij}^T$ and $-\tilde{\epsilon}_{ij}^P$, to establish Eq. (6.3). The relevant components of $\tilde{\epsilon}_{ij}^{*a}$ are given by

$$\tilde{\epsilon}_{11}^{*a} = \tilde{\epsilon}_{22}^{*a} = (1-f)(1-fP)\alpha^* + \Phi \epsilon_p \quad (6.15)$$

where

$$\Phi = 1-f \frac{2(C_{22} + 2C_{12})}{(C_{11}C_{22} - C_{12}C_{21})} \frac{\mu_c}{\mu_m} \quad (6.16)$$

Since the average stress component σ_{33}^0 in the i -th layer is zero and the elastic strain needed for the reattachment is the negative of Eq. (6.15), the stress of the i -th layer due to this permanent strain is computed as by using the Hooke's law

$$\sigma_{11}^0 = \sigma_{22}^0 = -\frac{E_i}{(1-v_i)} \tilde{\epsilon}_{11}^{*a}, \quad \sigma_{33}^0 = 0 \quad (6.17)$$

where E_i and v_i are Young's modulus and the Poisson ratio of the i -th layer, respectively and are computed by the average field method combined with the Eshelby theory [14, 15]. This straining process increases the strain energy density of the i -th layer by ΔU_2 , which is defined as $-\frac{1}{2} \sigma_{ij}^0 \tilde{\epsilon}_{ij}^{*a}$ and computed by Eqs. (6.15) and (6.17) as

$$\Delta U_2 = \frac{E_i}{1-v_i} \left[(1-f)(1-fP)\alpha^* + \Phi \epsilon_p \right]^2 \quad (6.18)$$

The change in the total elastic energy density of the i -th layer, ΔU , subjected to the temperature change with its metal phase undergone plastic deformation, is the sum of Eqs. (6.13) and (6.18) as given by

$$\Delta U = -f(1-f)\mu_m \left[2\Delta\gamma\epsilon_p^2 + (2\gamma_{11} + \gamma_{33})\alpha^*\epsilon_p - 3\zeta(\alpha^*)^2 \right] + \frac{E_i}{1-v_i} \left[(1-f)(1-fP)\alpha^* + \Phi\epsilon_p \right]^2 \quad (6.19)$$

6.2.2 Plastic work

The metal matrix is assumed to be elastic-perfectly plastic, while ceramic particles deform only elastically. The work dissipated by the plastic deformation of the metal matrix per unit volume of the i -th layer can be expressed as

$$W = 4k(1-f)\epsilon_p \quad (6.20)$$

where k is the yield stress of the metal matrix in shear deformation.

6.2.3 Critical CTE mismatch strain for relaxation

The minimum CTE mismatch strain which can initiate the dislocation punching (or plastic relaxation) is defined as the critical CTE mismatch strain. If the reduction in the elastic energy of the i -th layer due to the plastic deformation is larger than the work required for the plastic deformation of the metal matrix of the i -th layer, the dislocation punching takes place ($\Delta U + W < 0$). Since thermal activation is ignored in the present case, the following condition,

$$\left. \frac{\partial(\Delta U)}{\partial\epsilon_p} \right|_{\epsilon_p=0} + \left. \frac{\partial W}{\partial\epsilon_p} \right|_{\epsilon_p=0} \leq 0, \quad (6.21)$$

in addition to $\Delta U + W < 0$, must be met for the relaxation to occur. Eq. (6.21) is satisfied when

$$\alpha^* \leq \alpha^{*c} \quad (6.22)$$

It is noted in Eq. (6.22) that since α^* , and α^{*c} are both negative, Eq. (6.22) can be rewritten as

$$|\alpha^*| \geq |\alpha^{*c}| \quad (6.22)'$$

where the critical CTE mismatch strain, α^{*c} , is given by

$$\alpha^{*c} = \frac{4k}{f\mu_m(2\gamma_{11} + \gamma_{33}) - \frac{2E_i}{1-v_i}(1-fP)\Phi} \quad (6.23)$$

6.2.4 Plastic strain in the metal

When the absolute magnitude of the actual CTE mismatch strain is larger than that of the critical one, the dislocation punching takes place in the metal domain of the i -th layer. The magnitude of plastic strain is determined by minimizing the sum of the elastic strain energy change and plastic work with respect to the plastic strain, as expressed by

$$\frac{\partial(\Delta U)}{\partial \epsilon_p} + \frac{\partial W}{\partial \epsilon_p} = 0 \quad (6.24)$$

Inserting Eqs. (6.19) and (6.20) into Eq. (6.24), the plastic strain can be computed as

$$\epsilon_p = \frac{(1-f)\left\{-4k + \left[f\mu_m(2\gamma_{11} + \gamma_{33}) - \frac{2E_i}{1-v_i}(1-fP)\Phi\right]\alpha^*\right\}}{-4f(1-f)\mu_m\Delta\gamma + \frac{2E_i}{1-v_i}\Phi^2} \quad (6.25)$$

6.2.5 The average stress in the metal and ceramic

The average stresses both in the metal and ceramic phases can be given by combining the stresses due to the CTE mismatch strain and plastic strain in the hypothetically free state and those due to the reattachment process. The stresses by the first two sources are given in Eqs. (6.6) and (6.7). The stresses in ceramic particles by the last origin can be computed by Eshelby's equivalent inclusion method as

$$\begin{aligned}\underline{\sigma}_c &= \mathbf{C}_c \cdot (\mathbf{e}^0 + \bar{\mathbf{e}} + \mathbf{e}) \\ &= \mathbf{C}_m \cdot (\mathbf{e}^0 + \bar{\mathbf{e}} + \mathbf{e} - \underline{\varepsilon}^2),\end{aligned}\quad (6.26)$$

where $\mathbf{e}^0 = \mathbf{C}_m^{-1} \cdot \underline{\sigma}^0$ and the components of $\underline{\sigma}^0$ are defined in Eq. (6.17). By solving Eq. (6.26) with the same steps as Eqs. (6.4) and (6.5), the stresses in the metal due to $\underline{\sigma}^0$ can be expressed as

$$\sigma_{11}^{m,0} = \sigma_{22}^{m,0} = 2\mu_m \beta_{11} \sigma_{11}^0 / E_m, \quad \sigma_{33}^{m,0} = 2\mu_m \beta_{33} \sigma_{11}^0 / E_m \quad (6.27)$$

where

$$\beta_{11} = -f \frac{[-(5v_m + 9)(D_1 C_{22} - D_2 C_{12}) + (5v_m + 1)(D_1 C_{21} - D_2 C_{11})]}{15(1 - v_m)(C_{11} C_{22} - C_{12} C_{21})} + 1 + v_m \quad (6.28)$$

$$\beta_{33} = -f \frac{[-2(1 + 5v_m)(D_1 C_{22} - D_2 C_{12}) + 8(D_1 C_{21} - D_2 C_{11})]}{15(1 - v_m)(C_{11} C_{22} - C_{12} C_{21})} \quad (6.29)$$

and where D is tabulated in Appendix. The total stress in the metal can be computed, using Eqs. (6.6), (6.7) and (6.27).

6.3 Discussion

In order to demonstrate the effectiveness of the above analysis, we will discuss here the dislocation punching, equivalently plastic relaxation, using a model system of palladium (Pd) coatings on an Al_2O_3 substrate. The thermomechanical properties of Pd and Al_2O_3 are given in Table 6.1. We consider that Pd/ Al_2O_3 is cooled from 270 °C to room temperature (20°C), thus $\Delta T = -250$ °C.

Table 6.1 Material properties for computation

	Pd	Al ₂ O ₃
Young's Modulus (GPa)	112	363
Poisson ratio	0.39	0.25
CTE ($\times 10^{-6}$)	11.6	5.4
Yield stress in shear (MPa)	26	-
Temperature difference (ΔT)		-250

6.3.1 Critical CTE mismatch strain

The critical CTE mismatch strain in Model A is shown against the volume fraction of ceramic particles (f) in Fig. 6.3. As the volume fraction of the ceramic particles increases, the absolute magnitude of the critical CTE mismatch strain increases. For smaller f 's, $|\alpha^*| \geq |\alpha^{*c}|$, thus the dislocation punching takes place, resulting in the plastic deformation in the metal phase. As f increases beyond the intersecting point with $|\alpha^*| = 1.55 \times 10^{-3}$, shown as dash-dot line in Fig. 6.3, the dislocation punching can not take place, where the intersecting points of the two critical strains with the horizontal line (f^*) are 0.87 for Model A and 0.81 for Model B. If α^* changes, f^* changes according to Eqs. (6.22) and (6.23).

Fig. 6.3 also shows the critical CTE strain α^{*c} computed in Model B. It is smaller than that in Model A. This result is not surprising, since the structure differs in the two models. We now discuss why α^{*c} is smaller in Model B than in Model A. We believe that the reason for it is similar to the difference between the upper and lower bounds in the Hashin-Shtrikman theory of the elastic constants of a two phase material [17]. As proved by Wakashima [18], the average field theory with spherical inhomogeneities gives the overall modulus, exactly coinciding with the lower bound in the Hashin-Shtrikman theory, when the inhomogeneities are elastically harder than the matrix. When the inhomogeneities are softer, the average field theory gives the value, equal to the upper bound in the Hashin-Shtrikman theory. Since Al₂O₃ is elastically harder than Pd, Model A gives a result, corresponding to the lower bound. Model B corresponds to the upper bound. The examination of an extreme case makes this reasoning clearer. Suppose that a ceramic phase is extremely harder than a metal phase. In Model B, then, the overall CTE strain is almost the same as that of the substrate unless $f=0$. The stress in the spherical metal particles is hydrostatic. Then, a large α^* in magnitude is needed to induce the plastic deformation. On the other hand, in Model A, the overall CTE strain differs from that of the substrate. Because of this, the stress to induce the plastic deformation can exist when α^* is relatively small in magnitude.

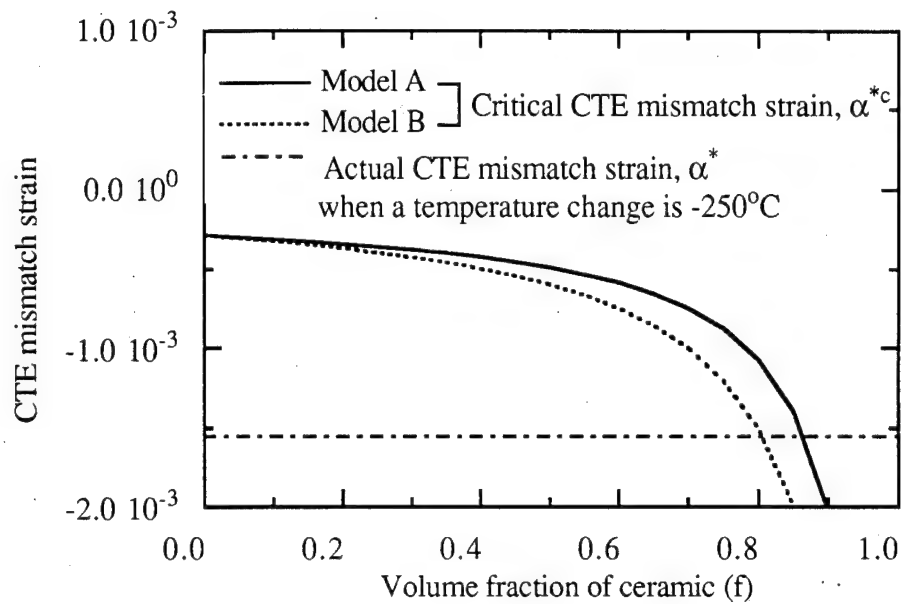


Figure 6.3. The prediction of the critical CTE mismatch strain in the Pd-Al₂O₃ FGM by Models A and B as a function of the volume fraction of Al₂O₃. The actual CTE mismatch strain is -1.55×10^{-3} .

6.3.2 Plastic strain in the metal

The plastic strain in the metal phase after the relaxation is also computed from Eq. (6.25) and the results are shown as a function of the volume fraction of the ceramic phase in Fig. 6.4. The smaller the volume fraction of the ceramic phase, the larger plastic deformation the metal phase undergoes. This is because a larger thermal stress is induced in the metal phase as the amount of the ceramic phase decreases. This explanation also holds for the calculated difference in the plastic strains in Models A and B.

6.3.3 Stress state in metal

The present analysis employs the energy approach, in which the expressions such as Eq. (6.19) contain no terms explicitly expressed by the stresses in the metal phase. This is advantageous because an energy is a scalar quantity and the parameters to determine are also scalars such as α^* and ε_p , owing to a certain symmetry requirement. However, we can conduct a similar analysis, using a stress approach by examining the magnitude of Von-Mises stress, $|\sigma_{11}^m - \sigma_{33}^m| = |\sigma_{22}^m - \sigma_{33}^m|$. If this is larger than 2k, the plastic deformation occurs until it becomes

equal to $2k$, as ε_p increases. To demonstrate this point, we have drawn Fig. 6.5, indicating that when f is smaller than f^* , $|\sigma_{11}^m - \sigma_{33}^m|$ before the relaxation is large than $2k$. After the relaxation, $|\sigma_{11}^m - \sigma_{33}^m|$ becomes $2k$. It is noted in Fig. 5 that the intersecting points with lines are the same as those in Fig. 3, indicating that the model based on the stress criterion gives rise to the same results by the energy approach.

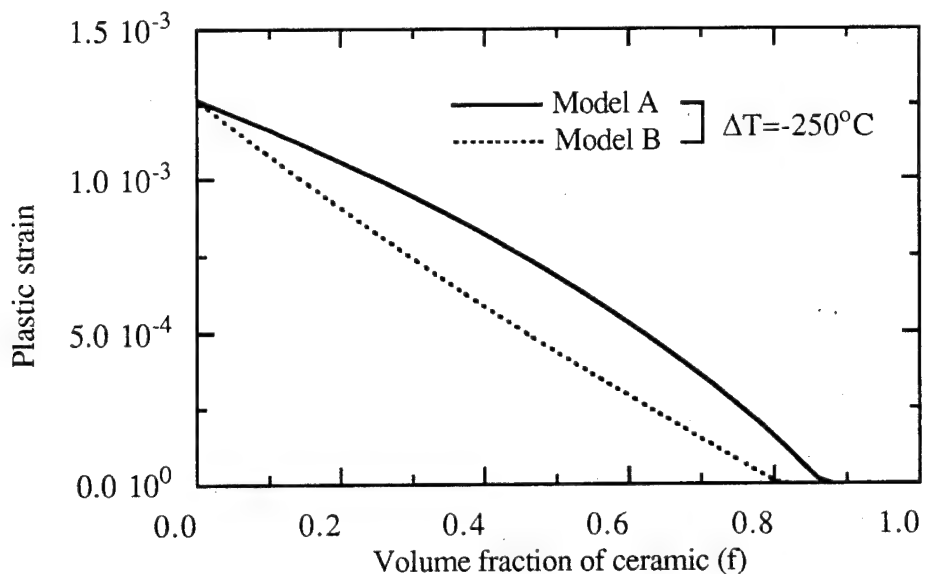


Figure 6.4. Plastic strain in Pd in Pd-Al₂O₃ FGM calculated by Models A and B as a function of volume fraction of Al₂O₃.

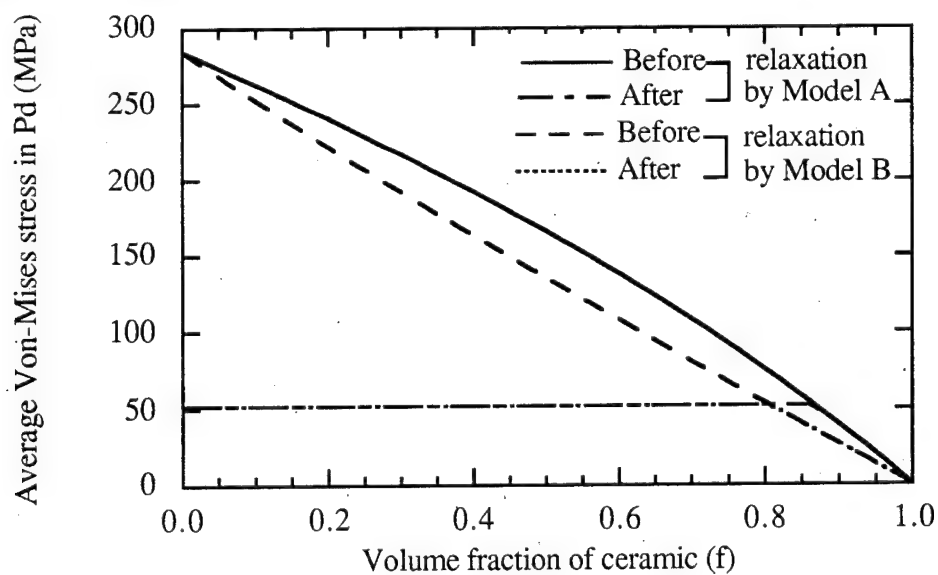


Figure 6.5 Average of Von-Mises stress, $|\sigma_{11}^m - \sigma_{33}^m|$ in Pd before and after the relaxation as a function of volume fraction of Al₂O₃.

6.3.4 Effect of the heterogeneous structure of a layer

To calculate the elastic state, the i -th layer is hypothetically removed from FGM. After this stage and before the reattachment process, the traction on its surfaces is zero, regardless of the presence of ε_{ij}^T and ε_{ij}^P . When these are introduced, the originally planar surfaces become slightly roughened, because of the traction free condition. The wavelength of the roughness is in the order of the particle spacing. Thus, when the layer is reattached, stress due to the surface roughness is induced, in addition to Eq. (6.17). However, the additional stress diminishes to a negligible degree at a few wavelengths below the surfaces, the Saint Venant principle. If the thickness of the layer is sufficiently larger than the particle spacing, the effect of the surface roughness on the energy evaluation can be ignored.

6.3.5 General

Recently, extensive studies were reported for the nucleation, arrangement and motion of crystal dislocations in multi-layered structures [19-24]. In these studies, the structures consist of single crystal layers, which are coherently connected to each other. On the contrary, in the present study a layer is polycrystalline, containing embedded particles. Thus, a continuum approach as adopted here is adequate. In this case, the process of dislocation generation is not involved, because the composition and structure do not change significantly across the interface of two neighboring layers. In particular, most of a metal phase is connected at the interface with neighboring layers in Model A. In Model B, the relaxation occurs inside isolated metal particles, whose interface with a ceramic matrix cannot be coherent everywhere. Thus, the ceramic/metal interface can be assumed to be dislocated before the relaxation. Similarly, no change in interfacial energies, to be calculated essentially by the discrete dislocation core energies, is involved.

Finally, we would like to mention that if diffusion and sliding on the metal/ceramic interfaces can occur, a more relaxed state is achieved [25]. Roughly speaking, this is because the combined process of sliding and diffusion on a ceramic/metal interface is equivalent to or more effective than the plastic deformation occurring inside the metal. It is noted that sliding occurs as long as a tangential traction does not vanish, while usual plastic deformation encounters a certain resistance, yield strength. Similarly, interfacial diffusion occurs whenever the gradient of a normal traction along the interface is not zero. However, these sliding and diffusional relaxation processes occur with a significant rate only at high temperatures.

6.4 Summary

The criterion to initiate dislocation punching in the metal of FGM consisting of metal and ceramic phases was examined. Two models were employed: ceramic particles embedded in metal matrix (Model A) and metal particles embedded in ceramic matrix (Model B). The theory was applied to a model Pd-Al₂O₃ FGM system, where 100% Pd is located atop and graded smoothly toward 100% Al₂O₃ ceramic substrate. When the volume fraction of the ceramic is larger than 0.87 and 0.81 for Models A and B, respectively, the dislocation punching does not take place. For the lower volume fraction of Al₂O₃, the plastic strains by Models A and B were also computed, which increase as the volume fraction of the ceramic decreases. The Von-Mises stresses in the metal, $|\sigma_{11}^m - \sigma_{33}^m|$, before and after the relaxation were calculated, showing that it is relaxed to the yield stress of the metal when the punching criterion is met. The critical CTE mismatch strains, plastic strains and stresses before and after the relaxation by both Models A and B coincide each other relatively well. Thus, the present model can predict the whole range of the volume fraction of ceramic phase.

6.5 Reference

1. Hedes, S. M. and Mitchell, J. W., 1953, "Observation of polyhedral substructure in crystals of silver bromide," *Phil. Mag.*, 44, 223-224.
2. Ashby, M. F. and Johnson, L., 1969, "On the generation of dislocations at misfitting particles in a ductile matrix," *Phil. Mag.*, 20, 1009-1022.
3. Tanaka, K., Narita, K. and Mori, T., 1972, "Work hardening of materials with strong inclusions after prismatic punching," *Acta Metall.*, 20, 297-304.
4. Arsenault, R. J. and Shi, N., 1986, "Dislocation generation due to differences between the coefficients of thermal expansion," *Mater. Sci. Eng.*, 81, 175-187.
5. Taya, M. and Mori, T., 1987, "Dislocations punched-out around a short fiber in a short fiber metal matrix composite subjected to uniform temperature change," *Acta Metall. Mater.*, 35, 155-162.
6. Taya, M., Lulay, K. E. and Lloyd, D. J., 1991, "Strengthening of a particulate metal matrix composite by quenching," *Acta Metall. Mater.*, 39, 73-87.
7. Dunand, D. C. and Mortensen, A., 1991, "On the relaxation of a mismatching spheroid by prismatic loop punching," *Scripta Metal. Mater.*, 25, 761-766.
8. Shibata, S., Mori, T. and Taya, M., 1992, "Stress relaxation by dislocation punching to radial direction from a long fiber in a composite," *Scripta Metal. Mater.*, 26, 363-368.

9. Shibata, S., Taya, M., Mori, T. and Mura, T., 1992, "Dislocation punching from spherical inclusions in a metal matrix composite," *Acta Metall. Mater.*, 40, 3141-3148.
10. Shieu, F. S. and Saas, S. L., 1991, "Dislocation mechanisms for the relaxation of thermal stress at metal-ceramic interfaces," *Acta Metall. Mater.*, 39, 539-547.
11. Matthews, J. W. and Blakeslee, A. E., 1974, "Defects in epitaxial multilayers," *J. Crystal Growth*, 27, 118-125.
12. Freund, L. B., 1987, "The stability of a dislocation threading a strained layer on a substrate,"
13. Taya, M. and Mori, T., 1994, "Dislocation punching from ceramic/metal interfaces," *J. Eng. Mater. Tech.*, 116, 408-413.
14. Eshelby, J. D., 1957, "The determination of the elastic field of an ellipsoidal inclusion and related problems," *Proc. R. Soc. London A*, 241, 376-396.
- J. Appl. Mech., 54, 553-557.
15. Mori, T. and Tanaka, K., 1973, "Average stress in matrix and average energy of materials with misfitting inclusions," *Acta Metall.*, 21, 571-574.
16. Mura, T., 1987, *Micromechanics of defects in solids*, 2nd ed., Martinus Nijhoff Publisher.
17. Hashin, Z. and Shtrikman, S., 1962, "A variational approach to the theory of the elastic behavior of polycrystals," *J. Mech. Phys. Solids*, 21, 711-720.
18. Wakashima, K. and Tsukamoto, H., 1991, "Mean field micromechanics model and its application to the analysis of thermomechanical behavior of composite materials," *Mater. Sci. Eng. A*, 146, 291-316.
19. Hirth, J. P. and Feng, X., 1990, "Critical layer thickness for misfit dislocation stability in multilayer structures," *J. Appl. Phys.*, 67, 3343-3349.
20. Kamat, S. V. and Hirth, J. P., 1990, "Dislocation injection in strained multilayer structures," *J. Appl. Phys.*, 67, 6844-6850.
21. Dregia, S. A. and Hirth, J. P., 1991, "A rebound mechanism for Lomer dislocation formation in strained layer structures," *J. Appl. Phys.*, 69, 2169-2175.
22. Feng, X. and Hirth, J. P., 1992, "Critical layer thicknesses for inclined dislocation stability in multilayer structures," *J. Appl. Phys.*, 72, 1386-1394.
23. Gosling, T. J., Willis, J. R., Bullough, R. and Jain, S. C., 1993, "The energetics of dislocation array stability in strained epitaxial layers," *J. Appl. Phys.*, 73, 8297-8303.
24. Gosling, Bullough, R., T. J., Jain, S. C. and Willis, J. R., 1993, "Misfit dislocation distributions in capped (buried) strained semiconductor," *J. Appl. Phys.*, 73, 8267-8278.
25. Mori, T., Huang, J. H. and Taya, M., 1996, "Stress relaxation by plastic flow, interfacial sliding and diffusion in an inclusion bearing materials," submitted to *Acta Metall.*.

Appendix

Since the calculation for C_{ij} and D_i is rather involved, only its results are given below.

$$C_{11} = (1-f) \left[\frac{-20(1-2v_m)}{15(1-v_m)} \frac{\bar{\lambda}}{\mu_m} + \frac{2(15v_m - 9)}{15(1-v_m)} \frac{\bar{\mu}}{\mu_m} \right] + \frac{2(\lambda_c + \mu_c)}{\mu_m} \quad (A-1)$$

$$C_{12} = (1-f) \left[\frac{-10(1-2v_m)}{15(1-v_m)} \frac{\bar{\lambda}}{\mu_m} + \frac{2(5v_m - 1)}{15(1-v_m)} \frac{\bar{\mu}}{\mu_m} \right] + \frac{\lambda_c}{\mu_m} \quad (A-2)$$

$$C_{21} = (1-f) \left[\frac{-20(1-2v_m)}{15(1-v_m)} \frac{\bar{\lambda}}{\mu_m} + \frac{4(5v_m - 1)}{15(1-v_m)} \frac{\bar{\mu}}{\mu_m} \right] + \frac{2\lambda_c}{\mu_m} \quad (A-3)$$

$$C_{22} = (1-f) \left[\frac{-10(1-2v_m)}{15(1-v_m)} \frac{\bar{\lambda}}{\mu_m} + \frac{4(5v_m - 4)}{15(1-v_m)} \frac{\bar{\mu}}{\mu_m} \right] + \frac{(\lambda_c + 2\mu_c)}{\mu_m} \quad (A-4)$$

$$D_1 = -2 \left[(1-2v_m) \frac{\bar{\lambda}}{\mu_m} + (1-v_m) \frac{\bar{\mu}}{\mu_m} \right] \quad (A-5)$$

$$D_2 = 2 \left[-(1-2v_m) \frac{\bar{\lambda}}{\mu_m} + 2v_m \frac{\bar{\mu}}{\mu_m} \right] \quad (A-6)$$

7. Conclusion

The major results of this project are summarized as

- (1) The dimensional change (ϵ) of a metal matrix composite subjected to creep/thermal cycling increases with maximum temperature (T_{max}), applied stress (σ) while the volume fraction of filler (f) dependence of ϵ is that ϵ increases with f and peaked at a certain value (f^*), then ϵ decreases with f beyond f^* . The shape of thermal cycling, particularly duration of heating has a strong effect on the dimensional change of a metal matrix composite. For example, if the duration is short even for higher maximum temperature, its effect on the composite dimensional change is much less than for the case of longer duration of high temperature (T_{max}) exposure and lower T_{max} . The case of short duration of heating with relatively high T_{max} can be encountered in the application of a MMC to brake disc, to which the present model is applicable.
- (2) The main driving force for the degradation of metal matrix composites after subjected to creep/thermal cycling is the CTE misfit strain $\epsilon^* = \Delta\alpha\Delta T$ where α , T are the CTE and temperature and Δ is change. When ϵ^* is not large so that the local yielding around ceramic particulates takes place, the model of dislocation punching is needed to simulate the relaxation precisely while ϵ^* is large, the assumption of general yielding in the matrix phase is valid.
- (3) Relaxation phenomena in a metal matrix composite can take many forms: interfacial sliding, interfacial diffusion, and bulk diffusion. Complete relaxation can be found by minimizing the total potential energy by using the variational principle developed in this project. For example, the complete relaxation of a creeping composite is that the Von-Mises stress in the metal matrix becomes zero, i.e. hydrostatic state of stress which can be obtained as a part of the present analysis.
- (4) In a functionally graded material (FGM) metal phase is smoothly changed from metal phase to ceramic phase through a number of layers consisting of metal-ceramic composite. The relation of CTE misfit strain in a FGM by dislocation punching is studied with findings: there exists a threshold FGM layer, beyond which toward ceramic phase, no dislocation punching takes place, and below which toward metal phase, dislocation punching takes place, resulting in the plastic strains (ϵ_p) in the metal phase. The magnitude of ϵ_p is obtained by the present model.

8. List of Publication under This Grant

1. Taya, M., Armstrong, W. D. and Dunn, M. L., 1993, "Thermal Cycling Damage of Metal Matrix Composites: Analytical Study on Dimensional Change," Aging of Energy Production and Distribution Systems, eds by M. M. Carroll and P. D. Spaos, ASME Book No. AMR 128, pp. 201-210.
2. Dunn, M. L. and Taya, M., 1994, "Modeling of Thermal Cycling Creep Damage of Short Fiber Metal Matrix Composites," Mater. Sci. Eng., A176, pp 349-355.
3. Arsenault, R. J., Fishman, S. G. and Taya, M., 1994, "Deformation and Fracture Behavior of Metal-Ceramic Matrix Composite Materials," Progress in Mater. Sci., Vol. 38, in memory of Prof. Peter Haasen, pp. 1-157.
4. Lee, J. K., Taya, M. and Lloyd, D. J., 1995, "Dimensional Change of Metal Matrix Composites Subjected to Thermal Cycling/Creep," Proc. of 5th Intl. Conf. Plasticity & its Current Applications, eds S. Tanimura and A. S. Khan, Gordon and Breach Pub., pp. 701-704.
5. Taya, M. and Mori, T., 1994, "Dislocation Punching from Metal/Ceramic Interfaces," J. Eng. Mater. Tech., Vol. 116, pp. 408-413.
6. Li, Z., Taya, M., Dunn, M. L., and Watanabe, R., 1995, "Experimental Study of the Fracture Toughness of a Ceramic/Ceramic-Matrix Composite Sandwich Structure," J. Amer. Ceram. Soc., 78(6), pp 1633-1639.
7. Lee, J. K., Taya, M. and Lloyd, D. J., 1995, "Dimensional Change of Metal Matrix Composites Subjected to Creep/Thermal Cycling Loading," ibid, pp. II-613-620.
8. Walker, G., Crow, W. and Taya, M., 1995, "Long Term Thermal Cycling of SCS-6/Ti-15-3 Metal Matrix Composite," Proceedings of ICCM-10, Whistler, B. C., Canada, eds A. Poursartip and K. Street, Woodhead Pub. Ltd., pp. II-711-718.
9. Taya, M., Lee, J. K., Lui, M. and Armstrong, W. D., 1995, "Creep and Thermal Cycling Fixture Design for Metal Matrix Composites," Experimental Mechanics, pp. 66-70.
10. Lee, J. K., Taya, M. and Lloyd, D. J., 1996, "Dimensional Change of Metal Matrix Composites Subjected to Thermal Cycling Creep Loading," Proceedings of Prof. J. Weertman's Symp., TMS-AIME, eds R. J. Arsenault et al., in press.
11. Taya, M., Lee, J. K. and Lloyd, D. J., 1996, "Strengthening by Dislocation Punching in Metal-Ceramic Composites," Proceedings of Intl. Symp. Mater. Chem. in Nuclear Environment, eds M. Kitajima et al., pp. 277-288.